

# Orbit Design Around Asteroids

Literature Study

Abhishek Agrawal



Cover image credit: Adopted from European Southern Observatory. Artist's Impression of the binary asteroid Antiope.

*"If you wish to make an apple pie from scratch, you must first invent the universe."*

Carl Sagan



# PREFACE

After 45 years since the day man landed on the Moon, mankind created history, yet again. For the first time ever, a spacecraft was put into an orbit around a comet and a lander was deployed to its surface. This was the Rosetta mission; launched in March 2004, the spacecraft took an astonishing 10 years to travel to the comet 67P/Churyumov-Gerasimenko, finally arriving at the comet in August 2014. This is an immense achievement for the scientists and engineers involved in the Rosetta mission because space missions to small irregular bodies in our solar system, both comets and asteroids, pose significant dynamical challenges. For scientists, missions to comets and asteroids are of great interest since in-situ exploration of these small bodies can provide insight into the birth of our Solar System and answer some very important and fundamental questions such as those about the origins of life on Earth. Now even the private space industry is interested in these small bodies, such as in mining the vast reserves of untapped natural resources within the small bodies. For a student, designing and assessing orbits around a small irregular body, and in our case an asteroid, turns out to be one of the toughest problems in astrodynamics, making it a perfect research topic for an MSc Thesis.

This report serves to be a *Literature Study* in the framework of the Master's program at the Faculty of Aerospace Engineering, Delft University of Technology. It paves way for the upcoming thesis project, where the actual research work shall be carried out. I am grateful I could do this literature study under the supervision of my supervisor Ir. Ron Noomen and with support from Dr. Jinglang Feng. Their experience in the subject matter has been of tremendous help to me. In writing this report, I have tried my very best to ensure that the material in the report is presented in a manner which is pleasant to read and understand. I hope you can gain some valuable knowledge from reading this report.

*Abhishek Agrawal  
Delft, August 2016*



# CONTENTS

Preface . . . . .	v
<b>List of Symbols</b>	<b>ix</b>
<b>List of Acronyms</b>	<b>xiii</b>
<b>1 Introduction</b>	<b>1</b>
1.1 Research problem . . . . .	3
1.2 Outline of the report . . . . .	4
<b>2 Mission Heritage</b>	<b>5</b>
2.1 Past and Current Missions . . . . .	5
2.1.1 Hayabusa 2 . . . . .	5
2.1.2 Dawn . . . . .	6
2.1.3 Rosetta . . . . .	9
2.1.4 NEAR . . . . .	13
2.2 Future Missions . . . . .	14
2.2.1 OSIRIS-REx . . . . .	14
2.2.2 AIDA . . . . .	16
2.3 Conclusion . . . . .	17
<b>3 Modeling The Gravitational Potential Of A Small Irregular Body</b>	<b>19</b>
3.1 Introduction . . . . .	19
3.2 Spherical Harmonics Model . . . . .	19
3.3 Ellipsoid Harmonics Model . . . . .	22
3.4 Elliptic Integral Model . . . . .	24
3.5 Mass Concentration Model . . . . .	27
3.6 Polyhedron Model . . . . .	28
3.7 Conclusion . . . . .	30
<b>4 Orbital Perturbations</b>	<b>35</b>
4.1 Introduction . . . . .	35
4.2 Solar Radiation Pressure . . . . .	35
4.3 Third Body Perturbation . . . . .	37
4.4 Lagrange Planetary Equations . . . . .	38
4.5 Conclusion . . . . .	38
<b>5 The Full 2-Body Problem</b>	<b>41</b>
5.1 Introduction . . . . .	41
5.1.1 Sphere-Ellipsoid Binary System . . . . .	41
5.1.2 Ellipsoid-Ellipsoid Binary System . . . . .	42
5.2 Mutual Potential Formulation for Two Polyhedrons . . . . .	43
5.3 Force terms for equations of motion from mutual potential derivatives . . . . .	46
5.4 Torque terms for equations of motion from mutual potential derivatives . . . . .	48
5.5 Equations of motion for the full 2-body problem . . . . .	49
5.6 Conclusion . . . . .	50

<b>6 The Restricted Full 3 Body Problem</b>	<b>51</b>
6.1 Introduction . . . . .	51
6.1.1 Circular Restricted Three-Body Problem . . . . .	51
6.1.2 Sphere-Ellipsoid Restricted Three-Body Problem . . . . .	51
6.1.3 Ellipsoid-Ellipsoid Restricted Three-Body Problem . . . . .	52
6.2 Polyhedron-Polyhedron Restricted Full Three-Body Problem . . . . .	53
6.2.1 Linearization . . . . .	54
6.3 Conclusion . . . . .	55
<b>7 Numerical Integration Methods</b>	<b>57</b>
7.1 Introduction . . . . .	57
7.2 Runge-Kutta Methods . . . . .	58
7.2.1 General Runge-Kutta Methods . . . . .	58
7.2.2 Embedded Runge-Kutta Methods . . . . .	59
7.2.3 Step Size Control . . . . .	60
7.2.4 Runge-Kutta-Nyström Methods . . . . .	61
7.3 Multistep Methods . . . . .	61
7.3.1 Adams-Basforth Methods . . . . .	62
7.3.2 Adams-Moulton and Predictor-Corrector Methods . . . . .	63
7.3.3 Variable-Order and Variable Step Size Methods . . . . .	65
7.4 Extrapolation Methods. . . . .	66
7.4.1 Mid-Point Rule . . . . .	66
7.4.2 Extrapolation . . . . .	66
7.5 Lie Group Variational Integrator . . . . .	67
7.6 Taylor Series Method. . . . .	68
7.7 Performance Verification Of A Numerical Integrator . . . . .	70
7.8 Conclusion . . . . .	71
<b>8 Monte Carlo Simulation</b>	<b>75</b>
8.1 Introduction . . . . .	75
8.2 Random Value Generating Function . . . . .	76
8.3 Random Value Sampling. . . . .	76
8.4 Conclusion . . . . .	77
<b>9 Dynamical Systems Theory</b>	<b>79</b>
9.1 Introduction . . . . .	79
9.2 (Planar) Circular Restricted Three-Body Problem . . . . .	79
9.3 Energy Manifold, Hill's Region, and Zero Velocity Curves . . . . .	80
9.4 Libration Points . . . . .	82
9.5 Invariant Manifolds of a Periodic Orbit . . . . .	84
9.5.1 Monodromy Matrix. . . . .	84
9.5.2 Poincaré Maps . . . . .	84
9.5.3 Computation of Invariant Manifolds . . . . .	85
9.6 Conclusion . . . . .	85
<b>10 Conclusions</b>	<b>87</b>
<b>Bibliography</b>	<b>89</b>

# LIST OF SYMBOLS

## LATIN LETTERS

<b>Symbol</b>	<b>Units</b>	<b>Description</b>
$a$	m	Semi-major axis of $\varepsilon_0$
$a_{ip}, b_{ip}, c_{ip}, d_{ip}$	–	Polynomial coefficients in the Ellipsoidal harmonic expansion, where $i = 1, 2, \dots$
$b$	m	Semi-major axis of $\varepsilon_0$
$B$	$\text{kg}/\text{m}^2$	Mass-to-area ratio of the particle orbiting the binary asteroid system
$c$	m	Semi-major axis of $\varepsilon_0$
$C_{lm}$	–	Gravitational field harmonic coefficient (also called Stokes Coefficient)
$\hat{d}$	–	Unit vector joining the centre of Sun to binary asteroid barycentre and pointing away from the sun
$E_n^p$	–	Lamé's Function of the first kind
$E_e$	–	Edge dyad computed as the summation of two outer products where each outer product involves the face normal vector and the edge normal vector
$E_x, E_y, E_e$	m	Focal lengths of the triaxial ellipsoid as used in elliptic integral model for gravitational potential
$F_f$	–	Face dyad computed as the outer product of the face normal vector with itself
$\mathbf{F}_\theta^A$	N	Force acting on body $A$ due to a second body $B$
$\mathbf{F}_\theta^B$	N	Force acting on body $B$ due to a second body $A$
$F_n^p$	–	Lamé's function of the second kind
$G$	$\text{m}^3 \text{ kg}^{-1} \text{ s}^{-2}$	Universal gravitational constant
$g_{SRP}$	$\text{m/s}^2$	Magnitude of the solar radiation pressure perturbing acceleration
$h$	m	The focal length of $\varepsilon_0$
$I_0, I_1, I_2, I_3$	–	Basic integrals used in the evaluation of the constant density ellipsoid potential
$k$	m	The focal length of $\varepsilon_0$
$K_n^p$	–	The Lamé's function of the first kind
$L_n^p$	–	The Lamé's function of the first kind
$l$	–	Degree of spherical harmonics expansion
$L_e$	–	Dimensionless per-edge factor used in polyhedron modeling
$m$	–	Order of spherical harmonics expansion
$M$	kg	Mass of a body
$M_n^p$	–	The Lamé's function of the first kind
$n$	–	Degree in Ellipsoidal Harmonic expansion
$\hat{n}_f$	–	Normal vector to a face 'f' of the polyhedron
$\hat{n}_e^f$	–	Normal vector to the edge 'e' of a face 'f' of the polyhedron

---

$N_n^p$	—	The Lamé's function of the first kind
$p$	—	Order, respectively, in Ellipsoidal Harmonic expansion
$P$	—	Transformation matrix mapping from body-fixed frame of body A to inertial frame
$\mathbf{P}$	kg-m/s	Relative linear momentum in the full two-body problem
$P_{lm}$	—	Associated Legendre function of degree l and order m
$\mathbf{q}$	—	6-element vector containing barycentre coordinates of polyhedron facet vertices
$r$	m	position vector magnitude
$\mathbf{r}$	$m$	position vector
$\mathbf{R}$	m	Relative position vector between the binary asteroid centroids, defined in inertial frame
$\overrightarrow{\mathbf{r}}$	m	second representation for position vector
$R_{celt}$	$m^2/s^2$	Perturbing potential from other celestial bodies
$R_{SRP}$	$m^2/s^2$	Solar Radiation Pressure perturbing potential
$S$	—	Transformation matrix mapping from body-fixed frame of body B to inertial frame
$S_{lm}$	—	Gravitational field harmonic coefficient (also called Stokes Coefficient)
$s_1, s_2, s_3$	$m^2$	Ellipsoidal coordinates as used in elliptic integral model for gravitational potential
$T$	—	Transformation matrix mapping from body-fixed frame of body B to body-fixed frame of body A
$U$	$m^2/s^2$	Gravitational potential
$u$	—	Barycentre coordinate, used in mutual potential formulation for two polyhedrons
$u$	m	Alternate variant of ellipsoidal coordinates used in elliptic integral model for gravitational potential
$U_{SE}$	$m^2/s^2$	Gravitational potential for the sphere-ellipsoid binary asteroid model
$U_s$	$m^2/s^2$	Gravitational potential for the sphere in sphere-ellipsoid binary asteroid model
$U_{e(1,2)}$	$m^2/s^2$	Gravitational potential for the ellipsoids in both the sphere-ellipsoid and ellipsoid-ellipsoid binary asteroid model
$v$	—	Barycentre coordinate, used in mutual potential formulation for two polyhedrons
$w$	—	Barycentre coordinate, used in mutual potential formulation for two polyhedrons
$w_f$	—	Dimensionless per-face factor used in polyhedron modelling
$x$	m	position in X direction
$\hat{\mathbf{x}}$	—	unit vector along the X axes in the Cartesian coordinate system
$y$	m	position in Y direction
$\hat{\mathbf{y}}$	—	unit vector along the Y axes in the Cartesian coordinate system
$z$	m	position in Z direction

---

$\hat{\mathbf{z}}$	—	unit vector along the Z axes in the Cartesian coordinate system
--------------------	---	---

**GREEK**

Symbol	Units	Description
$\alpha$	rad	True anomaly of the Sun with respect to the binary asteroid system
$\alpha_{np}$	—	Ellipsoidal Harmonic Coefficient
$\beta$	rad	Alternate variant of ellipsoidal coordinates used in elliptic integral model for gravitational potential
$\delta$	rad	spherical coordinate called latitude
$\gamma_n^p$	—	Normalization constant for ellipsoidal harmonic expansion
$\Gamma_A$	$\text{kg}\cdot\text{m}^2/\text{s}$	Angular momentum of the primary asteroid expressed in its own body-fixed frame
$\Gamma_B$	$\text{kg}\cdot\text{m}^2/\text{s}$	Angular momentum of the secondary asteroid expressed in the primary asteroid's body-fixed frame
$\lambda$	rad	spherical coordinate called longitude
$\lambda_1, \lambda_2, \lambda_3$	m	Ellipsoidal Coordinates
$\lambda_1^{ref}$	m	Largest semi-major axis of $\varepsilon_0$
$\lambda$	rad	Alternate variant of ellipsoidal coordinates used in elliptic integral model for gravitational potential
$\mu_A$	Nm	Torque acting on body $A$ as expressed in the frame fixed to body $A$
$\mu_B$	Nm	Torque acting on body $B$ as expressed in the frame fixed to body $A$
$\Omega_A$	rad/s	Angular velocity of the primary asteroid expressed in its own body frame
$\Omega_B$	rad/s	Angular velocity of the secondary asteroid expressed in its own body frame
$\rho$	—	Reflectivity of a particle orbiting the binary asteroid system
$\varepsilon_0$	—	Reference ellipsoid used in the Ellipsoid Harmonics gravitational potential model



# LIST OF ACRONYMS

<b>AB</b>	Adams-Bashforth
<b>AD</b>	Automatic Differentiation
<b>AIDA</b>	Asteroid Impact and Deflection Assessment
<b>AIM</b>	Asteroid Impact Mission
<b>AM</b>	Adams-Moulton
<b>AU</b>	Astronomical Unit
<b>BASiX</b>	Binary Asteroid In-Situ Exploration
<b>CCAR</b>	Colorado Center For Astrodynamics Research
<b>DART</b>	Double Asteroid Redirection Test
<b>DSN</b>	Deep-Space Network
<b>EDVEGA</b>	Electric Delta-V Earth Gravity Assist
<b>ESA</b>	European Space Agency
<b>HAMO</b>	High Altitude Mapping Orbit
<b>JAXA</b>	Japan Aerospace Exploration Agency
<b>LAMO</b>	Low Altitude Mapping Orbit
<b>LGVI</b>	Lie Group Variational Integrator
<b>LPE</b>	Lagrange Planetary Equations
<b>MBO</b>	Main-Belt Objects
<b>NASA</b>	National Aeronautics and Space Administration
<b>NEA</b>	Near-Earth Asteroids
<b>NEAR</b>	Near Earth Asteroid Rendezvous
<b>ODE</b>	Ordinary Differential Equation
<b>OSIRIS-REx</b>	Origins, Spectral Interpretation, Resource Identification, Security, Regolith EXplorer
<b>PCRTBP</b>	Planar Circular Restricted Three Body Problem
<b>PECE</b>	Predictor-Corrector
<b>R3BP</b>	Restricted Three-Body Problem

<b>RC3</b>	Rotation Characterization 3
<b>RCS</b>	Reaction Control System
<b>RK</b>	Runge-Kutta
<b>RK4</b>	Runge-Kutta 4
<b>RKN</b>	Runge-Kutta-Nyström
<b>SMASS</b>	Small Main-Belt Asteroid Spectroscopic Survey
<b>SRP</b>	Solar Radiation Pressure
<b>TNO</b>	Trans-Neptunian Objects
<b>TSM</b>	Taylor Series Method
<b>UST</b>	Unified State Theory



# 1

## INTRODUCTION

Asteroids are small rocky bodies in our solar system that are orbiting the Sun. These small bodies are basically the remnants from the process that formed the inner planets in our Solar System [29]. Asteroids are mainly found in an orbit between Jupiter and Mars and as such are classified as MBO (Main-Belt Objects). These MBO range in size from a few meters to hundreds of kilometers, the largest one being 1 Ceres with a diameter of 948 km. A subset of the MBO, called the NEA (Near-Earth Asteroids), are asteroids whose orbits come extremely close to, and sometimes even cross, the orbit of the Earth [26]. Other small bodies in our small system, classified as asteroids when broadly speaking, are the Trojans (small bodies captured at Jupiter's Lagrange points 4 and 5), the TNO (Trans-Neptunian Objects) (small bodies whose orbits around the Sun go beyond Neptune), the Centaurs (small bodies whose orbits lie in between Jupiter and Neptune) [26]. The asteroids in the main-belt tend to be more rocky in nature, however the small bodies beyond Jupiter tend to have a more icy-composition due to their relatively larger distance from the Sun [26]. A histogram plot depicting the distribution of MBO is shown in Figure 1.1. The gaps in the plot depict resonance in mean-motion between Jupiter and an asteroid [26].

Asteroids don't only exist as single bodies in the Solar System, but they are also found in local multi-body systems consisting of two to even three asteroids. With advanced asteroid detection methods, astrophysicists have found over 190 multiple asteroid systems in the Solar System [34]. Contrary to intuition, these multiple asteroid systems exhibit a wide diversity in terms of the size ratios of the components, their mutual orbits and separation, implicating that the individual components evolved differently over time [34]. If a multi-asteroid system consists of two or three components, which are bound gravitationally, then it is termed as *binary asteroids* or *triple asteroids* respectively. Triple asteroids are also sometimes termed as *trinary* or *ternary* [35]. Asteroid components that are not gravitationally bound but are genetically related, are termed as *asteroid pairs*. Asteroid pairs where the larger asteroid is a binary or a triple asteroid, are termed as *paired binaries* or *paired triples*, respectively. The larger component in a binary or triple asteroid system or an asteroid pair, is referred to as the *primary* and similarly the smaller component is referred to as the *secondary* [35]. Asteroids are further classified based on their dimensions and thermal properties, for which the reader should read the publication in [34].

We now know what asteroids are and the different ways in which they are found in our Solar System, but is it important to study them? There are three major, and most commonly expressed, reasons to study asteroids in our solar system, and not just from a distance such as through radar telescopes placed on Earth, but also through in-situ exploration involving spacecrafts and surface probes. These reasons are mentioned as follows.

- Asteroids are basically the material left-over from formation of planets in our Solar System. Thus, they are the perfect source to study and understand the origins of the Solar System, as

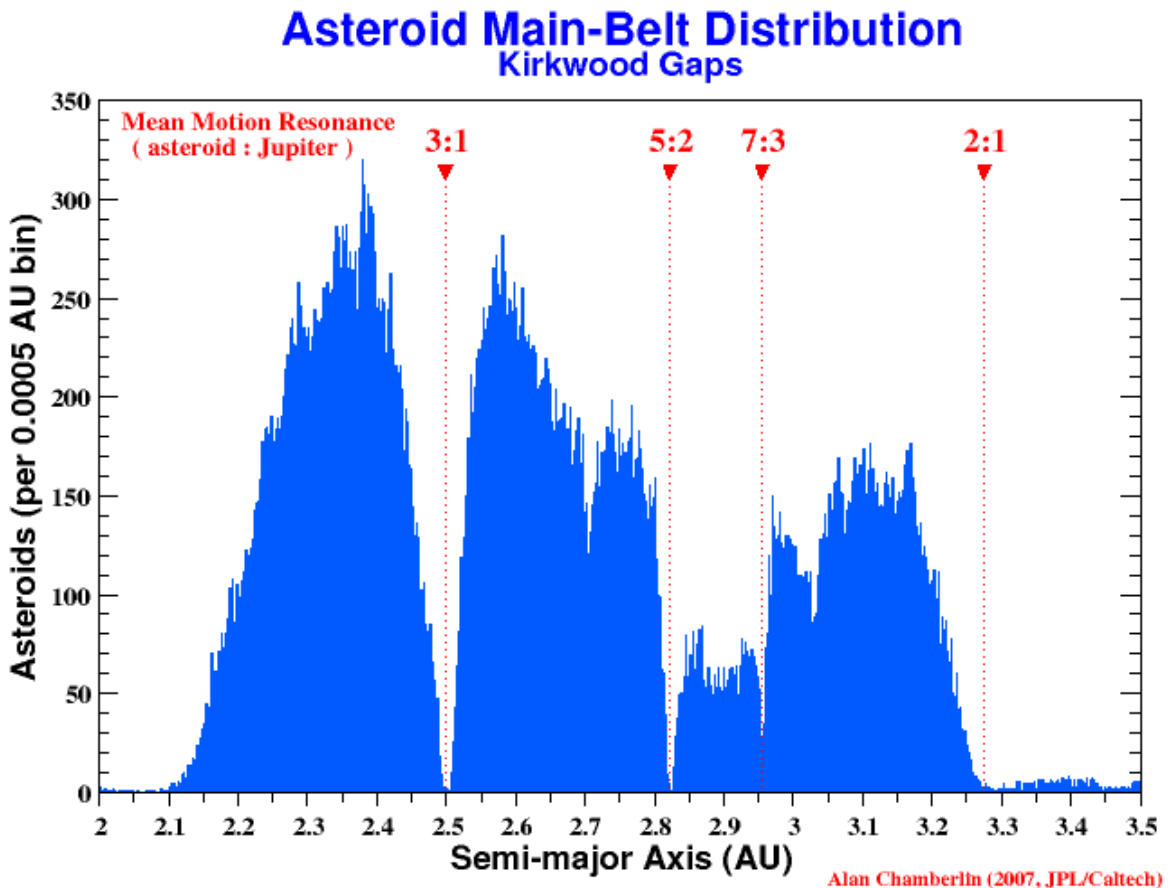


**Figure 1.1:** Histogram plot depicting distribution of semi-major axis of 156,929 main-belt asteroids, created in June 2007 [26].

they have remained in the same pristine form since the birth of the Solar System, unlike the planets which have undergone massive topographical and atmospheric changes after their formation. The asteroids can provide valuable information on the chemical composition and initial conditions which led to the formation of planets, including Earth some 4.6 billion years ago. Several scientists have also hypothesized that water and life could have been brought about on Earth through an asteroid or comet and hence exploration of these small bodies could provide a definite answer to an age old question of how life began on Earth [29].

- Asteroids have been hypothesized to have brought complex molecules to the surface of Earth that eventually resulted in life, but lately they have also been linked to the extinction of dinosaurs due to its impact with Earth. Earth is continuously bombarded with very small interplanetary material, most of which doesn't reach the surface of the Earth but gets evaporated in its atmosphere. However, every few 100 years, an asteroid spanning some tens of meter could impact Earth resulting in widespread damage, in the present case to life and property. But the impact from those will not cause the human race to extinct. But every 100,000 years or so, larger asteroids, spanning over tens of kilometer would impact the Earth, which will lead to extinction of life as we know it now. Although the probability of getting hit by an asteroid on such a large scale is low, it is still a statistical possibility and to be able to device strategies for active deflection of such asteroids, it is imperative that we understand more of the dynamics, properties and composition of the asteroids [29].

- The third most important reason for us to study asteroids, is the fact that these small bodies are rich in raw materials or minerals. NEA can be exploited for the resources that they possess and use it to build space structures or generate fuel for spacecrafts to enable human space exploration in farther reaches of the Solar System. By studying the asteroids, we can develop methods to tap the vast reservoirs of raw materials residing in them [29].

## 1.1 RESEARCH PROBLEM

In the previous section, we discussed what asteroids are and why its important to study them. In this section, we shall discuss, albeit broadly, the areas of research for the upcoming thesis work. The motivation for this literature study and the future thesis work arises from the fact that past in-situ space exploration activities have made use of explosive capsules to extract subsurface samples for analysis [42]. For asteroids with surface made of unconsolidated rock material or dust, use of explosive payloads to expose subsurface material could potentially result in the regolith being lofted from the surface of the asteroid. The lofted material could enter into a long term orbit, or a short term orbit concluding in re-impact of the lofted regolith back on the surface of the asteroid, or even escape the gravitational influence of the asteroid. This idea is fueled by a research paper [16] which discusses the re-accretion and escape of ejecta due to impact from impacts in the Ida system in the main-belt. The lofted regolith poses a serious threat to the safety of the spacecraft in orbit around the asteroid. To avoid any damage to it, it is necessary to develop models that can simulate the motion of the lofted regolith for a given asteroid, to as high an accuracy as possible, so that the mission design for asteroid exploration can account for it and ensure safety of the spacecraft. To do so we need to model the dynamics of the asteroid around the Sun, model the dynamical environment around the asteroid itself, and, although not limited to but also model the dynamics for multiple debris particles lofted from the asteroids surface and account for different perturbing forces that could affect the orbital motion of these particles. By running these simulation models we can compute trajectories for multiple particles at the same time and observe their long or short term behavior.

The tentative research questions shall be presented shortly. We say tentative because in the beginning, the report was aimed to focus on *orbital motion of spacecraft around a binary asteroid system*. However, towards the period around which the report was being concluded, a thesis opportunity was offered from the CCAR (Colorado Center For Astrodynamics Research) because of which the thesis topic was changed to *orbital motion of regolith lofted from the surface of an asteroid*. The content of the report is nevertheless useful since it still discusses the dynamics around an asteroid with the difference that instead of a spacecraft, now it will be applied to lofted regolith material. Due to the sudden shift in the focus of the thesis at the time of writing this report, the research questions presented below should be considered as only tentative. The final research questions or problem statements will be mentioned in the final thesis report. The core questions are listed as follows:

- Simulate, observe and characterize the motion of regolith lofted from the surface of an asteroid for extended periods of time.
- Does the lofted regolith enter a stable or unstable orbit? What are the corresponding initial conditions and can they be generalized for different asteroids?
- What is the correlation, if any, between the size of the lofted material against stable or unstable orbital motion? Can a critical size for the lofted material be determined, for the asteroid under study, which would differentiate between stable and unstable orbital motion for the lofted material?
- In case of stable orbits, are the orbits planar or spatial periodic?

- In case of an unstable orbit, does the lofted regolith fall back to the surface of the asteroid or does it escape the gravitational influence of the asteroid? Can this behavior be also generalized for a different asteroid?
- What is the subsequent motion of the regolith that re-impacts on the surface of the asteroid?
- For a regolith sample return mission based on a touch-and-go technique (such as the OSIRIS-REx (Origins, Spectral Interpretation, Resource Identification, Security, Regolith EXplorer) mission), is it possible to retrieve a sample without causing adjacent surface material to be lofted in to an orbit around the asteroid?
- For a subsurface sample return mission involving surface detonation (such as the Hayabusa-2 mission), how can the dangers of spacecraft damage from lofted regolith be averted or avoided?

## 1.2 OUTLINE OF THE REPORT

This literature study report tackles the problem of modeling particle dynamics and solving it in a systematic way. We begin by first describing the various missions that have been to asteroids in the past or are being operated currently along with missions planned for the future in Chapter 2. Chapter 3 discusses the various gravitational potential models that exist and have been applied in past for theoretical studies on orbital mechanics of or around asteroids along with the advantages and disadvantages of each model. Chapter 4 presents the relevant orbit perturbation models for working with particle dynamics around asteroids. Chapter 5 begins with a brief introduction to relatively low-fidelity full two-body problem models that have been extensively applied in the past following which an extensive discussion on mutual potential and coupled equations of motion for binary polyhedron-based asteroids is presented. Chapter 6 begins by introducing the relatively low-fidelity restricted three-body problem but the chapter focuses more on the dynamics of a particle around binary asteroid modeled as two polyhedrons. A linearization technique to reduce simulation loads has also been introduced in that chapter. Chapter 7 describes and compares the various numerical integration methods; an integrator is needed to propagate the orbital motion of a particle around an asteroid. Chapter 8 briefly describes the Monte Carlo simulation technique which will be utilized in our simulation package to generate multiple debris particles at the surface of an asteroid. Chapter 9 presents some basic concepts on dynamical systems theory such as poincaré maps which are used when one wants to characterize the motion of an orbiting particle. And finally, Chapter 10 concludes the literature study report.

# 2

## MISSION HERITAGE

Asteroids and comets have been the target of many spacecraft missions in the past two decades, yielding unparalleled scientific returns relative to ground-based observations. Several space agencies, both private (such as Deep Space Industries and Planetary Resources) and governmental, are planning future missions to these small bodies to not only study them in more detail but also to manipulate, deflect and extract resources from them. The current chapter shall highlight past and current missions to small bodies in Section 2.1 and future missions in Section 2.2.

### 2.1 PAST AND CURRENT MISSIONS

A brief overview on missions to asteroids and comets that have flown in past or are still active at the time of writing this report will be presented in this section. The various missions will be presented in a reverse chronological order.

#### 2.1.1 HAYABUSA 2

Hayabusa 2 is a JAXA (Japan Aerospace Exploration Agency) mission, launched on 3 December 2014. It will rendezvous with asteroid 1999 JU3 in 2018 and will return back to Earth with a sample from the asteroid in 2020. Hayabusa 2 carries an impactor that shall be used to create a crater on the asteroid to expose fresh material that will be collected and returned to Earth for further analysis [42]. Hayabusa 2 is a sequel to a previous asteroid mission by JAXA, called Hayabusa which explored the asteroid Itokawa.

The asteroid 1999 JU3 (and henceforth JU3) has been classified as a potentially hazardous asteroid which also happens to be in the list of potential targets for another sample return mission: OSIRIS-REx of NASA (National Aeronautics and Space Administration) (briefed in Section 2.2.1). JU3 was also a potential target for the Marco Polo-R mission of ESA (European Space Agency) as part of their Cosmic Vision Program, however in February 2014 it was not selected for the M3 Launch opportunity in the Cosmic Vision Program [10]. JU3 has an orbit with semi-major axis of 1.19 AU (Astronomical Unit) and an eccentricity of 0.19 putting the orbit's perihelion close to Earth's orbit and the aphelion near Mars' orbit. The asteroid is roughly spherical with an effective diameter of 875 m [42]. JU3 has been classified as a Cg-type asteroid in the SMASS (Small Main-Belt Asteroid Spectroscopic Survey) classification system which in turn is within the C-class in the Tholen classification system. C-class objects are believed to be primitive, volatile-rich remnants from the early solar system [4].

The entire low-thrust transfer trajectory of Hayabusa 2 has been divided in several phases. First is the EDVEGA (Electric Delta-V Earth Gravity Assist) phase wherein the spacecraft connects to the transfer trajectory to the asteroid JU3 via an Earth swing-by (Earth gravity assist maneuver). After

spending three years in the transfer leg of the trajectory, the spacecraft arrives at the JU3 asteroid which marks the beginning of the mission phase and close-proximity operations at the asteroid. After ending the mission phase, the spacecraft enters into a one year long return trajectory back to Earth [57]. The geometry of the trajectory along with the dates of departure and arrival for each transfer leg are shown in Figure 2.1.

The spacecraft will fly near the asteroid on a virtual line connected between JU3 and the Sun. This is because Hayabusa 2 has stationary solar panels. This configuration is illustrated in Figure 2.2 along with a detailed timeline [8]. It represents how spacecraft operational constraints were accounted for in orbit design. The orbit design ensures that the spacecraft is always facing the sun, resulting in the global characterization of the asteroid to be completed in almost a year.

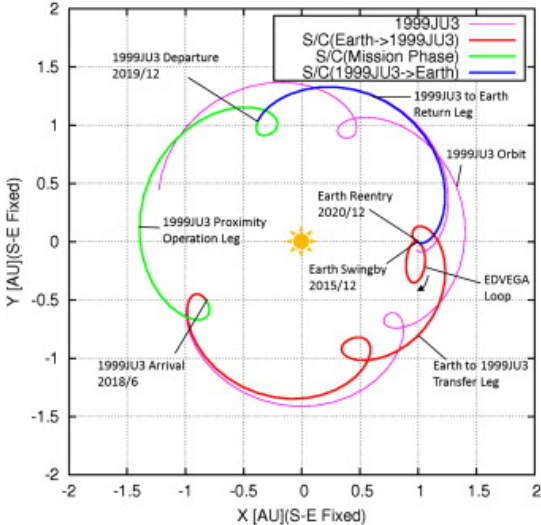


**Figure 2.1:** Trajectory geometry for Hayabusa-2, shown in an inertial reference frame centered at Sun and the line connecting the Sun and Earth is fixed i.e. the Sun-Earth line coincides with the X axis of the inertial frame [57].

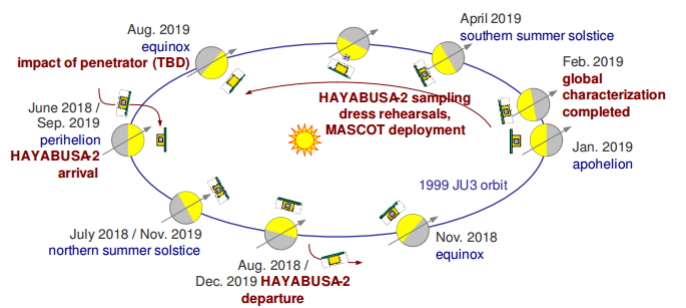


**Figure 2.2:** Hayabusa 2 mission phase [8].

### 2.1.2 DAWN

The Dawn mission of NASA was designed to rendezvous and orbit around the asteroids 4 Vesta and 1 Ceres. The objective of the mission was to characterize the asteroids' internal structure, shape, density, size, composition, mass and provide data on surface morphology, cratering, and magnetism [41].

Vesta and Ceres are two most massive asteroids that have survived largely intact through the collisional history of our solar system. Vesta appears to be a dry and differentiated body consisting of pyroxene-bearing lava flows. Telescopic observations have revealed mineralogical variations along the asteroid's surface. Certain meteorites have been linked to be fragments of Vesta. The latter has a dimension of 289 x 280 x 229 km. Ceres, the largest body in the asteroid belt with a dimension of 487 x 487 x 455 km, is very different from Vesta although its only slightly farther away from Sun than the latter. Microwave observations reveal that Ceres is covered in a clay like material, indicating the presence of water in its history. No meteorites have been linked to Ceres. Vesta, which is believed to be dry and differentiated, and Ceres, which consists of water ice that slowed its thermal evolution, form the bridge between the rocky bodies in the inner solar system and icy bodies in the outer solar system [48].

The dawn spacecraft was launched in September 2007 on-board a Delta-2 heavy rocket and after an initial checkout phase [44], it was put into its interplanetary orbit towards Vesta. The entire

interplanetary trajectory is depicted in Figure 2.3. The interplanetary cruise was performed using the on-board ion propulsion system. The cruise phase consisted of varying thrusting and strategically designed coasting periods. The latter was included for the ground control to perform orbit determination, downloading spacecraft engineering data and for uploading command sequences to the spacecraft using NASA's DSN (Deep-Space Network) [20]. After a gravity assist in February 2009, Dawn arrived at Vesta in July 2011 [20]. Four mapping orbits were planned around Vesta at three different mapping altitudes. All the orbits were close to polar inclination. Each orbit started as an instantaneous circular orbit but due to Vesta's gravity, these circular orbits grew into eccentric orbits. The different mapping orbits along with their altitudes are illustrated in Figure 2.4 [44].

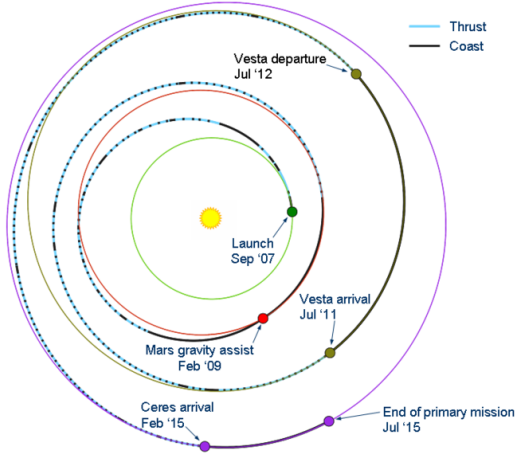


**Figure 2.3:** Dawn's Interplanetary Trajectory. The trajectory is depicted in blue when thrusting and in black when coasting. [20]

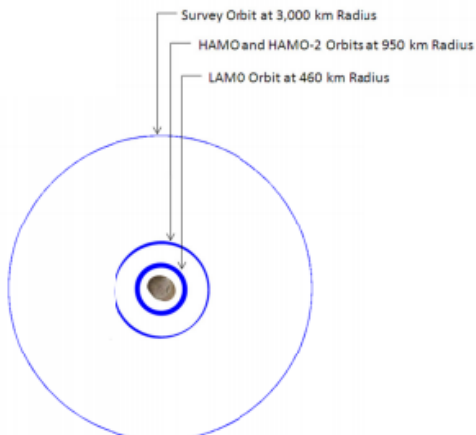


**Figure 2.4:** Vesta Science Orbits [44]

The first and highest is the survey orbit at an altitude of 3000 km. The angle between Dawn's orbital plane and the Sun-Vesta line keeps increasing as Vesta moves around the Sun. This ensured that Dawn never entered Vesta's shadow in the survey orbit. The next phase is the HAMO (High Altitude Mapping Orbit) which lies between the altitudes of 925 and 975 km. The groundtrack of HAMO repeated after every 10-orbits. Figure 2.5 illustrates the 10-orbit cycle of HAMO. Each equator crossing of the 10-orbit cycle was evenly spaced, around 36 degrees, to get uninterrupted images of Vesta's surface. The angle between the orbital plane and the Vesta-Sun line (henceforth called the  $\beta$  angle) was frozen, unlike that of the survey orbit, offering constant illumination of Vesta's surface throughout the mapping process. The third phase was the LAMO (Low Altitude Mapping Orbit) which lies between the altitudes of 405 and 521 km. Figure 2.6 illustrates the groundtrack of LAMO. The groundtrack of LAMO ensured total surface coverage in the first 60 days of entering into this orbit by keeping a 6 degree longitudinal spacing between successive equatorial crossings. The  $\beta$  angle in LAMO was frozen at a target value of 45 degree such that at the given orbital radius, the spacecraft never entered the shadow region (shadow occurred at a  $\beta$  angle of 39 degree) [44].

Just like the orbits at Vesta, Dawn had three different types of science orbits at different altitudes around Ceres, see Figure 2.7. All of the orbits at Ceres were circular and polar, going from North to South over the side which was illuminated by the Sun. Upon capture at Ceres, Dawn entered into what is known as the RC3 (Rotation Characterization 3) orbit at an altitude of 13,500 km, see Figure 2.8. The RC3 orbit helped in determining the composition of Ceres along with accurately finding its pole points. The orbital period of RC3 was 15 days. The orbit geometry was such that the spacecraft always remained in Sunlight, irrespective of the lighting condition on the surface [46]. In the RC3 orbit, as Ceres completed one full rotation around its own axis (just over 9 hours [46]), the

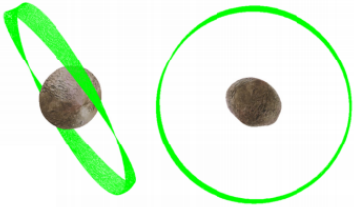


**Figure 2.5:** 10-orbit cycle of HAMO design [44].



**Figure 2.6:** Vesta Low-altitude mapping orbit [44].

spacecraft position changed by only about 10 degrees in latitude [45].

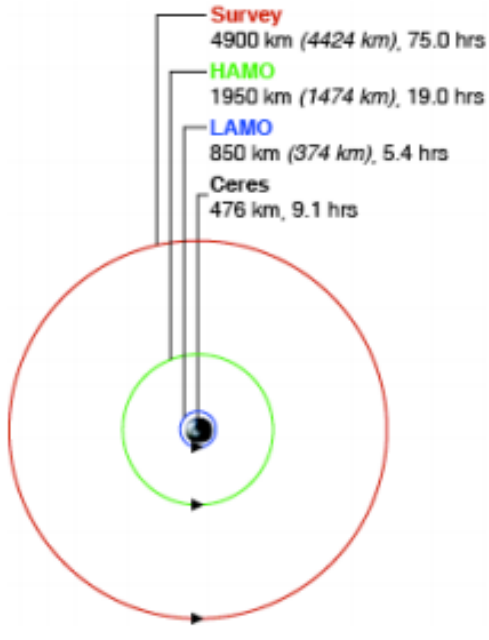


**Figure 2.7:** A schematic illustrating the three different orbit phases, their corresponding altitudes and orbital periods around Ceres. The RC3 orbit is not shown here, which was at an altitude of 13500 km [45].

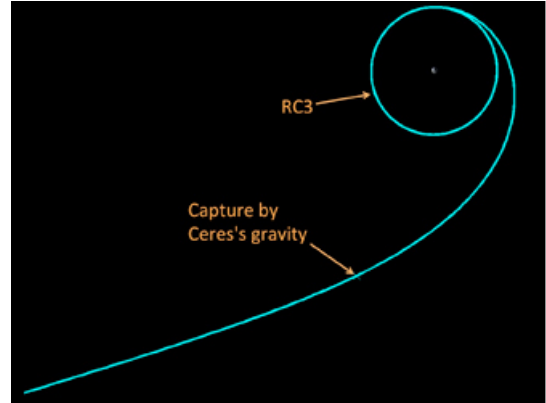


**Figure 2.8:** Following capture by Ceres' gravity, Dawn used ion propulsion to spiral down to the RC3 orbit [46].

After completing its investigations in the RC3 orbit, Dawn spiraled down to the "survey orbit" which was about 4400 km above the surface of Ceres. During this month-long decent, Dawn made only 5 revolutions around Ceres. Figure 2.9 illustrates the 5 spiral loops that Dawn traversed to reach the survey orbit. After finalizing observations in the survey orbit, Dawn spiraled down in a tighter loop to HAMO (at 1470 km) in about 30 revolutions around Ceres in a six week long trip. After performing two months of intense observations in HAMO, the spacecraft spiraled down to the final orbit called LAMO at 375 km in the most tight loop possible of 160 revolutions around Ceres in just two months of trip time [47]. Figure 2.10 illustrates the tight spiraling transfer from HAMO to LAMO.

Each revolution in the survey orbit was defined as a mapping cycle and each cycle was planned to cover different regions of Ceres. The 7 revolutions in the survey orbit achieved 95% surface coverage of Ceres [45]. Figure 2.11 shows the surface regions covered by different revolutions (or mapping cycles) in the survey orbit around Ceres. At the HAMO altitude, the spacecraft had an orbital period of 19 hours. HAMO consisted of five mapping cycles and each cycle consisted of 14 orbits and at the designated altitude for HAMO, only 12 orbits were required to give a complete coverage of the

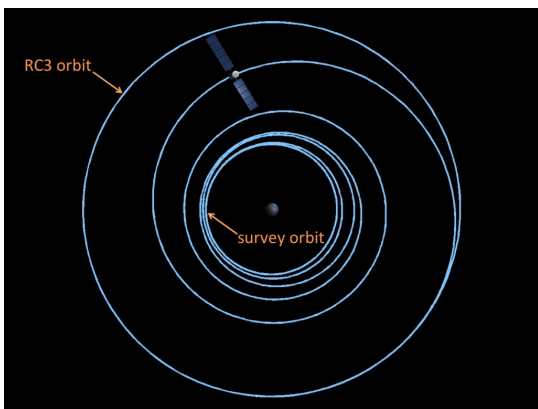


**Figure 2.9:** Spiral loop traversed by Dawn to reach survey orbit from RC3 [47].

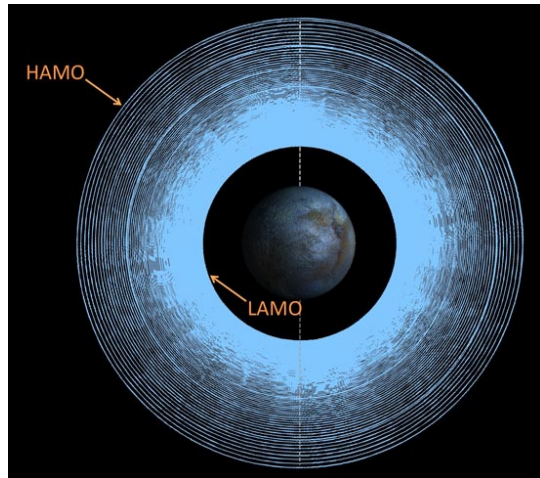


**Figure 2.10:** Tight spiral traversed by Dawn from HAMO to LAMO in 160 revolutions around Ceres [47].

surface [45]. The ground coverage by Dawn in HAMO is illustrated in Figure 2.12.

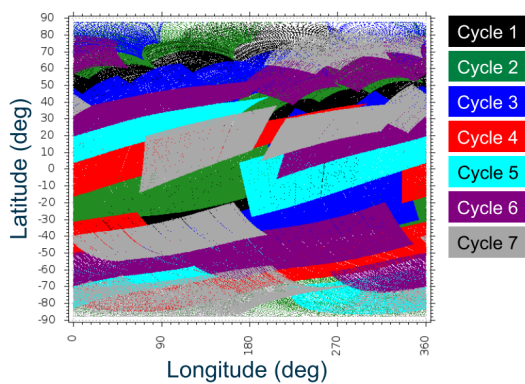


**Figure 2.11:** Ground coverage by Dawn in multiple revolutions (cycles) in the survey orbit around Ceres. Each cycle was planned to cover a different region of Ceres' surface which resulted in an irregular patchwork of observation. The overlaps in the observation between different cycles provided redundancy against data loss [45].

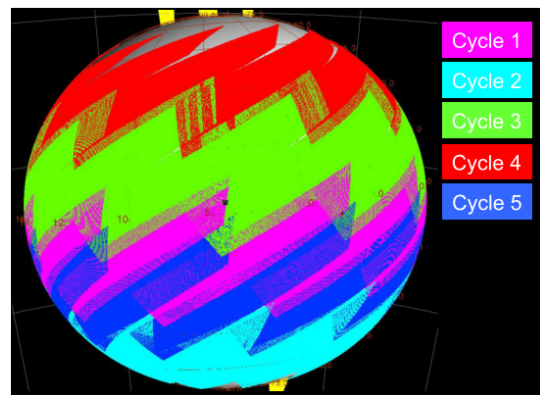


**Figure 2.12:** Ground coverage by Dawn in HAMO around Ceres. Each cycle consisted of 14 orbits and each orbit had a period twice that of the rotation period of Ceres. Each cycle was planned to cover a different latitude band [45].

Following the departure from HAMO, the spacecraft arrived at the altitude of 375 km of the LAMO, with an orbital period of 5.4 hours. The total revolutions in LAMO were divided into four cycles each with 101 orbital revolutions. Each cycle of 101 orbits was comprised of five repeating 20 orbit segments (plus one phasing orbit). The LAMO altitude selection was a major challenge for the Dawn team since hydrazine consumption (hydrazine is used on-board Dawn by the RCS (Reaction Control System) for attitude control) increased for altitudes below 1000 km. Apart from selecting the proper altitude, the orbit designers for LAMO had to ensure that the orbit can also provide dense ground coverage to meet the science objectives [45].

### 2.1.3 ROSETTA

Rosetta is a cornerstone mission of ESA's scientific program. The prime objective of the Rosetta comet rendezvous mission was in-situ observations of cometary matter. The original mission was supposed to be launched in July 2003 and reach comet Wirtanen in 2011 [21]. However, Rosetta

lost its 19 day launch window in 2003 due to suspension of Ariane 5 launches following the failure of flight 517 in 2002. A new mission opportunity was selected, soon after loosing the first launch window, which was subsequently launched in 2004 and rendezvoused with comet 67P/Churyumov-Gerasimenko (henceforth called 67P/CG) in 2014 [15].

### ORBIT AROUND COMET WIRTANEN

In case of a comet, orbit strategies cannot be fixed beforehand and are to be decided during the late comet approach phase. This is so because comet properties cannot be completely determined from Earth-based (ground and/or satellite) observations due to large distances of cometary orbit from Earth. Although Rosetta never flew to the comet Wirtanen, the following description briefly describes the preliminary orbit design for the spacecraft around the comet [21].

The sphere of influence in which the gravitational attraction of the Sun can be considered as a perturbation, given that only Earth-observed mean comet nucleus radius and density information is available, will have a size ranging from 7 to 20 times the cometary nucleus radius. Orbits near the comet can be considered as Keplerian orbits i.e. at altitudes of a few cometary radii, since the effect of a non-spherical gravity field will have minor influence on the motion of the spacecraft. Mapping of the comet would have been done with eccentric orbits around it, wherein the orbital plane would have been such that it contained the comet's spin axis and the comet-Sun line. The close observations phase was planned to consist of a sequence of eccentric orbits, all at altitudes of or below 1 cometary nucleus radius. To deliver the surface probe, the spacecraft was planned to be transferred into an elliptic orbit around the comet so that the orbiter could fly multiple revolutions without any maneuvers and obtain precise knowledge on the orbit of the spacecraft, thus ultimately leading to a good probe delivery accuracy. Following the delivery of the surface probe, the orbiter was planned to enter a relay orbit to communicate with the ground stations on Earth. Figure 2.13 illustrates the geometries of the different types of orbits around comet Wirtanen [21].

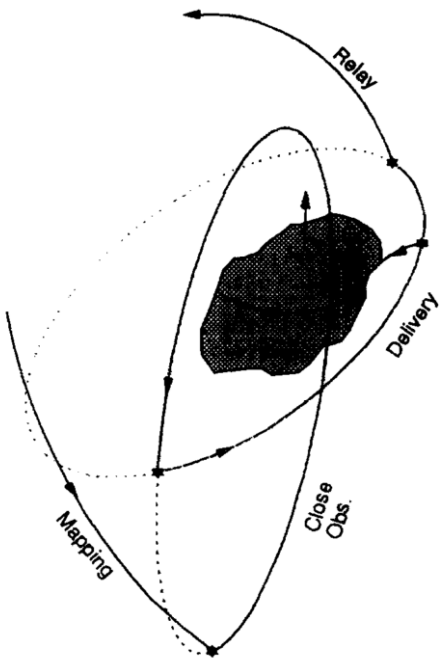


**Figure 2.13:** Rosetta orbits around comet Wirtanen [21].

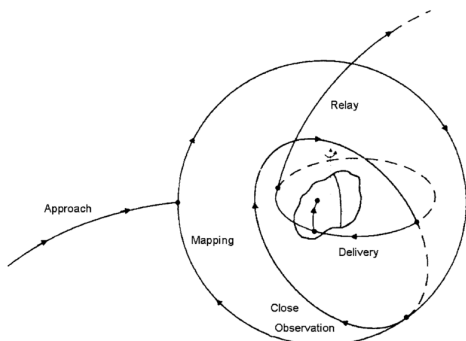


**Figure 2.14:** Schematic of Rosetta's different orbits around 67P/Churyumov-Gerasimenko [18]. Note the similarity with the preliminary orbit design of Rosetta around comet Wirtanen, depicted in Figure 2.13.

### ORBIT AROUND COMET 67P/CHURYUMOV-GERASIMENKO

We will now discuss the orbit design around the new target comet, 67P/CG. The initial orbit design, before complete cometary information of 67P/CG was known, is illustrated in Figure 2.14. At a distance of 300 times the cometary nucleus radius, the relative velocity between the spacecraft and the comet was reduced to about 1.5 m/s. At this point, landmark and radiometric measurements were performed for precise determination of the relative position and velocity of Rosetta and 67P/CG, and the gravity and rotation of the comet. The new in-situ information was then used to start the orbit insertion around the comet and initiate close proximity operations at a distance of about 60 times the cometary nucleus radius, with a relative velocity of just a few cm/s. At a distance of 25 times the cometary nucleus radius, the spacecraft was captured into a closed orbit around the comet. For global mapping of the cometary nucleus, polar orbits with altitudes ranging from 5 to 25 times the cometary nucleus radius were used. After concluding global observations, close proximity operations around the comet began in orbits with altitudes of 1 cometary nucleus radius. Based on the data collected in close proximity observations, the landing site for the Philae lander was selected. The lander was deployed from an eccentric orbit with pericenter altitude being very close to the landing site [18]. After deploying the lander, Rosetta was transferred into an orbit suitable for transmitting data back to Earth, see Figure 2.14. Now, we shall discuss the different orbits around the comet in more detail.

**Comet Initial Characterization Phase:** The objective of this phase, was for the spacecraft to fly around the comet and identify landmarks on the comet's surface, estimate its shape and rotation state and get an initial estimation of its gravitational field. This information was used to fly trajectories much closer to the surface, in the subsequent phase. The trajectory in the initial characterization phase consisted of 4 hyperbolic arcs in the shape of a pyramid, see Figure 2.15, on the day side of the comet. The first arc started at a 100 km distance, while every other arc had a pericenter distance of about 60 km. Each arc lasted for 2 days. Each orbital plane, corresponding to each of the arcs, was tilted at an angle of 45 degrees from the Sun's direction. An impulse of 0.7 m/s was required to switch between the arcs. The reason why hyperbolic arcs were selected instead of circular/elliptical ones, was that hyperbolic trajectories result in higher relative velocity between the spacecraft and the comet, which makes the trajectory more robust against insertion maneuver errors and the mis-modeling of spacecraft dynamics around the comet. Also, with faster arcs, the comet can be observed in shorter time [39].

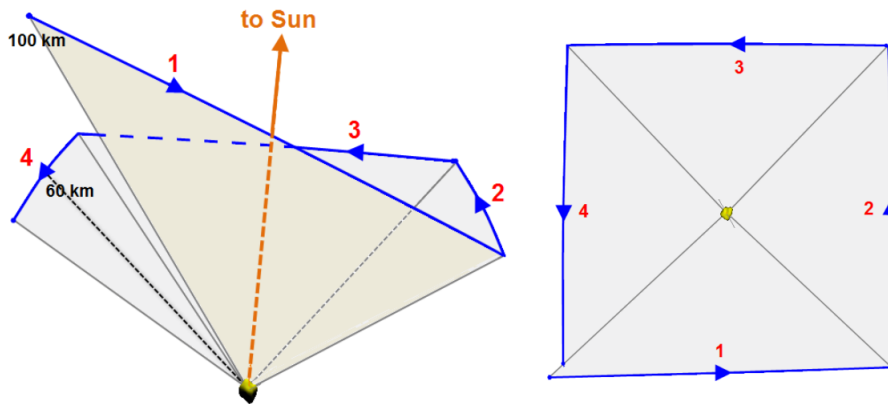
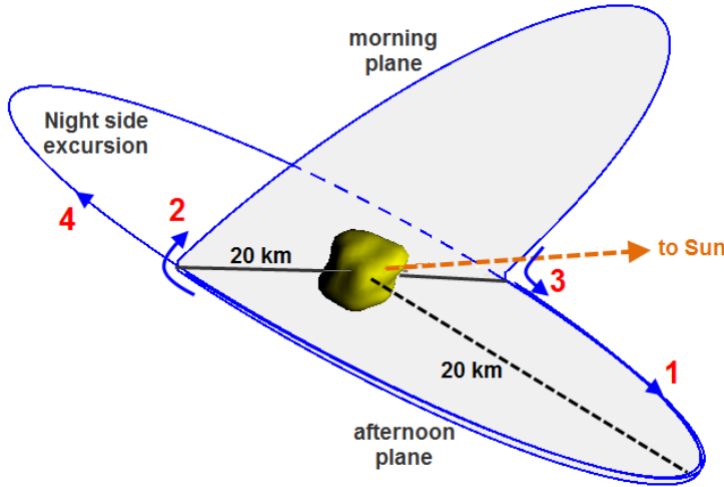


Figure 2.15: Geometry of Rosetta's initial characterization phase around 67P/CG [39].

**Global Mapping Phase:** This phase was planned to improve upon the knowledge on dynamical properties and kinematics of the comet. The selected trajectory, see Figure 2.16, consists of four 180-degree arcs of circular polar orbit, each having a radius of 20 km. These arcs are found in two orbital planes each having a 30 degree inclination from the Sun direction, to avoid eclipses. To keep

the spacecraft on the day-side of the comet, the transfer maneuver from one arc to the other were performed when the spacecraft was above the poles of the comet. By skipping one maneuver (i.e. instead of a 180 degree arc, the spacecraft completes the whole 360 degree orbit), in either plane, a night-side excursion of the comet is also possible. Each maneuver to shift between the arcs also changes the orbital plane from morning to afternoon and vice-versa [39], see Figure 2.16.



**Figure 2.16:** Geometry of Rosetta's global mapping phase around 67P/CG [39].

**Close Observation Phase:** This phase was used to select candidate landing sites (for the Philae lander) based on the information obtained in the previous phase. Accurate information on spacecraft navigation was required to allow the instruments to point towards the candidate landing sites. This information was obtained by executing a trajectory around the comet without any impulsive maneuvers because any uncertainty in maneuver performance would have lead to degradation of navigation knowledge around the comet. One of the mission requirements was to have continuous optical observations of the comet and hence any trajectory to the night-side of the comet was avoided. The candidate landing sites were observed from a circular orbit of 10 km radius lying in the daylight terminator plane around the comet to avoid night-side excursions. A terminator plane is one where the spacecraft flies above the day-night line, in this case, on the comet's surface. After determination of one of the candidate landing sites, an orbit closer to the surface was selected to observe the landing site at the pericentre passage. This orbit was elliptical with the apocentre at 10 km radius and pericentre at 5 km radius [39]. Figure 2.17 illustrates the orbits of the close observation phase. The reader is advised to scan the QR code given in Figure 2.18 to view the trajectory animation by ESA for the initial characterization, global mapping, and the close observation phases.

**Lander Delivery Phase:** In this phase, Rosetta entered into a trajectory from which the lander was deployed towards the comets' surface. The spacecraft was initially in an orbit similar to the one in the close observation phase. It was maneuvered and put into a hyperbolic trajectory and soon after the lander was separated [39]. Figure 2.20 illustrates the geometry of the trajectory and the lander separation point. The reader is also advised to scan the QR code given in Figure 2.19 to view the trajectory animation by ESA for the lander delivery phase.

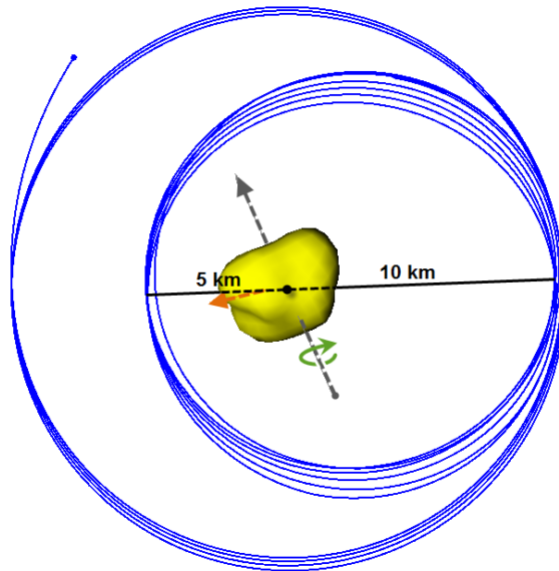


**Figure 2.17:** Geometry of Rosetta's close observation phase around 67P/CG [39].



**Figure 2.18:** Animation by ESA depicting Initial characterization, global mapping and close observation phases. Scan the QR code to view the trajectory animation or visit the following web-link: <https://www.youtube.com/watch?v=fNBUep7mPdI&feature=youtu.be>



**Figure 2.19:** Animation by ESA depicting lander delivery phase of Rosetta. Scan the QR code to view the trajectory animation or visit the following web-link: <https://www.youtube.com/watch?v=4a3eY5siRRk&feature=youtu.be>

#### 2.1.4 NEAR

The NEAR (Near Earth Asteroid Rendezvous) mission was designed to study the near-Earth Asteroid Eros from a close orbit over a period of one year. The NEAR spacecraft was launched in 1996, and with an Earth swingby in January 1998, the spacecraft was targeted towards Eros. However due to a main engine abort in December 1998, a fly-by of Eros was performed and a rendezvous was rescheduled for the year 2000 [3].

Figure 2.21 illustrates a schematic of the geometry of the low-altitude circular orbit around Eros as viewed from the Sun. The orbital plane is always within 30 degrees of a plane which is perpendicular to the Eros-Sun line, so as to orient the spacecraft's fixed solar panel towards the Sun. In part (a) of Figure 2.21, the spacecraft is in a circular equatorial orbit with its spin axis aligned with the Eros-Sun line. The south pole of Eros is facing the Sun and the spacecraft orbit is retrograde. Part (b) of Figure 2.21 denotes the earlier part of the orbital mission wherein the asteroid rotation axis was perpendicular to the Eros-Sun line and the spacecraft orbit was in a polar orbit [3].

Figure 2.22 shows the mission profile of the NEAR spacecraft in terms of its distance from the asteroid and inclination of its orbital plane from the asteroid's equator while it was in a close circular orbit. The long duration of NEAR in a polar orbit at a range of 50 km was designed to permit the

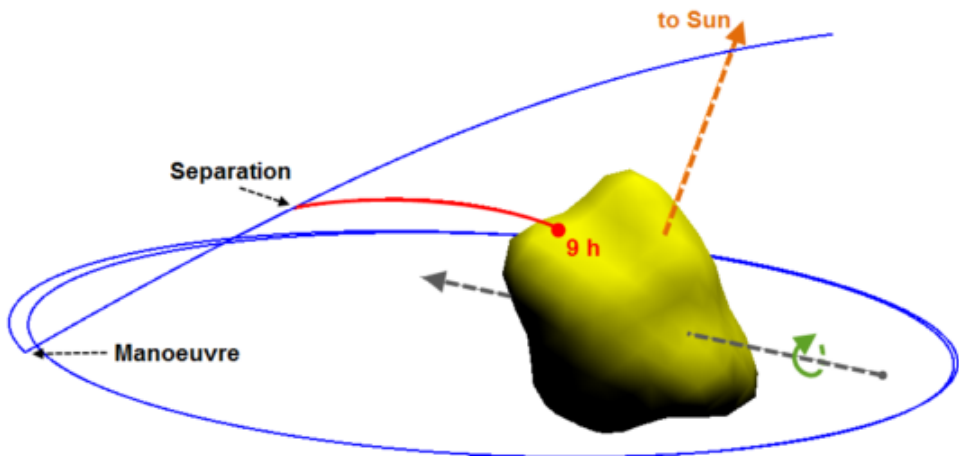


**Figure 2.20:** Geometry of Rosetta's lander delivery phase to 67P/CG [39].

most comprehensive mapping of Eros. The low-altitude retrograde orbit towards the end of mission profile was designed to extensively map the equatorial region of Eros [9].

The methodology adopted for orbit design of the NEAR mission was to compute a maneuver that satisfied a local set of constraints and performance criteria and then propagate the trajectory to see where it goes. This differs substantially from the traditional approach of defining a number of constraints and then obtaining a trajectory that is a global minimum of some performance criteria [22]. From the orbit design approach adopted by the NEAR mission designers, it can be inferred that their approach allows a relatively simple way to compute trajectories, because instead of solving for global constraints that are defined for all the scientific objectives, they solved for orbits under local constraints pertaining to fewer or even singular scientific objectives at a time and then repeated this step-by-step process until all scientific objectives were met. Although this approach will provide locally optimum trajectories, it is not necessary that these trajectories would also be globally optimum.

## 2.2 FUTURE MISSIONS

This section will discuss the missions proposed or planned for the future.

### 2.2.1 OSIRIS-REX

In September 2016, the OSIRIS-REx spacecraft will be launched to rendezvous with asteroid Bennu. After arriving at the asteroid in 2018, it will conduct observations to select a suitable site from where it will retrieve a sample of the asteroid and return it to Earth in 2023 [2].

The mission design of OSIRIS-REx consists of a preliminary survey phase that comprises of three hyperbolic passes over the North and South poles and the equator at a distance of 7 km from the centre of the asteroid, see Figure 2.23. These passes will determine information about the asteroid which will be necessary in planning the propulsive maneuvers to place the spacecraft in an orbit around it [2].

After the preliminary survey phase, the spacecraft will enter into an orbit at a distance of 1.5 km (Orbital A) from the centre of the asteroid. In Orbital A, the spacecraft will transition to landmark based optical navigation. The spacecraft will also perform high resolution science imaging during Orbital A phase to improve topographic maps and shall also determine the rotation state of the asteroid [2].

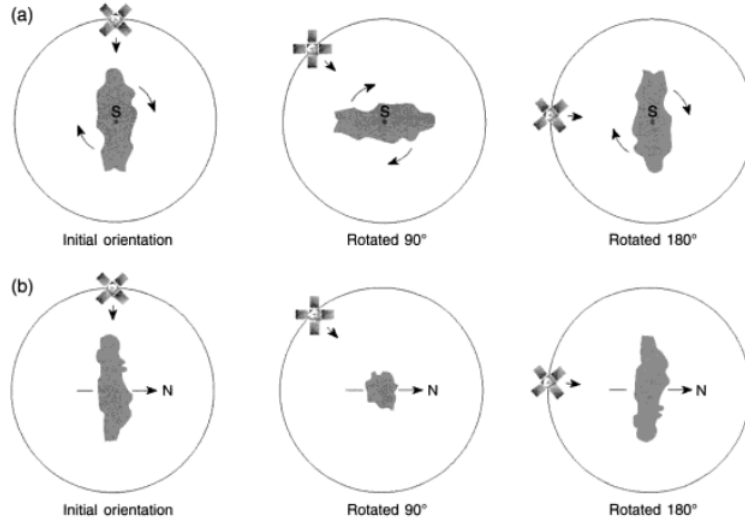


**Figure 2.21:** Orbital geometries around Eros, as viewed from the Sun. The arrow near the spacecraft marks the instrument bore-sight. (a) Spacecraft is in a retrograde equatorial orbit and the south pole of Eros is denoted by 'S'. (b) Spacecraft is in a polar orbit and the arrow going through the asteroid denotes its spin axis [3].

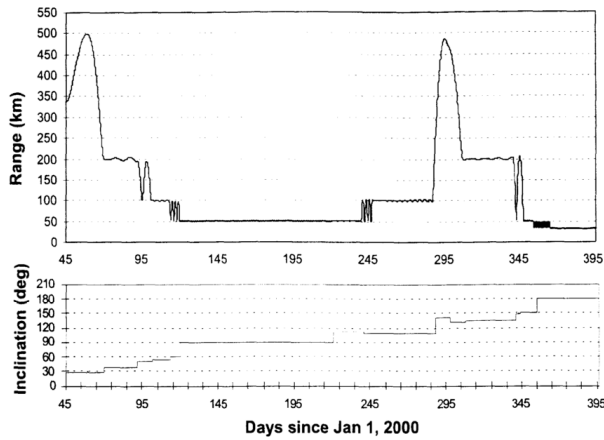


**Figure 2.22:** Range and Inclination in orbit phase around Eros [9].

Following the Orbital A phase, comes the final leg in the global investigation of Bennu, the detailed survey phase consisting of multiple hyperbolic passes of Bennu. The first of these passes will be at a distance of 3.5 km from the centre of the asteroid and transit over four sub-satellite points at 40 degrees latitude (both North and South) and at 10 AM and 2 PM local time at the surface of Bennu. Following this, the spacecraft will traverse in seven passes at an altitude of 5 km from the surface of the asteroid. These passes fly through points above the equator spaced over multiple local times of day on the surface, see Figure 2.24. The end of the detailed survey phase will result in an initial selection of 12 candidate sites from where a sample of the asteroid could potentially be collected [2].

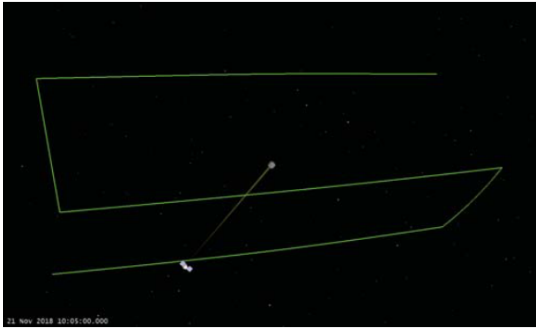


**Figure 2.23:** Hyperbolic passes over both the poles and the equator, as part of the preliminary survey of asteroid Bennu [2].

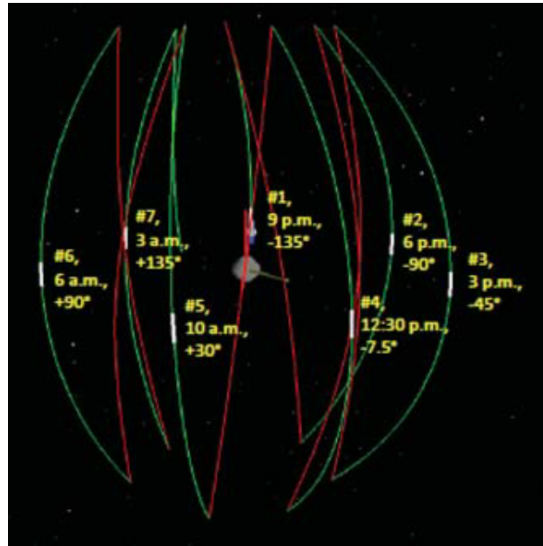


**Figure 2.24:** Multiple passes through points above the equator of Bennu, as part of the detailed survey of the asteroid [2].

Following the Detailed Survey phase, the spacecraft will perform a site-specific reconnaissance mission on the initial selection of candidate sampling sites. To do this the spacecraft will enter into a 1 km orbit (Orbital B) around Bennu. This phase will conclude with the selection of two primary and two secondary sites. The two primary sites will be observed again from an altitude of 225 m above the surface of the asteroid to get high-resolution images of the surface [2].

### 2.2.2 AIDA

The AIDA (Asteroid Impact and Deflection Assessment) mission will be the first of its kind to demonstrate a mitigation technique to protect Earth from an asteroid impact by performing a spacecraft kinetic impact on the asteroid to deflect it from its trajectory. AIDA is an international collaboration between ESA and NASA. Both space agencies will provide independent but mutually supporting missions. NASA will provide the asteroid kinetic impactor spacecraft under its DART (Double Asteroid Redirection Test) mission and ESA will provide the asteroid characterization spacecraft under its AIM (Asteroid Impact Mission). The AIDA target will be the binary asteroid Didymos and the deflection experiment will take place in late 2022 [6]. Figure 2.25 shows the heliocentric trajectory of Didymos along with that of Earth and other inner solar system planets.

Since this literature survey report is focused on the design of orbits around asteroids, hence this subsection shall present information on the AIM part of the AIDA mission. AIM shall start the observation of the Didymos binary system from a formation-flying quasi periodic orbit at an altitude of 35 km which is outside the sphere of influence of both asteroids in the Didymos system. This station point will be within the orbital plane of the asteroid around the Sun but it will be offset by around 45 degrees from the direction towards the Sun. This ensures that the spacecraft will always be positioned above the illuminated face of the asteroid. To perform a more detailed characterization of the asteroid, a second observation station point is selected at a 10 km altitude. Finally, as part of the AIDA mission scenario, the DART impactor will be observed from a safe distance of 100 km from Didymos to avoid any damage from the impact debris [6].

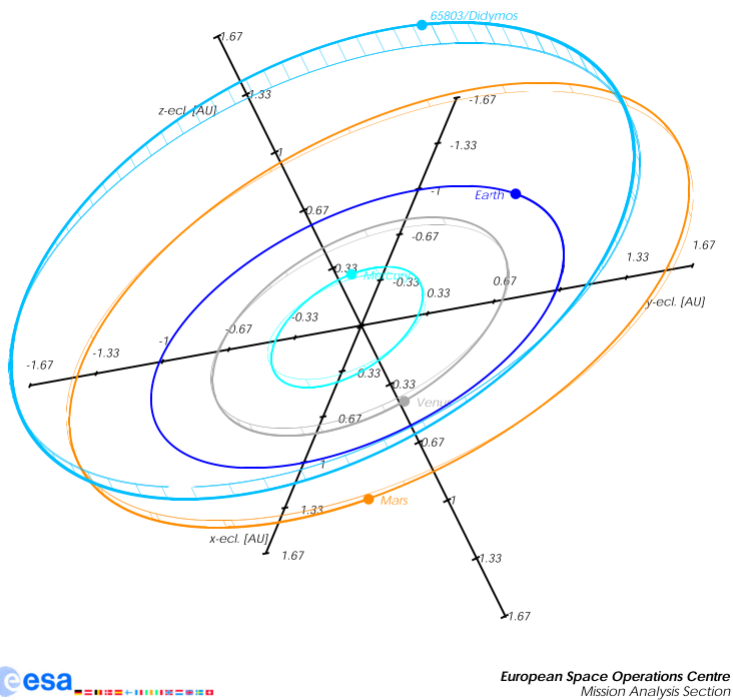


**Figure 2.25:** Heliocentric orbit of the Didymos system [6].

## 2.3 CONCLUSION

In this chapter we discussed a few missions to asteroids that were conducted in the past, some which are being conducted presently, and some that will be conducted in the future. The idea behind writing this chapter, was to understand the approach that has been adopted for different mission scenarios, to gather any common elements, and to understand the reasons behind following a particular approach to orbit design. The inferences drawn from studying the various missions are listed as follows:

- The design of all propulsive maneuvers and all the trajectories in between those maneuvers, are always driven by the scientific objectives and spacecraft constraints, not the other way around.
- Since the dynamical environment around small bodies such as asteroids and comets is not always known to a very high accuracy, due to the inability to perform the required observations at such large distances from Earth, a common approach to orbit design involves breaking down the mission into multiple phases in terms of the altitudes of the orbits around the small body. For example, before planning maneuvers and designing orbits for close proximity operations, the spacecraft would first map the rotation rates, composition, and gravitational attraction of the small body from a relatively large distance in what is usually defined as a survey orbit, and then proceed to lower altitudes gradually to perform the scientific objectives.
- Due to relatively low gravitational attraction of asteroids and comets, it is always possible to design trajectories around the small body which involves multiple propulsive maneuvers since the cost of these maneuvers is small.



# 3

## MODELING THE GRAVITATIONAL POTENTIAL OF A SMALL IRREGULAR BODY

### 3.1 INTRODUCTION

Before we study the motion of the binary asteroid system or the motion of the spacecraft in the environment of the binary system, it is necessary to define and model the gravitational potential for a small irregular body. Large celestial bodies in the Solar System such as the planets and their moons have, approximately, a spherical shape because the strong gravitational field (due to the large mass of these celestial bodies) has reshaped them into spheres. Unlike the planets and most of their moons, smaller celestial bodies such as asteroids and comets have relatively smaller mass leading to a weaker gravitational field that could not break the material strength to reshape these bodies into spheres. Thus, asteroids and comets are characterized by irregular shapes and consequently an irregular gravitational field [56]. This chapter will give a brief description on the different ways in which the gravitational potential of a small irregular body can be modeled.

### 3.2 SPHERICAL HARMONICS MODEL

Consider a point  $P$  (see Figure 3.1), outside a small irregular body (henceforth generalized as an asteroid) corresponding to the position vector  $\mathbf{r}$  defined as:

$$\mathbf{r} = x\hat{\mathbf{x}} + y\hat{\mathbf{y}} + z\hat{\mathbf{z}} \quad (3.1)$$

The frame of reference, for all discussions, has its axes aligned with the principal moments of inertia and the origin is at the centre of mass of the body. The spherical coordinates corresponding to Equation (3.1) are defined as [52]:

$$r = \sqrt{x^2 + y^2 + z^2} \quad (3.2)$$

$$\delta = \sin^{-1} \frac{z}{r} \quad (3.3)$$

$$\lambda = \tan^{-1} \frac{y}{x} \quad (3.4)$$

where  $\delta$  and  $\lambda$  are latitude and longitude of the external point, respectively, and  $r$  is the magnitude of the position vector. Given the above definitions, the general form for the spherical harmonics gravitational potential is given as [52]:

$$U(r, \delta, \lambda) = \frac{\mu}{r} \sum_{l=0}^{\infty} \sum_{m=0}^l \left( \frac{r_0}{r} \right)^l P_{lm}(\sin \delta) [C_{lm} \cos(m\lambda) + S_{lm} \sin(m\lambda)] \quad (3.5)$$

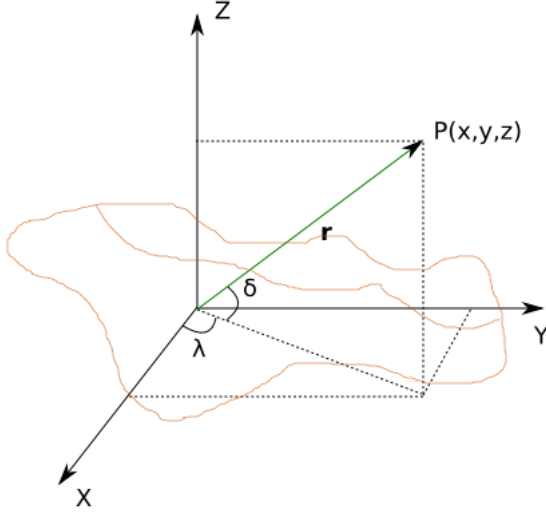


**Figure 3.1:** Schematic illustrating an irregular body and a point outside this body, denoted as  $P$ , where the spherical harmonics potential for the gravity field has to be calculated.

Where  $\mu = GM$  is the gravitational parameter of the asteroid and  $r_0$  is the normalizing radius which is often chosen as the largest radius of the irregularly shaped asteroid or its mean radius [52].  $P_{lm}$  are the Associated Legendre Function, of degree  $l$  and order  $m$ .  $C_{lm}$  and  $S_{lm}$  are called the gravity field harmonic coefficients and they describe the dependence of the potential function on a body's internal mass distribution [36] and [52]. The Associated Legendre Functions are defined as [31] and [52]:

$$P_{lm}(\sin \delta) = \cos^m \delta \sum_{i=0}^k T_{lmi} \sin^{l-m-2i} \delta \quad (3.6)$$

$$T_{lmi} = \frac{(-1)^i (2l-2i)!}{2^i i! (l-i)! (l-m-2i)!} \quad (3.7)$$

where  $k$  is the integer part of the term  $(l-m)/2$ . Explicit formulas for the Associated Legendre Functions upto a degree and order of 2 can be found in [36] (Section 3.2.1, Table 3.1 in [36]). Another method, a recursive method, that is practically used to compute the Associated Legendre functions of any degree ( $l$ ) and order ( $m$ ), with  $m < l$ , is given as follows [60]:

$$(l+1)P_{(l+1),0}(x) = (2l+1)xP_{l,0}(x) - lP_{(l-1),0}(x) \quad (3.8)$$

$$P_{l,l}(x) = (2l-1)\sqrt{1-x^2}P_{(l-1),(l-1)}(x) \quad (3.9)$$

$$P_{l,(l-1)} = (2l-1)xP_{(l-1),(l-1)}(x) \quad (3.10)$$

$$P_{l,m}(x) = \frac{2l-1}{l-m}xP_{(l-1),m}(x) - \frac{l+m-1}{l-m}P_{(l-2),m}(x) \quad (3.11)$$

The recursive relations use the starting values  $P_{0,0}(x) = 1$  and  $P_{1,0}(x) = x$  [60]. Equation (3.8) corresponds to the value of the Associated Legendre Function for the zonal harmonics, Equation (3.9) corresponds to the value for the sectorial harmonics, and similarly, Equation (3.10) and Equation (3.11) corresponds to the value for the tesseral harmonics [60]. The zonal harmonics ( $l \neq 0, m = 0$ ) in the spherical harmonics potential function for the gravity field, represent the influence of variations in mass density distribution and shape of a body in the north-south direction i.e. the potential changes with the latitude but not with the longitude. The sectorial harmonics ( $l = m \neq 0$ ) represent influence of variation in the mass density and shape of the body in the east-west direction i.e. the potential

changes with the longitude but not with the latitude. Finally, the tesseral harmonics ( $l \neq m \neq 0$ ) represent the influence of the variation in mass density and shape of the body in both the east-west and north-south direction i.e. the potential changes with both the latitude and longitude [60]. An equation representing the zonal, sectorial and tesseral harmonic parts in the potential function can be found in [60] and is not repeated here.



**Figure 3.2:** Schematic illustrating the zonal harmonics (left), the sectorial harmonics (centre), and the tesseral harmonics (right) [60].

The integral formulas for the gravity coefficients  $C_{lm}$  and  $S_{lm}$  are given in [36] (see Section 3.2.1, Equation 3.11 in [36]) and also in [52] (see Equation 2.15 in [52]). The integral expressions for the gravity coefficients are complicated but the solution of the integrals for some lower degree and order cases is well explained in [36] (see Section 3.2.2 in [36]).

#### LOWER DEGREE AND ORDER SPHERICAL HARMONICS GRAVITY FIELD COEFFICIENTS

From the integrand expression for  $C_{lm}$  it can easily be evaluated that  $C_{00} = 1$ . From the integrand expression for  $S_{lm}$ , we know that all  $S_{l0}$  terms will be zero since for  $m = 0$ , the  $\sin(m\lambda)$  term in the integral evaluates to zero [36]. The first degree and order gravity coefficients are all related to the centre of mass of the body and the corresponding expressions are given as follows [52]:

$$x_{CM} = C_{11}r_0 \quad (3.12)$$

$$y_{CM} = S_{11}r_0 \quad (3.13)$$

$$z_{CM} = C_{10}r_0 \quad (3.14)$$

where  $(x_{CM}, y_{CM}, z_{CM})$  are the coordinates of the centre of mass of the irregular body in the body fixed frame, and  $r_0$  is the largest radius or the mean radius of the irregular body. By coinciding the origin of the frame with the centre of the mass i.e.  $(x_{CM}, y_{CM}, z_{CM}) = (0, 0, 0)$ , the three coefficients can be made zero i.e.  $C_{11} = S_{11} = C_{10} = 0$ . These coefficients however will not be zero if the irregular body does not have a constant density [52].

Now the second degree and order gravity coefficients are related to the body's principle moments of inertia and the products of inertia [52]. The ones related to the product of inertia are given as follows [52]:

$$I_{xy} = -2Mr_0^2S_{22} \quad (3.15)$$

$$I_{yz} = -Mr_0^2S_{21} \quad (3.16)$$

$$I_{xz} = -Mr_0^2C_{21} \quad (3.17)$$

where  $M$  is the total mass of the irregular body. By aligning the axes of the body fixed coordinate frame with the principle moments of inertia, the products of inertia become zero, thereby making  $S_{22} = S_{21} = C_{21} = 0$ .

Thus, the simplest form of the spherical harmonics potential for the gravity field of a body can be defined with only the second degree and order coefficients  $C_{20}$  and  $C_{22}$ . These two coefficients also account for the majority of the gravitational perturbation acting on a dynamical system [52].

This simplified gravity potential expression is given as [52]:

$$U = \frac{\mu}{r} \left[ 1 + \left( \frac{r_0}{r} \right)^2 \left[ C_{20} \left( 1 - \frac{3}{2} \cos^2 \delta \right) + 3C_{22} \cos^2 \delta \cos(2\lambda) \right] \right] \quad (3.18)$$

### 3.3 ELLIPSOID HARMONICS MODEL

The equation for a fundamental ellipsoid (henceforth called the reference ellipsoid  $\varepsilon_0$ ) is given as [49]:

$$\frac{x^2}{a^2} + \frac{y^2}{b^2} + \frac{z^2}{c^2} = 1 \quad (3.19)$$

where  $a \geq b \geq c$  and  $a, b, c$  are the semi-major axes of  $\varepsilon_0$ . Analogous to the Spherical Harmonics,  $\varepsilon_0$  will always be the smallest ellipsoid enclosing the entire small irregular body [49]. The equation for a family of quadrics, confocal to  $\varepsilon_0$  is written as [7]:

$$\frac{x^2}{a^2 + s^2} + \frac{y^2}{b^2 + s^2} + \frac{z^2}{c^2 + s^2} = 1 \quad (3.20)$$

where  $s$  in Equation (3.20) is a variable; by changing its value a family of quadrics (ellipsoid, hyperboloid of one sheet, or hyperboloid of two sheets [43]) can be generated that will have the same foci as  $\varepsilon_0$ . Lets define  $h, k$  which are two constants such that  $0 < h < k$  and introduce a change of variable called  $\lambda$ :

$$h^2 = a^2 - b^2 \quad (3.21)$$

$$k^2 = a^2 - c^2 \quad (3.22)$$

$$\lambda^2 = a^2 + s^2 \quad (3.23)$$

The quantities  $h, k$  are two focal lengths of  $\varepsilon_0$ . In light of the new terms and their definitions, Equation (3.20) can be re-written as:

$$\frac{x^2}{\lambda^2} + \frac{y^2}{\lambda^2 - h^2} + \frac{z^2}{\lambda^2 - k^2} = 1 \quad (3.24)$$

Equation (3.24) has three real roots denoted as  $\lambda_1^2, \lambda_2^2, \lambda_3^2$ , where  $\lambda_1, \lambda_2, \lambda_3$  are called ellipsoidal coordinates. The latter are related to the Cartesian coordinates by the following relations [7]:

$$x^2 = \frac{\lambda_1^2 \lambda_2^2 \lambda_3^2}{h^2 k^2} \quad (3.25)$$

$$y^2 = \frac{(\lambda_1^2 - h^2)(\lambda_2^2 - h^2)(h^2 - \lambda_3^2)}{h^2(k^2 - h^2)} \quad (3.26)$$

$$z^2 = \frac{(\lambda_1^2 - k^2)(k^2 - \lambda_2^2)(k^2 - \lambda_3^2)}{k^2(k^2 - h^2)} \quad (3.27)$$

Because the Cartesian coordinates are related to the ellipsoidal coordinates in a square power, there will be 8 cartesian points corresponding to the same values of  $\lambda_1^2, \lambda_2^2, \lambda_3^2$ . In order to have a one to one relation between the cartesian and ellipsoidal coordinates, certain restrictions have to be imposed which are provided in [7] (section 1.1).

Consider a small irregular asteroid body enclosed by the smallest possible reference ellipsoid  $\varepsilon_0$  which has a largest semi-major axis denoted by  $\lambda_1^{ref}$ . Then the potential for the interior space of the ellipsoid is given as follows [7]:

$$U(\lambda_1, \lambda_2, \lambda_3) = \mu \sum_{n=0}^{\infty} \sum_{p=1}^{2n+1} \alpha_{np} \frac{E_n^p(\lambda_1)}{E_n^p(\lambda_1^{ref})} E_n^p(\lambda_2) E_n^p(\lambda_3) \quad (3.28)$$

such that  $\lambda_1 \leq \lambda_1^{ref}$ . Equation (3.28) is also called as the Surface Ellipsoidal Harmonics expansion. In Equation (3.28),  $n$  and  $p$  define the degree and order, respectively, of the potential expansion;  $\mu$  defines the gravitational parameter of the small irregular asteroid body;  $a_{np}$  is called the Ellipsoidal Harmonic Coefficient;  $E_n^p$  are called Lamé's function of the first kind. The latter are divided into four types, defined as follows [7]:

$$K_n^p(\lambda_i) = a_{0p}\lambda_i^n + a_{1p}\lambda_i^{n-2} + \dots + \begin{cases} a_{\sigma p}: & \text{for } n \text{ even} \\ a_{\sigma p}\lambda_i: & \text{for } n \text{ odd} \end{cases} \quad (3.29)$$

$$L_n^p(\lambda_i) = \sqrt{|\lambda_i^2 - h^2|} \times \left[ b_{0p}\lambda_i^{n-1} + b_{1p}\lambda_i^{n-3} + \dots + \begin{cases} b_{n-\sigma-1,p}\lambda_i: & \text{for } n \text{ even} \\ b_{n-\sigma-1,p}: & \text{for } n \text{ odd} \end{cases} \right] \quad (3.30)$$

$$M_n^p(\lambda_i) = \sqrt{|\lambda_i^2 - k^2|} \times \left[ c_{0p}\lambda_i^{n-1} + c_{1p}\lambda_i^{n-3} + \dots + \begin{cases} c_{n-\sigma-1,p}\lambda_i: & \text{for } n \text{ even} \\ c_{n-\sigma-1,p}: & \text{for } n \text{ odd} \end{cases} \right] \quad (3.31)$$

$$N_n^p(\lambda_i) = \sqrt{(|\lambda_i^2 - h^2|)(|\lambda_i^2 - k^2|)} \times \left[ d_{0p}\lambda_i^{n-2} + d_{1p}\lambda_i^{n-4} + \dots + \begin{cases} d_{\sigma-1,p}: & \text{for } n \text{ even} \\ d_{\sigma-1,p}\lambda_i: & \text{for } n \text{ odd} \end{cases} \right] \quad (3.32)$$

where  $i = 1, 2, 3$  and signifies the index number for the three ellipsoidal coordinates;  $K, L, M, N$  are the four types of Lamé's function of first kind;  $a_{0p}, a_{1p}, \dots, b_{0p}, b_{1p}, \dots, c_{0p}, c_{1p}, \dots, d_{0p}, d_{1p}$  are the polynomial coefficients and:

$$\sigma = \begin{cases} \frac{n}{2}: & \text{for } n \text{ even} \\ \frac{n-1}{2}: & \text{for } n \text{ odd} \end{cases} \quad (3.33)$$

For a given value for the degree of expansion,  $n$ , the  $E_n^p$  is shared among the four types of Lamé's function in the following manner [7]:

- $(\sigma + 1)$  are of type  $K$  for  $p = 1, \dots, (\sigma + 1)$
- $(n - \sigma)$  are of type  $L$  for  $p = (\sigma + 2), \dots, (n + 1)$
- $(n - \sigma)$  are of type  $M$  for  $p = (n + 2), \dots, (2n - \sigma + 1)$
- $\sigma$  are of type  $N$  for  $p = (2n - \sigma + 2), \dots, (2n + 1)$

Thus depending on what the value of the order,  $p$ , is at a given instant of evaluation in Equation (3.28), the appropriate type of Lamé's function is chosen for the term  $E_n^p$ .

In a similar way, the potential outside the ellipsoid  $\lambda_1 = \lambda_1^{ref}$  is defined as [7]:

$$U(\lambda_1, \lambda_2, \lambda_3) = \mu \sum_{n=0}^{\infty} \sum_{p=1}^{2n+1} \alpha_{np} \frac{F_n^p(\lambda_1)}{F_n^p(\lambda_1^{ref})} E_n^p(\lambda_2) E_n^p(\lambda_3), \forall \lambda_1 \geq \lambda_1^{ref} \quad (3.34)$$

where  $F_n^p$  is Lamé's function of the second kind and all other terms have the same meaning as defined earlier for Equation (3.28).  $F_n^p$  is defined as follows [7]:

$$F_n^p(\lambda_1) = (2n+1)E_n^p(\lambda_1) \int_{\lambda_1}^{\infty} \frac{du}{(E_n^p(u))^2 \sqrt{(u^2 - k^2)(u^2 - h^2)}} \quad (3.35)$$

where  $u$  is just an integration variable. Of course at the boundary  $\lambda_1 = \lambda_1^{ref}$ , Equation (3.28) and Equation (3.34) have the same expression so that the potential is continuous [7].

It is often preferred to use a normalized expression for a gravitational potential, mainly because normalization helps to simplify these expressions and avoids combination of large and small numerical quantities in computations, such as multiplication. The normalization constant (the use of the normalization constant is shown in Equation (3.39) and Equation (3.40)) is shown here without any derivation [7]:

$$\gamma_n^p = 8 \times \int_0^h \int_h^k \frac{(\lambda_2^2 - \lambda_3^2)(E_n^p(\lambda_2)E_n^p(\lambda_3))^2}{\sqrt{(k^2 - \lambda_2^2)(\lambda_2^2 - h^2)(h^2 - \lambda_3^2)(k^2 - \lambda_3^2)}} d\lambda_2 d\lambda_3 \quad (3.36)$$

Thus the normalized ellipsoidal harmonic expansion of the gravitational potential are expressed as:

$$U(\lambda_1, \lambda_2, \lambda_3) = \mu \sum_{n=0}^{\infty} \sum_{p=1}^{2n+1} \overline{\alpha_{np}} \frac{E_n^p(\lambda_1)}{E_n^p(\lambda_1^{ref})} \overline{E_n^p(\lambda_2)} \overline{E_n^p(\lambda_3)}, \forall \lambda_1 \leq \lambda_1^{ref} \quad (3.37)$$

$$U(\lambda_1, \lambda_2, \lambda_3) = \mu \sum_{n=0}^{\infty} \sum_{p=1}^{2n+1} \overline{\alpha_{np}} \frac{F_n^p(\lambda_1)}{F_n^p(\lambda_1^{ref})} \overline{E_n^p(\lambda_2)} \overline{E_n^p(\lambda_3)}, \forall \lambda_1 \geq \lambda_1^{ref} \quad (3.38)$$

$$\overline{E_n^p(\lambda_2)} \overline{E_n^p(\lambda_3)} = \frac{E_n^p(\lambda_2)E_n^p(\lambda_3)}{\sqrt{\gamma_n^p}} \quad (3.39)$$

$$\overline{\alpha_{np}} = \alpha_{np} \sqrt{\gamma_n^p} \quad (3.40)$$

The ellipsoidal harmonic coefficient  $\alpha_{np}$  can be expressed as a linear transformation of the spherical harmonics coefficients  $C_{lm}$  and  $S_{lm}$  as follows [7]:

$$\overline{\alpha_{np}} = \sum_{l=0}^{\infty} \sum_{m=0}^l (A_{np}^{lm} \cdot C_{lm} + B_{np}^{lm} \cdot S_{lm}) \quad (3.41)$$

where  $l$  and  $m$  represent the degree and order from the spherical harmonic expansion;  $A_{np}^{lm}$  and  $B_{np}^{lm}$  represent the transformation coefficients. Depending on the type (even or odd) of  $l, m, n, p$ , the various values of the transformation coefficients are given in reference [7] (section 2.3.2.2) which shall be used in the computation of the ellipsoidal harmonic expansion of the gravitational potential for an irregularly shaped asteroid body.

### 3.4 ELLIPTIC INTEGRAL MODEL

Before we can begin with the expressions for the gravitational potential for an elliptic integral, we will have to revisit the theory of ellipsoidal coordinates. This is necessary since the theory shall be presented in a different manner compared to that in Section 3.3 because unlike in that section, the theory presented here shall result in the formulation of a one-to-one relation between cartesian and ellipsoidal coordinates without the involvement of external conditions or restrictions. The theory for this section has mainly been derived from a previous research work given in [43] and the reader is strongly advised to refer [43] for more details.

$$\frac{x^2}{a^2 + s^2} + \frac{y^2}{b^2 + s^2} + \frac{z^2}{c^2 + s^2} = 1 \quad (3.42)$$

Equation (3.42) is a cubic equation ( $a \geq b \geq c$ ) in  $s$  and has three unequal real roots in  $s$  denoted here as  $s_1, s_2, s_3$ . The latter are also called ellipsoidal coordinates as described in [43]. Note that the form of ellipsoidal coordinates mentioned here as  $s_1, s_2, s_3$  is not the same as that of  $\lambda_1, \lambda_2, \lambda_3$

mentioned in Section 3.3. The three pairs of foci of the triaxial ellipsoid  $\varepsilon_0$  (circumscribing ellipsoid for an irregular body) are denoted as  $(\pm E_x, 0, 0)$ ,  $(\pm E_e, 0, 0)$ ,  $(\pm E_y, 0, 0)$  and can be seen in Figure 3.3, Figure 3.4, and Figure 3.5. In the same figures, the reader can also notice the semi-major axes  $a, b, c$  of  $\varepsilon_0$ . These figures are a much simplified diagram (and also not to scale), depicting the ellipsoid and its parameters, compared to the ones rendered in [43] (see section 2 of [43]).

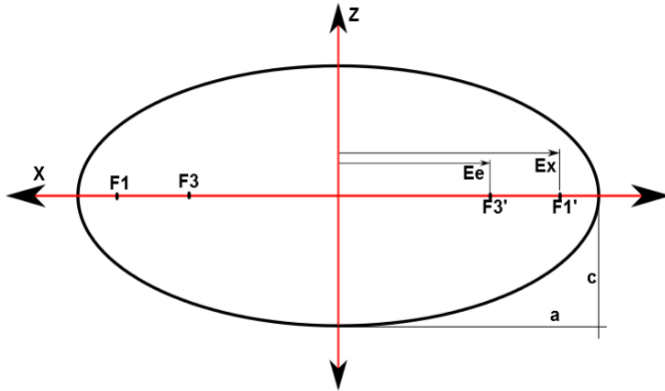


**Figure 3.3:**  $X - Z$  plane of triaxial ellipsoid.

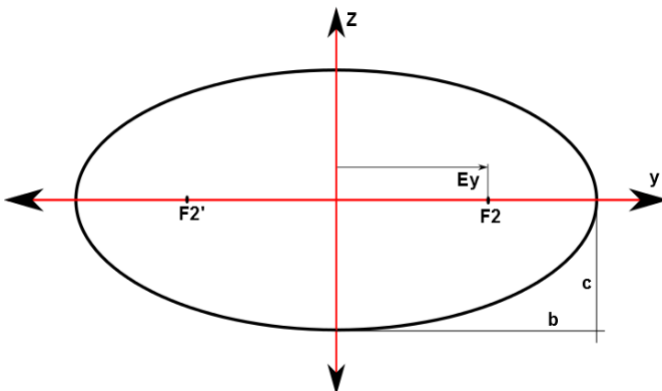


**Figure 3.4:**  $Y - Z$  plane of triaxial ellipsoid.

The focal lengths are given as  $E_x = \sqrt{a^2 - c^2}$ ,  $E_y = \sqrt{b^2 - c^2}$ , and  $E_e = \sqrt{a^2 - b^2}$ . The parameter  $E_e$  can be related to  $E_x$  and  $E_y$  as  $E_e^2 = E_x^2 - E_y^2$  [43]. The general relation between the ellipsoidal coordinates  $(s_1, s_2, s_3)$  and the cartesian coordinates  $(x, y, z)$  is given as [43]:

$$x^2 = \frac{(a^2 + s_1)(a^2 + s_2)(a^2 + s_3)}{(a^2 - b^2)(a^2 - c^2)} \quad (3.43)$$

$$y^2 = \frac{(b^2 + s_1)(b^2 + s_2)(b^2 + s_3)}{(b^2 - a^2)(b^2 - c^2)} \quad (3.44)$$

$$z^2 = \frac{(c^2 + s_1)(c^2 + s_2)(c^2 + s_3)}{(c^2 - a^2)(c^2 - b^2)} \quad (3.45)$$

The transformation given in Equation (3.43), Equation (3.44), and Equation (3.45) is not one-to-one and for each ellipsoidal coordinate  $(s_1, s_2, s_3)$  there exists eight cartesian points  $(\pm x, \pm y, \pm z)$ . [43] has introduced an alternate variant of ellipsoidal coordinates so as to have a one to one relation with the cartesian coordinates. These new ellipsoidal coordinates will be denoted as  $(u, \beta, \lambda)$  and are given

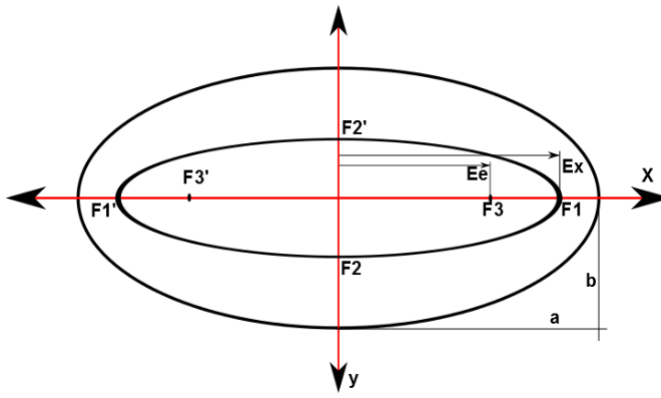


Figure 3.5:  $X - Y$  plane of triaxial ellipsoid.

by the following relations:

$$s_1 = u^2 - c^2 \quad (3.46)$$

$$s_2 = -b^2 \sin^2(\beta) - c^2 \cos^2(\beta) \quad (3.47)$$

$$s_3 = -a^2 \sin^2(\lambda) - b^2 \cos^2(\lambda) \quad (3.48)$$

In the new ellipsoidal coordinates  $(u, \beta, \lambda)$ ,  $u$  is the polar semi-axis of the ellipsoid,  $\beta$  is the ellipsoidal latitude and  $\lambda$  is the ellipsoidal longitude [43]. Upon substituting Equation (3.46), Equation (3.47), and Equation (3.48) into Equation (3.43), Equation (3.44), and Equation (3.45), the following relations are obtained [43]:

$$x = \sqrt{u^2 + E_x^2} \left[ \cos^2 \beta + \frac{E_e^2}{E_x^2} \sin^2 \beta \right]^{1/2} \cos \lambda \quad (3.49)$$

$$y = \sqrt{u^2 + E_y^2} \cos \beta \sin \lambda \quad (3.50)$$

$$z = u \sin \beta \left[ 1 - \frac{E_e^2}{E_x^2} \cos^2 \lambda \right]^{1/2} \quad (3.51)$$

where  $u \geq 0$ ,  $-\pi/2 \leq \beta \leq \pi/2$ , and  $-\pi < \lambda \leq \pi$ . Equation (3.49) to Equation (3.51) show a one to one correspondence between the cartesian coordinates and the alternate variant of ellipsoidal coordinates. Now that we have developed an understanding for the ellipsoidal coordinates, we shall discuss the expression for the gravitational potential of a triaxial ellipsoid given in terms of an elliptic integral.

The gravitational potential  $U$  of a homogeneous ellipsoid can be expressed in terms of an integral as follows [43]:

$$U(s_1, s_2, s_3) = \frac{3}{4} \mu \int_{s_1}^{\infty} \left[ 1 - \frac{x^2}{a^2 + s} - \frac{y^2}{b^2 + s} - \frac{z^2}{c^2 + s} \right] \frac{ds}{\sqrt{(a^2 + s)(b^2 + s)(c^2 + s)}} \quad (3.52)$$

where  $(s_1, s_2, s_3)$  are the ellipsoidal coordinates which are related to the Cartesian coordinates by Equation (3.43), Equation (3.44) and Equation (3.45). In terms of the alternate variant of ellipsoidal coordinates,  $(u, \beta, \lambda)$ , the gravitational potential is expressed as [43]:

$$U(u, \beta, \lambda) = \frac{3}{2} \mu \int_u^{\infty} \left[ 1 - \frac{x^2}{\sigma^2 + E_x^2} - \frac{y^2}{\sigma^2 + E_y^2} - \frac{z^2}{\sigma^2} \right] \frac{d\sigma}{\sqrt{(\sigma^2 + E_x^2)(\sigma^2 + E_y^2)}} \quad (3.53)$$

The expression in Equation (3.53) can further be broken down into four "basic" integrals [43]:

$$U(u, \beta, \lambda) = \frac{3}{2} \mu (I_0(u) - x^2 I_1(u) - y^2 I_2(u) - z^2 I_3(u)) \quad (3.54)$$

where

$$I_0(u) = \int_u^\infty \frac{d\sigma}{\sqrt{(\sigma^2 + E_x^2)(\sigma^2 + E_y^2)}} \quad (3.55)$$

$$I_1(u) = \int_u^\infty \frac{d\sigma}{\sqrt{(\sigma^2 + E_x^2)^3(\sigma^2 + E_y^2)}} \quad (3.56)$$

$$I_2(u) = \int_u^\infty \frac{d\sigma}{\sqrt{(\sigma^2 + E_x^2)(\sigma^2 + E_y^2)^3}} \quad (3.57)$$

$$I_3(u) = \int_u^\infty \frac{d\sigma}{\sigma^2 \sqrt{(\sigma^2 + E_x^2)(\sigma^2 + E_y^2)}} \quad (3.58)$$

Equation (3.54), at first look, does not seem to have any dependency on the ellipsoidal coordinates  $u, \beta, \lambda$  but the dependence becomes apparent when the  $x, y, z$  coordinates are substituted from Equation (3.49) to Equation (3.51) into Equation (3.54). The integrals  $I_0, I_1, I_2$ , and  $I_3$  can be expressed as elliptic integrals of the first and the second kind in order to be evaluated. However these integrals can also be computed using numerical integration methods. In order to use the numerical method, these improper integrals (since they are definite integral with one of the boundaries being  $\infty$ ) have to be converted into proper definite integrals by applying the transformation  $\sigma = 1/t$  (note that the lower and upper boundaries of the new integrals change because of applying the transformation). The transformed integrals are shown below [43]:

$$I_0(u) = \int_0^{1/u} \frac{dt}{\sqrt{(1 + E_x^2 t^2)(1 + E_y^2 t^2)}} \quad (3.59)$$

$$I_0(u) = \int_0^{1/u} \frac{t^2 dt}{\sqrt{(1 + E_x^2 t^2)^3(1 + E_y^2 t^2)}} \quad (3.60)$$

$$I_0(u) = \int_0^{1/u} \frac{t^2 dt}{\sqrt{(1 + E_x^2 t^2)(1 + E_y^2 t^2)^3}} \quad (3.61)$$

$$I_0(u) = \int_0^{1/u} \frac{t^2 dt}{\sqrt{(1 + E_x^2 t^2)(1 + E_y^2 t^2)}} \quad (3.62)$$

Thus using any numerical integration method, Equation (3.59) to Equation (3.62) can be computed which can then be utilized in Equation (3.54) to compute the gravitational potential at any given point  $x, y, z$  external to the ellipsoid.

### 3.5 MASS CONCENTRATION MODEL

To calculate the trajectory of a particle around a single or a system of small irregularly shaped bodies, the mass concentrations or "*mascon*" model can also be used. In this method, the entire volume of the small irregular body can be filled with a uniform grid of point masses such that the sum of all these point masses equals the total mass of the body. The acceleration for a particle or spacecraft in orbit around such a small irregular body is then calculated as a vector sum of accelerations due to each point mass. The position and velocity of the particle in orbit and that of the rotating small

irregular body are then updated in each time step [17].

Consider  $m_i$  being one of the point masses in the distribution where  $i = 1, \dots, n$  and  $n$  is the total number of point masses;  $U_i$  being the gravitational potential due to the point mass  $i$ ;  $\mathbf{r}_i$  being the Cartesian position vector of the orbiting particle from the point mass  $i$  in the inertial reference frame;  $\mathbf{a}_i$  being the acceleration due to the point mass  $i$ ; then the following relations can be written:

$$U_i = \frac{Gm_i}{r_i} \quad (3.63)$$

$$\vec{a}_i = \frac{\delta}{\delta x}(U_i)\hat{x} + \frac{\delta}{\delta y}(U_i)\hat{y} + \frac{\delta}{\delta z}(U_i)\hat{z} \quad (3.64)$$

The total acceleration will then be given as:

$$\overrightarrow{a}_{tot} = \sum_{i=1}^n \vec{a}_i \quad (3.65)$$

### 3.6 POLYHEDRON MODEL

A polyhedron is a three-dimensional solid body whose surface consists of several planar faces (or facets) that meet along straight edges or at isolated points called vertices. An edge can be common to only two faces. These planar faces are, in general, polygons. Three or more of these planar faces meet at each vertex. The reader should note that just the vertex coordinates alone are not sufficient enough to completely describe a polyhedron. In addition to the vertex coordinates, information about which edge connects which vertex pair and bounds which face pair should also be given to completely characterize a polyhedron. To adopt the polyhedron modeling of gravitational attraction, two important assumptions are made [61]:

- The asteroid is a polyhedron
- The asteroid's density is constant

Each polyhedron face has a normal vector  $\hat{n}_f$ , which is pointing outwards, and a face dyad  $F_f = \hat{n}_f \hat{n}_f$ . The latter is basically a dyadic product of the normal vector with itself. Now each edge of each face also has its own normal vector denoted as  $\hat{n}_e^f$  which is perpendicular to  $\hat{n}_f$  and also to the edge to which it belongs. This edge normal vector lies in the plane of the corresponding face [61]. Figure 3.6 gives a graphical view of the different vectors just described. For the common edge  $P_1P_2$  connecting faces A and B (see Figure 3.6) the edge dyad is defined as  $E_{12} = \hat{n}_A \hat{n}_{12}^A + \hat{n}_B \hat{n}_{21}^B$  i.e. the summation of two dyadic products. Other edge dyads,  $E_e$ , are defined in a similar way [61].

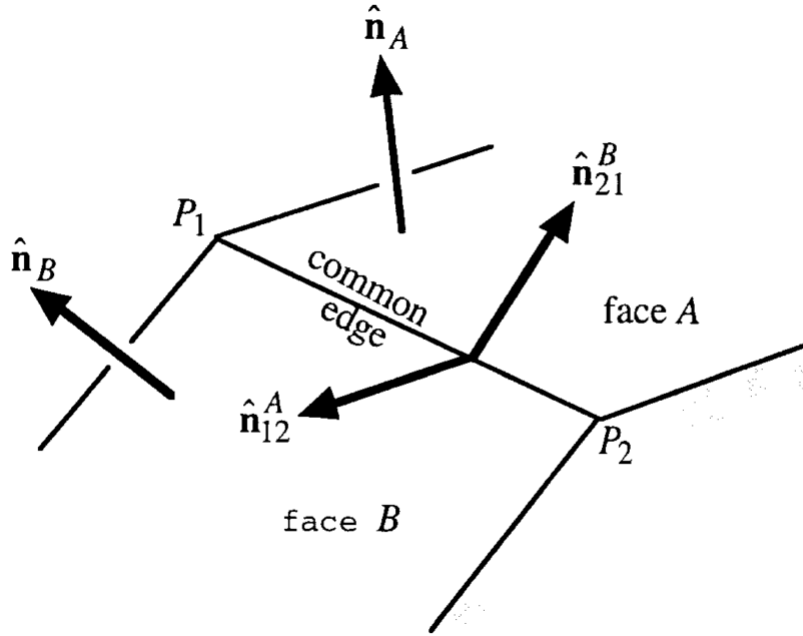


**Figure 3.6:** Two adjacent faces of the polyhedron depicting the common edge  $P_1P_2$ .  $\hat{n}_A$  and  $\hat{n}_B$  are the two face normal vectors;  $\hat{n}_{12}^A$  and  $\hat{n}_{21}^B$  are the edge normal vectors situated in planes A and B respectively [61].

Consider one edge of a face on the polyhedron. Let this edge have two vertex points denoted as  $P_i$  and  $P_j$ . Let the length of the edge be denoted as  $e_{ij}$ . Consider a point external to the polyhedron, henceforth called as the field point i.e. the point at where the potential is to be calculated. Let the distance vectors from this field point to the vertices  $P_i$  and  $P_j$  be denoted as  $\vec{r}_i$  and  $\vec{r}_j$  respectively. Then the dimensionless per-edge factor  $L_e$  is denoted as [61]:

$$L_e = \ln \frac{\|\vec{r}_i\| + \|\vec{r}_j\| + e_{ij}}{\|\vec{r}_i\| + \|\vec{r}_j\| - e_{ij}} \quad (3.66)$$

Now consider that each face of the polyhedron is triangular, bounded by vertices  $P_i$ ,  $P_j$ , and  $P_k$ . Each of these vertices has a position vector defined from a field point external to the polyhedron as  $\vec{r}_i$ ,  $\vec{r}_j$ , and  $\vec{r}_k$  respectively. Then the dimensionless per-face factor  $w_f$  is denoted as [61]:

$$w_f = 2 \arctan \frac{\vec{r}_i \cdot \vec{r}_j \times \vec{r}_k}{\|\vec{r}_i\| \cdot \|\vec{r}_j\| \cdot \|\vec{r}_k\| + \|\vec{r}_i\|(\vec{r}_j \cdot \vec{r}_k) + \|\vec{r}_j\|(\vec{r}_k \cdot \vec{r}_i) + \|\vec{r}_k\|(\vec{r}_i \cdot \vec{r}_j)} \quad (3.67)$$

Using the above definitions, the gravitational potential of a polyhedron at a variable field point can be defined as [61]:

$$U = \frac{1}{2} G\sigma \sum_{e \in \text{edges}} \vec{r}_e \cdot E_e \cdot \vec{r}_e \cdot L_e - \frac{1}{2} G\sigma \sum_{f \in \text{faces}} \vec{r}_f \cdot F_f \cdot \vec{r}_f \cdot w_f \quad (3.68)$$

The vector  $\vec{r}_e$  is a position vector from the field point to any point on the edge  $e$ , similarly the vector  $\vec{r}_f$  is the position vector from the field point to any point in the face  $f$ ,  $G$  is the universal gravitational constant, and  $\sigma$  is the (constant) density of the polyhedron. Thus with the definitions given above, the gravitational potential at any external field point can be easily calculated. An example polyhedron model for the primary asteroid in the binary system 1999 KW4 is shown in Figure 3.7 [58].

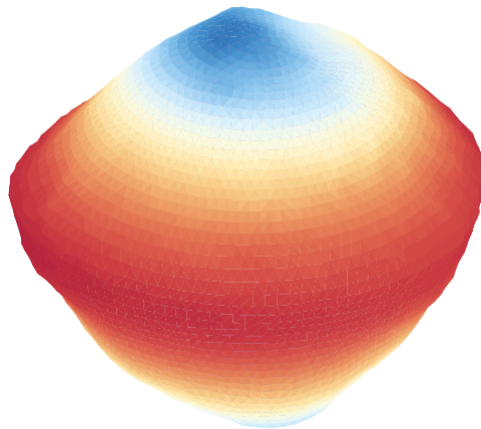


**Figure 3.7:** polyhedron model of the primary asteroid in binary system 1999 KW4. Red faces indicate higher potential, blue indicate low potential [58].

### 3.7 CONCLUSION

This chapter discussed various methods in which the gravitational potential of a small irregular body (or in general any celestial body) can be modeled. This section will present a subjective discussion (based on certain criteria) on the advantages and/or disadvantages of using any particular model. We will also look into the results from an objective comparison performed between the ellipsoidal harmonics model and the spherical harmonics model, where the polyhedron model was used as the reference. The objective results were taken from a previous study in [23].

The criteria which shall be responsible for deciding the relevance of a given potential model are as follows:

- Computational economy
- Volume of divergence
- Accuracy
- Availability of physical data on asteroids
- Application

The classical approach for modeling the gravitational field for an arbitrary body is in the form of a spherical harmonics expansion. This method involves relatively simple mathematics and converges to an accurate value of the gravity field outside the circumscribing sphere (see Figure 3.10). Finite truncation orders can model the potential of the body to have a close match with the "true" potential. To improve the accuracy of the model, for a given body, the spherical harmonic coefficients can be determined with a high accuracy by evaluating the perturbations acting on the orbiting space-craft. The disadvantage, however, is that the spherical harmonic expansion model exhibits severe divergence within the circumscribing sphere [7]. The gravitational acceleration using the spherical harmonics model was calculated for the asteroid 433 Eros in [23]. The acceleration due to gravity was calculated on a reference circumscribing sphere using the polyhedron model and then again by using the spherical harmonics model. The difference between the two were then calculated to judge the accuracy of the spherical harmonics model for a highly elongated and irregular shape of Eros (the study considered the gravitational acceleration computed using the polyhedron model as the "true" acceleration). The results for the differences in computed gravitational acceleration between the spherical harmonics (degree 10 and 20) and the polyhedron model are shown in Figure 3.8

and Figure 3.9 respectively [23]. The errors reduce when the degree of the spherical harmonic expansion is increased, indicating that higher orders can provide a very good approximation of the "true" gravity field.

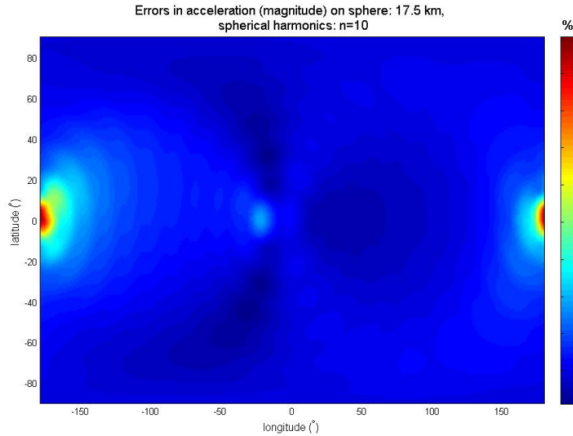


**Figure 3.8:** Difference in the computed gravitational acceleration between the spherical harmonics model of degree 10 and the polyhedron model [23].

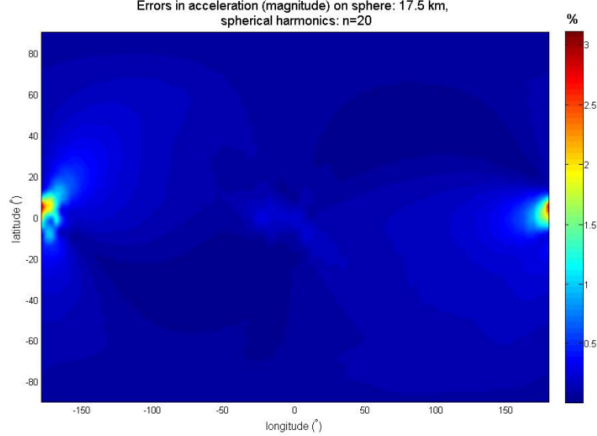


**Figure 3.9:** Difference in the computed gravitational acceleration between the spherical harmonics model of degree 20 and the polyhedron model [23].

As explained in Section 3.2, that majority of the perturbations from the non-uniform gravitational field of an irregular body can be accounted for by just taking the second degree and order coefficients, however, determining the values for these coefficients can itself be a problem if no spacecraft tracking data around an asteroid is available (from which the values of the coefficients can be determined) or if the principle moments of inertia of the asteroid are unknown. It is easy to infer that if the values for the gravitational coefficients are unknown then the spherical harmonics model can not be used.

For close proximity operations, the spherical harmonics model can not be used to model the gravity of an asteroid since the spherical harmonics expansion diverges inside the circumscribing sphere. In general, the spherical harmonics model is not suitable for aspherical bodies [49] since the circumscribing sphere does not provide an optimal fit to such a body leading to large volumes of space around the body where the expansion diverges severely. The circumscribing sphere can be seen in Figure 3.10. Thus, although we can increase the accuracy of the gravitational potential modeling by increasing the degree and order of the harmonics expansion, it still can not avoid the divergence of the expansion inside the circumscribing sphere. For applications involving the study of motion on or very close to the surface of an asteroid, such as the orbital motion of lofted regolith, the spherical harmonics model can not be used.

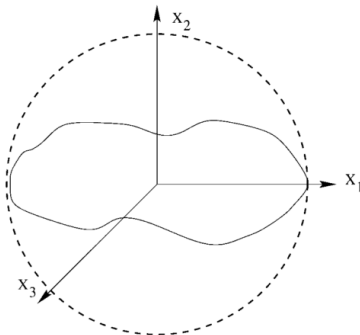


**Figure 3.10:** Circumscribing sphere (or the Brillouin sphere) [49].

We shall now evaluate the feasibility of using the ellipsoidal harmonics expansion. The difference in the computed gravitational acceleration, for 433 Eros, between the ellipsoidal harmonics model, of degrees 10 and 20, and the polyhedron model is shown in Figure 3.11 and Figure 3.12. The accelerations were calculated on the reference ellipsoid that circumscribed Eros [23]. Note that the peak value for the difference in the degree 10 expansion case is more than that of the corresponding spherical harmonics case. The order of magnitude for the difference in the gravitational accelerations for the degree 20 expansion of the ellipsoidal harmonics is, however, the same as that for the corresponding spherical harmonics expansion. Just like in the case of the spherical harmonics, by increasing the degree of the ellipsoidal harmonics expansion, the accuracy of the modeled gravitational field has increased. For irregular and elongated bodies such as Eros, [23] mentions that the spherical harmonics expansion is less suitable than the ellipsoidal harmonics expansion.

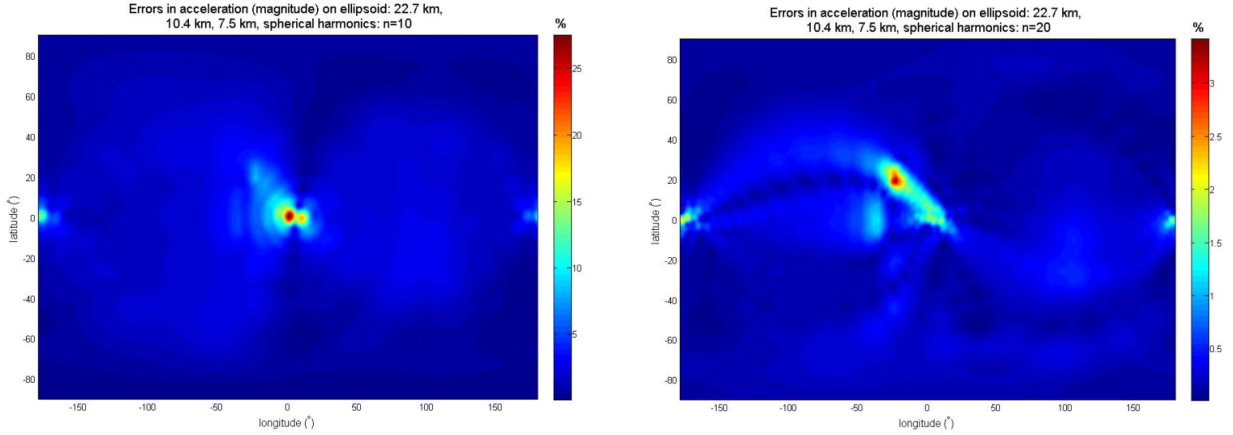


**Figure 3.11:** Difference in the computed gravitational acceleration between the ellipsoidal harmonics model of degree 10 and the polyhedron model [23].

**Figure 3.12:** Difference in the computed gravitational acceleration between the ellipsoidal harmonics model of degree 20 and the polyhedron model [23].

Just like in the case of the spherical harmonics expansion, the ellipsoidal harmonic expansion is convergent outside the circumscribing ellipsoid or the Brillouin ellipsoid. For an irregular body, an ellipsoid fits more closely rather than a sphere (see Figure 3.14), and thus the volume of divergence of the ellipsoidal harmonic expansion is reduced. This provides an opportunity to work with orbits around an asteroid at close proximity. Again due to the fact that an ellipsoid can fit an irregular body more closely than a sphere, the potential calculated at a point close to the body is much accurate in the case of ellipsoidal harmonic expansion rather than the spherical harmonic expansion [49]. Within their respective volumes of divergence, the ellipsoidal harmonics model performs better than its spherical counterpart [23]. This is evident from Figure 3.13. It illustrates the difference in the computed gravitational potential for Phobos between the polyhedron model and the two harmonic (spherical and ellipsoidal) expansion models [23]. The performance of the ellipsoidal harmonics model is much better than that of the spherical harmonics, within their respective volume of divergence. Note that the points at which the potential was calculated in both cases, was the same [23].

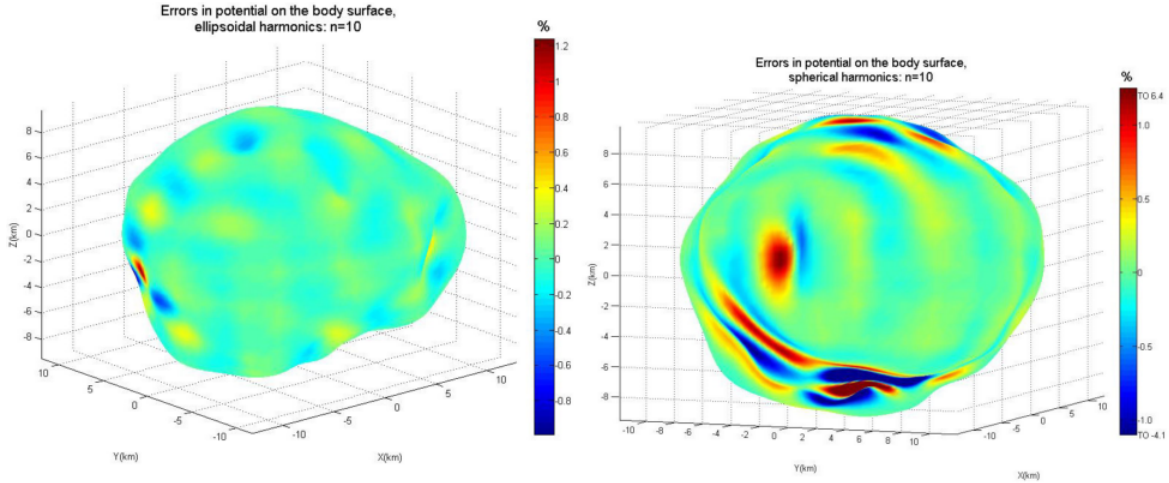


**Figure 3.13:** Difference in the computed gravitational potential for Phobos between the polyhedron model and the two harmonic, ellipsoidal (shown on the left) and spherical (shown on the right), expansion models [23].

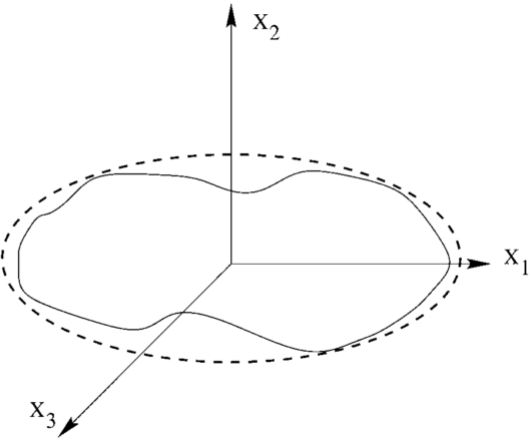


**Figure 3.14:** Circumscribing or Brillouin ellipsoid [49].

In general, for both spherical and ellipsoidal harmonics, a common drawback is that these models do not provide information on whether a field point (the point at which the gravitational potential is to be calculated) is inside or outside the body [61], an information which is very useful when designing orbits very close to the surface of an asteroid.

After the harmonic models, we shall now discuss the elliptic integral potential model wherein the body is assumed to be a perfect ellipsoid of constant density. The variant of ellipsoidal coordinates used in this model ensures that its transformation to Cartesian coordinate is one-to-one without imposing any extra rules or constraints. The integrals involved in the potential formula can be expressed as elliptic integrals of the first and the second kind in order to be evaluated. However the model presented in Section 3.4 has provided an alternate representation for these integrals allowing their evaluation by just using any numerical integration algorithm. This makes the computation of the elliptic integral potential model much easier than the harmonic expansion models. Unlike the harmonic expansion models, the elliptic integral model is not truncated at a certain degree or order and therefore the latter is more accurate than the former.

The mass concentrations or "mascons" model is easy to develop but is computationally intensive since at each time step the acceleration due to individual point masses has to be calculated.

Although the model can be used to approximate the shape and density of a given asteroid to a great accuracy but for a given computational effort, the mascons approach is less accurate than the harmonics approach in its given region of convergence [61].

The final approach that we used to model the gravity field for an asteroid is by using a constant density polyhedron. Small details such as craters, elevations, slopes and other surface features can be included in modeling the asteroid with very high resolution. The biggest advantage of polyhedron modeling is that the potential is valid and exact for any given shape up to the surface of that body. Thus there are no regions of divergence, unlike that in the case of harmonic models, which means that close proximity orbits can be designed using the polyhedron potential. Errors in polyhedron potential modeling can arise because of errors in shape determination of an asteroid, the resolution selected for modeling i.e. the number of facets used to represent the polyhedron, and finally because of the assumption that the asteroid is of constant density [7]. Another drawback is that the computational effort required in this model is quite significant. Polyhedron models are generally helpful when considering the design of lander trajectories because it involves surface interaction and harmonic models will diverge if the potential is calculated at the surface of an irregular body. Also, polyhedron models restrict the orbit design strategy to be specific to the body being modeled and not to any arbitrary body.

After discussing all the pros and cons of the various potential models and for the application of studying the motion of lofted regolith from the surface of an asteroid, a study that will involve obtaining orbits close to the surface of the asteroid with a possibility for surface interaction, the polyhedron model will be the most suitable and hence it will be used for the thesis in future.

# 4

## ORBITAL PERTURBATIONS

### 4.1 INTRODUCTION

Within the context of exploring the dynamic behavior of a particle near a pair of small irregular bodies, it is necessary to explore the effects of different perturbing forces, acting on the particle, on initial baseline orbits (orbits without perturbations). Perturbations hold significant importance especially when considering particle motion around small irregular bodies since the gravitational attraction of these bodies is weak relative to that of planets and thus even the smallest of the perturbing forces can result in drastic changes to baseline orbit designs. In this chapter we shall explore the perturbing forces of consequence in the context of a particle in motion around binary irregular asteroids.

### 4.2 SOLAR RADIATION PRESSURE

We begin with a simple model for the SRP (Solar Radiation Pressure) perturbation. The geometry involving the modeling of this perturbation is shown in Figure 4.1.

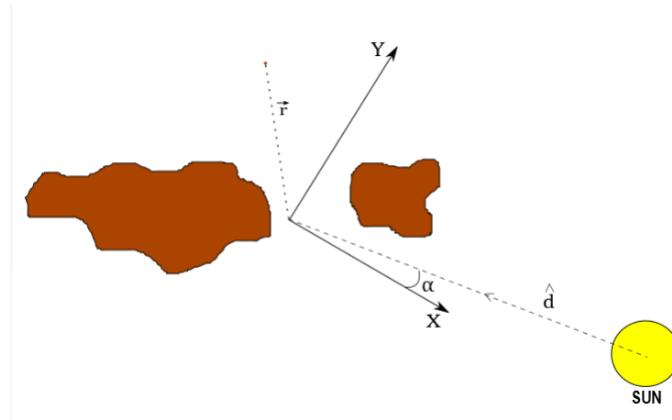


**Figure 4.1:** Geometry used in modeling SRP perturbation. Diagram not to scale.

The relative sizes and positions of the celestial bodies as depicted in Figure 4.1 are not to scale and are shown therein for the purpose of representation only. The coordinate axis system as shown in the figure is an inertial frame with the origin attached to the barycentre of the binary asteroid system. The hidden axis,  $Z$ , completes the coordinate frame in the right hand sense and hence the axis is coming out of the plane of the figure. The unit vector,  $\hat{d}$ , points away from the sun and represents the inverse of the direction of the sun relative to the binary asteroid system. The angle  $\alpha$  represents

the longitude of the Sun with respect to the binary asteroid system. Note that the barycentre of the binary system is considered as the centre of the dynamical system shown in Figure 4.1 and that the Sun is in a planar orbital motion around the centre. For simplicity, The motion of the Sun around the binary system is computed by solving the classical two-body point mass problem, the primary being the barycentre of the binary asteroid system and the secondary being the Sun. As we will see later, changing longitude of the Sun affects the direction in which the SRP acceleration will be acting on a particle in orbit around the asteroids. Since only a planar system is considered here, the SRP acceleration acting on an orbiting particle in the inertial  $Z$  direction is null. The vector  $\vec{r}$  depicts the inertial position of a particle in orbit around the asteroid system; note that this particle is in a proper three dimensional motion around the two asteroids. Another aspect to be noticed here is that the distance from the Sun to any particle in orbit around the binary asteroid system, is assumed to be the same as the distance between the Sun and the barycentre of the binary asteroids. This simplification was made because the distance to the Sun is extremely large compared to the distance between the orbiting particle and the barycentre and hence the position from the latter and the former to the Sun can be considered to be effectively equal.

The perturbing potential because of SRP is given as [50]:

$$R_{SRP} = g_{SRP} \hat{d} \cdot \vec{r} \quad (4.1)$$

where  $g_{SRP}$  is the magnitude of the acceleration. Partial derivative of the perturbing potential  $R_{SRP}$  with respect to the position vector  $\vec{r}$  gives the perturbing acceleration vector as follows [50]:

$$\vec{g}_{SRP} = g_{SRP} \hat{d} \quad (4.2)$$

where the magnitude of the acceleration is computed as follows [50]:

$$g_{SRP} = \frac{\beta}{d^2} \quad (4.3)$$

where  $d$  is the magnitude of the distance between the centre of the Sun and the binary asteroid barycentre; the term  $\beta$  is defined as follows [50]:

$$\beta = \frac{(1 + \rho)G_1}{B} \quad (4.4)$$

where  $B$  is the particle mass-to-area ratio in  $\frac{kg}{m^2}$ ,  $\rho$  is the reflectivity of the particle, and  $G_1$  is the Solar constant and has a value of approximately  $1 \times 10^8 \frac{kg \cdot km^3}{s^2 \cdot m^2}$  [50]. The unit vector  $\hat{d}$  is given as:

$$\hat{d} = \begin{bmatrix} -\cos(\alpha) \\ -\sin(\alpha) \\ 0 \end{bmatrix} \quad (4.5)$$

From Equation (4.2) and Equation (4.3), one can see that the magnitude of the perturbing acceleration depends on the distance to the Sun which varies all the time as the Sun traverses in an planar elliptic orbit around the binary asteroid system, and one can also infer that the direction of the perturbing acceleration changes with the longitude of the Sun with respect to the binary system. Note that the SRP model presented here is very simple and is meant for discussions on bulk and qualitative effects of the perturbation. A detailed model will include the orientation of the asteroid's surface, its temperature and a few other parameters [53].

For natural particles, such as the regolith on the surface of an asteroid, the reflectance  $\rho$  of the particle is  $<< 1$  and hence, it can be assumed to be 0 [53]. The particle is assumed to have a spherical shape with mass  $M$  defined as  $M = \frac{4\pi\sigma r_0^3}{3}$  and total projected area  $\pi r_0^2$ , where  $\sigma$  is the particle's

density and  $r_0$  is the particle radius [53]. Thus for a spherical regolith particle the mass-to-area ratio  $B$  is calculated as [53]:

$$B = \frac{4\sigma r_0}{3} \quad (4.6)$$

As an example to understand the qualitative effect of SRP, consider the regolith grain density of  $2.5 \frac{g}{cm^3}$  and particle grain radius of 0.2 micron for the asteroid Eros, which is at a distance of 1.13 AU [53]. The magnitude of SRP acceleration is then equal to  $8.94 \times 10^{-3} m/s^2$ . For Eros, with the gravitational parameter  $\mu = 4.5 \times 10^{-4} km^3/s^2$  and mean radius  $R = 8.4 km$  [53], the gravitational acceleration (assuming Eros to be a point-mass) is then equal to  $6.38 \times 10^{-3} m/s^2$ . It can be seen that for the given particle density and grain radius, the perturbing acceleration due to SRP is of the same order of magnitude as the gravitational attraction of the asteroid, and hence SRP can not be ignored whilst studying orbital motion of regolith around an asteroid.

### 4.3 THIRD BODY PERTURBATION

The presence of other celestial bodies, such as the Sun and Jupiter, will provide a perturbing force that will affect the motion of a particle in its orbit around the binary asteroid system. Let's denote the body or particle being perturbed with the index  $i$ , the perturbing bodies by index  $j$ , and the barycentre of the binary asteroid by the index  $k$  which is also where the inertial reference frame is centered at. Then the perturbing potential as defined in this inertial reference frame is expressed by the following equation [60]:

$$R_{celt} = -G \sum_{j \neq i, k} m_j \left[ \frac{1}{r_{ij}} - \frac{\vec{r}_i \cdot \vec{r}_j}{r_j^3} \right] \quad (4.7)$$

where  $G$  is the universal gravitational constant;  $m_j$  is the mass of the  $j^{th}$  perturbing body;  $r_{ij}$  is the distance between the bodies  $i$  and  $j$ ;  $\vec{r}_i$  and  $\vec{r}_j$  are the position vectors of the body  $i$  and  $j$  from the inertial reference frame as defined before;  $r_j$  is the magnitude of the vector  $\vec{r}_j$ . A low-fidelity perturbing potential model will be considered, in the sense that the perturbing celestial bodies will be considered as point masses and that they are in planar elliptic motion around the binary asteroid system. The two celestial bodies which shall have considerable influence on the motion of a particle orbiting the asteroids, will be Jupiter and the Sun. The perturbing acceleration is defined as [60]:

$$\mathbf{g}_{celt} = -\vec{\nabla} \left[ -Gm_j \left( \frac{1}{r_{ij}} - \frac{x_i x_j + y_i y_j}{r_j^3} \right) \right] \quad (4.8)$$

The individual components of this perturbing acceleration, from Equation (4.8), can be given as [60]:

$$g_{celt-x} = Gm_j \left( \frac{x_j - x_i}{r_{ij}^3} - \frac{x_j}{r_j^3} \right) \quad (4.9)$$

$$g_{celt-y} = Gm_j \left( \frac{y_j - y_i}{r_{ij}^3} - \frac{y_j}{r_j^3} \right) \quad (4.10)$$

$$g_{celt-z} = 0 \quad (4.11)$$

To understand the qualitative effect of the gravitational attraction from a third body, we shall compute the gravitational acceleration from the Sun and Jupiter and compare it with the gravitational acceleration of the asteroid Eros. Since we want to look only at the qualitative effect, the distance between the perturbing third-bodies and the regolith particle will be assumed to be the same as the distance between the former and the asteroid Eros. This assumption is valid since the

distance between an orbiting regolith particle and the asteroid will be relatively small compared to the distance between the perturbing third-bodies and the asteroid. The gravitational parameter of the sun is  $1.327 \times 10^{20} \text{ m/s}^2$  [27] and the distance to the asteroid from the sun is 1.13 AU [53] (Eros' perihelion distance [28]). Thus, the acceleration due to the Sun's gravitational pull (assuming point-mass attraction) is then equal to  $4.64 \times 10^{-3} \text{ m/s}^2$ . The gravitational parameter for the Jupiter is  $1.267 \times 10^{17} \text{ m}^3/\text{s}^2$  [40]. Since we considered perihelion distance for Eros, we shall consider the perihelion distance for Jupiter (assuming a configuration where the Sun, Eros and Jupiter are in a straight line and in that order), which is 4.95 AU [40]. Then the distance between Eros and Jupiter is 3.82 AU. Thus, the acceleration due to Jupiter's gravitational pull (assuming point-mass attraction) is then equal to  $3.879 \times 10^{-7} \text{ m/s}^2$ . In Section 4.2, we calculated the gravitational attraction of Eros, which came out to be  $6.38 \times 10^{-3} \text{ m/s}^2$ . Thus, the magnitude of perturbing acceleration from the Sun is of the same order of magnitude as the asteroid's gravitational acceleration. The magnitude of perturbing acceleration from the Jupiter, however, has an order four times less than the asteroid's gravitational acceleration and the Sun's perturbing acceleration.

#### 4.4 LAGRANGE PLANETARY EQUATIONS

When dealing with perturbed orbits, the classical orbital elements are no longer the constants of motion. In such a scenario, the orbital motion of a particle can be considered as a seamless transition from one set of orbital elements to another [60]. For a given instant of time, if the corresponding Cartesian coordinates are converted to orbital elements, then for that instant of time, we speak of osculating elements [60]. A set of first-order differential equations for the variation of the osculating elements with time, are termed as LPE (Lagrange Planetary Equations) [60]. For the motion of an orbiting particle, the effect of the perturbations is accounted for by entering them as a potential term, in addition to the gravitational potential, in the LPE. By integrating the differential equations, the values for the osculating elements can be obtained for any instant of time [60]. Thus, the variations in the osculating elements for a given integration time can provide valuable insight into how an orbit is being affected by the perturbing forces. The standard set of LPE are given as follows [51]:

$$\frac{da}{dt} = \frac{2}{na} \frac{\partial R}{\partial \chi} \quad (4.12)$$

$$\frac{de}{dt} = \frac{1-e^2}{na^2 e} \frac{\partial R}{\partial \chi} - \frac{\sqrt{1-e^2}}{na^2 e} \frac{\partial R}{\partial \omega} \quad (4.13)$$

$$\frac{di}{dt} = \frac{\cot i}{na^2 \sqrt{1-e^2}} \frac{\partial R}{\partial \omega} - \frac{1}{na^2 \sqrt{1-e^2} \sin i} \frac{\partial R}{\partial \Omega} \quad (4.14)$$

$$\frac{d\omega}{dt} = \frac{\sqrt{1-e^2}}{na^2 e} \frac{\partial R}{\partial e} - \frac{\cot i}{na^2 \sqrt{1-e^2}} \frac{\partial R}{\partial i} \quad (4.15)$$

$$\frac{d\Omega}{dt} = \frac{1}{na^2 \sqrt{1-e^2} \sin i} \frac{\partial R}{\partial i} \quad (4.16)$$

$$\frac{d\chi}{dt} = \frac{2}{na} \frac{\partial R}{\partial a} - \frac{1-e^2}{na^2 e} \frac{\partial R}{\partial e} \quad (4.17)$$

where  $a$  is the semi-major axis,  $e$  is the eccentricity,  $i$  is the inclination,  $\omega$  is the argument of periapsis,  $\Omega$  is the right ascension of the ascending node,  $n$  is the mean motion and  $\chi = -M_0$  where  $M_0$  is the mean anomaly [51].

#### 4.5 CONCLUSION

In this chapter, we covered the two most relevant sources of perturbation, i.e. SRP and third-body gravitational attraction, that can effect the orbital motion of a particle around an asteroid. The perturbing effect of an asteroid's irregular shape will also be accounted for, since we will be using

the polyhedron gravitational potential model (see Section 3.6). For SRP, we considered a low-fidelity perturbation model as a first step in analyzing its qualitative effect on baseline orbits of a particle.

We could have considered the method of LPE in this literature study to better visualize the effects of perturbations on the orbital motion of the particle because the variation of Keplerian orbital elements is much more intuitive rather than the variation of Cartesian position and velocity components. Since we will be dealing with the orbital motion of regolith lofted from the surface of an asteroid, the analysis of which demands that we consider different initial conditions for the lofted particles which can lead to any type of orbit, then in this situation and under certain circumstances the LPE method would lead to some singularities. For example, in case of orbits with very small inclination and/or eccentricity, the time derivatives of certain orbital elements would become infinitely large [60]. Since we will be analyzing the orbits of multiple particles, some of which may have an escape trajectory, some may fall back to the asteroid's surface and some may remain in an orbit around the asteroid, the singularity problem may be encountered in case of the motion of one of those particles. This issue of singularity can be avoided by adopting a different set of orbital elements, however, even then we will have to consider certain special cases such as that of near-circular orbit or near-equatorial orbit and all of this will again not help in applying the LPE method for a general analysis of particle orbital motion. Thus, for the aforementioned reasons, it was decided not to use LPE for perturbation analysis.

Another method in which we can observe the variations in the classical orbital elements is by converting the Cartesian position and velocity vector for each epoch in the ephemeris of the particle's orbit around an asteroid to its equivalent orbital elements. The recorded values of the orbital elements for each epoch can then be plotted to observe their variation over a certain period of time.

One of the initial assumption made in this literature study is that some of the lofted regolith particles may escape from the gravitational attraction of the asteroid. These particles could first complete certain fixed number of orbits around the asteroid before escaping or they may escape without even completing a single orbit around the asteroid. Since there is a possibility that the lofted regolith may escape without completing even a single orbit, we can not use the averaging techniques to analyze the secular effects of orbit perturbations. This conclusion is a corollary from an earlier work in [51] wherein averaging techniques were used to analyze the secular effects of perturbations for spacecraft orbits that complete a number of orbits around an asteroid and were assumed to not escape in general.

Finally, we shall now bring together the results from the qualitative analysis of the different perturbing accelerations and compare them. The perturbing accelerations of SRP and third-body gravitational attraction, along with the gravitational acceleration at the surface of an asteroid (assuming the asteroid is a point-mass), are given in Table 4.1. We can observe that the magnitudes of the

**Table 4.1:** Comparison of the magnitudes of perturbing acceleration due to SRP and third-body effect of the Sun and Jupiter with the magnitude of the acceleration due to gravity at the surface of asteroid Eros.

Source	Magnitude of acceleration [ $m/s^2$ ]
Solar Radiation Pressure	$8.94 \times 10^{-3}$
Third-body effect of the Sun	$4.64 \times 10^{-3}$
Third-body effect of the Jupiter	$3.88 \times 10^{-7}$
Acceleration due to gravity of Eros	$6.38 \times 10^{-3}$

perturbing accelerations due to SRP and the third-body effect of the Sun have the same order of magnitude as the acceleration due to gravity of Eros. Based on this qualitative analysis we should, in general, not ignore these two perturbing effects while analyzing the orbital motion of lofted regolith around an asteroid. The magnitude of perturbing acceleration due to the third-body effect of Jupiter has an order of magnitude which is 4 times smaller than the rest in Table 4.1, and as such

can be ignored. Thus, the SRP and the third-body effect of the Sun will be included as perturbing sources in the analysis of the orbital motion of lofted regolith around an asteroid.

# 5

## THE FULL 2-BODY PROBLEM

### 5.1 INTRODUCTION

This chapter presents the coupled rotational and orbital motion of a binary asteroid system wherein both the bodies are modeled as a polyhedron and are under the influence of their mutual gravitational potential. The dynamical equations presented here are applicable to any binary asteroid system with individual asteroids having any arbitrary shape and mass distribution. As mentioned in Chapter 1 that the initial goal of this literature study was to study the motion of a spacecraft around a binary asteroid system, which was inspired by a future mission called AIDA (see Section 2.2.2) wherein one of the spacecrafnts in the joint NASA ESA mission will be orbiting around the binary asteroid Didymos. This is the reason why in this chapter we present the theory to understand the dynamical system around a binary asteroid system.

But before we begin with discussing the motion for two polyhedrons, we will briefly look at (relatively) lower-fidelity binary asteroid models namely the sphere-ellipsoid and ellipsoid-ellipsoid systems.

#### 5.1.1 SPHERE-ELLIPSOID BINARY SYSTEM

In this full two-body problem formulation, the primary is modeled as an ellipsoid with semi-major axes  $\alpha$ ,  $\beta$ , and  $\gamma$  and the secondary is modeled as a sphere. Both bodies are uniform with constant densities. The geometry of the problem is given in Figure 5.1 [5]:

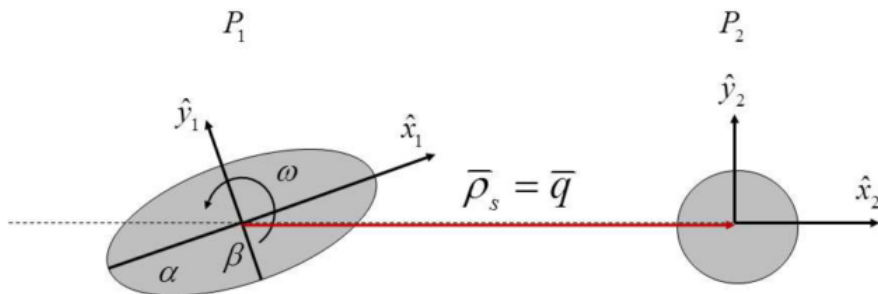


**Figure 5.1:** Geometry of sphere-ellipsoid binary system [5].

The non-dimensional equations of motion for this system, i.e. for the sphere around the ellip-

soid, are given as follows [5]:

$$\begin{aligned}\ddot{\rho}_s + 2\omega \times \dot{\rho}_s + \omega \times (\omega \times \rho_s) + \dot{\omega} \times \rho_s &= \frac{\partial U_{e1}}{\partial \rho_s} \\ I \cdot \dot{\omega} + \omega \times I \cdot \omega &= -\mu \rho_s \times \frac{\partial U_{e1}}{\partial \rho_s}\end{aligned}\quad (5.1)$$

These equations are defined in a rotating frame fixed to the ellipsoid. The term  $\rho_s$  is the non-dimensional position vector of the centre of mass of the sphere with respect to the ellipsoid as can be seen in Figure 5.1;  $\omega$  is the angular rate of the ellipsoid;  $I$  is the inertia dyadic for the ellipsoid;  $U_{e1}$  represents the gravitational potential of the ellipsoid [5].

### 5.1.2 ELLIPSOID-ELLIPSOID BINARY SYSTEM

In this form of full two-body problem, both the asteroids are modeled as triaxial ellipsoids. It is assumed that both bodies are orbiting each other in a coplanar and equatorial orbit. The dynamics of the mutual orbit is then described by four degrees of freedom; one distance and three angles. One of the angles,  $\theta$ , defines the only rotation existing between the inertial and rotating frame of reference about the  $z$ -axis. The two other angles define the rotation angle of the two ellipsoids about the inertial  $z$ -axis, namely  $\phi_1$  and  $\phi_2$ . The distance as a degree of freedom is basically the separation between the centres of the two ellipsoids. The geometry for this binary formulation is given in Figure 5.2 [5]. Note that the spacecraft is included in Figure 5.2 only as an illustration and serves no purpose in this chapter since the dynamics of the spacecraft around the binary system will not be modeled here. The figure was added unaltered since it was sourced from a published paper.

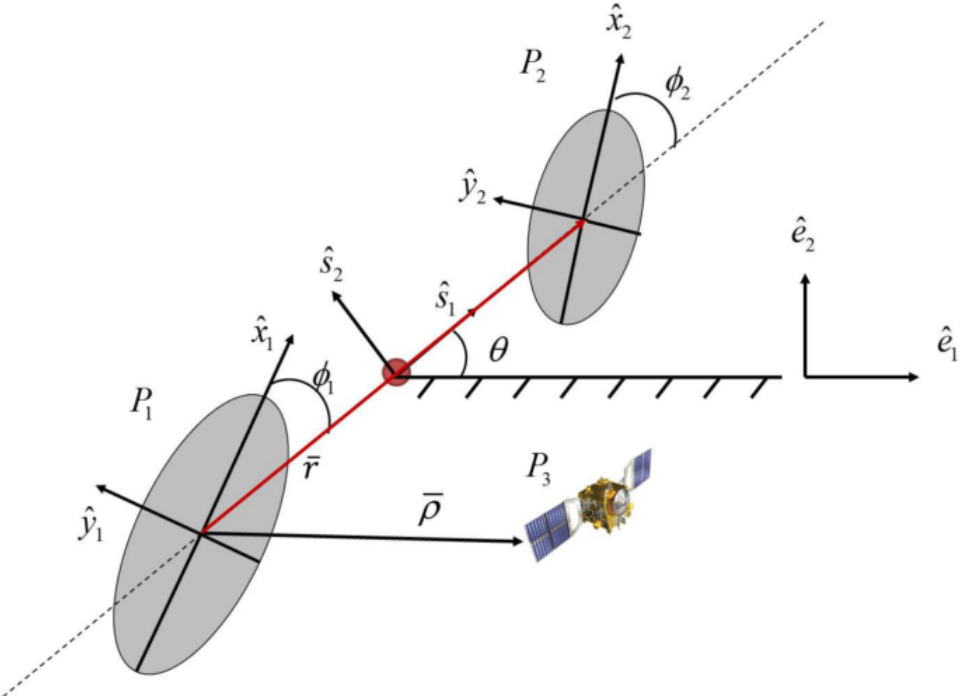


**Figure 5.2:** Geometry of ellipsoid-ellipsoid binary system [5]. Note that the spacecraft is included here only as an illustration and the dynamics of it around the binary system have not been included in the equations of motion since this chapter is concerned only with the two-body problem.

The equations of motion for the system are given as follows [5]:

$$\begin{aligned}\ddot{r} &= \dot{\theta}r - \frac{1}{m}V_r \\ \ddot{\phi}_1 &= -\left(1 + \frac{mr^2}{I_{1z}}\right)\frac{1}{mr^2}V_{\phi_1} - \frac{1}{mr^2}V_{\phi_2} + 2\frac{\dot{r}\dot{\theta}}{r} \\ \ddot{\phi}_2 &= -\left(1 + \frac{mr^2}{I_{2z}}\right)\frac{1}{mr^2}V_{\phi_2} - \frac{1}{mr^2}V_{\phi_1} + 2\frac{\dot{r}\dot{\theta}}{r} \\ \ddot{\theta} &= \frac{1}{mr^2}(V_{\phi_1} + V_{\phi_2}) - 2\frac{\dot{r}\dot{\theta}}{r}\end{aligned}\tag{5.2}$$

where  $m$  denotes the reduced mass of the two bodies in the system as  $m = \frac{m_1 m_2}{m_1 + m_2}$ ;  $V$  is the potential energy (for a complete definition the reader should refer [5]) and the subscripts denote against what the partial differentiation of  $V$  takes place;  $I_{1z}$  and  $I_{2z}$  denote the moment of inertia for the two bodies about the z-axis.

This was an introduction to the different ways in which earlier works have tried to model a binary system. The reader should refer to [5] to get more insight into these topics. We will now begin with describing the mutual potential formulation for a binary polyhedron system, and after that the force and the torque equations shall be presented which basically describe the coupled dynamics of the binary asteroid system.

## 5.2 MUTUAL POTENTIAL FORMULATION FOR TWO POLYHEDRONS

Let's begin with defining the underlying geometry that is used to build up the expression for the mutual potential. Each polyhedron is segmented into a collection of tetrahedrons called simplices. One of the vertices of each simplex is placed at the centroid of the polyhedron. The remaining three vertices form a triangular facet of the polyhedron. The position vectors are defined in an inertial reference frame, unless stated otherwise. We will denote the two asteroids with symbols  $A$  and  $B$ . The position vector to the centroid of body  $A$  is defined as  $\mathbf{A} = (x_A, y_A, z_A)$  and the position vector for a differential volume element  $dA$  in  $A$  is defined by  $\mathbf{a} = (x_a, y_a, z_a)$ , and in body-fixed frame the same is defined by  $\mathbf{a} - \mathbf{A} = (\Delta x_a, \Delta y_a, \Delta z_a)$ . Similar definitions also apply for a second body  $B$  [62]. These vectors can be visualized in Figure 5.3.

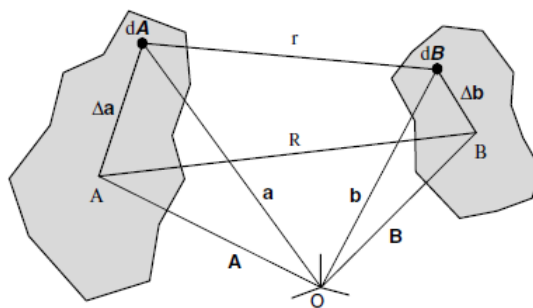


**Figure 5.3:** Vectors  $\mathbf{a}$  and  $\mathbf{b}$  denote the inertial position of the two differential volume elements, separated from each other by a distance  $r$ . Vectors  $\mathbf{A}$  and  $\mathbf{B}$  denote the inertial position of the two-body centroids, separated by a distance  $R$  [62].

The distance between the differential volumes is defined as follows [62]:

$$r^2 = (x_a - x_b)^2 + (y_a - y_b)^2 + (z_a - z_b)^2\tag{5.3}$$

$$r^2 = [(x_A - x_B) + (\Delta x_a - \Delta x_b)]^2 + [(y_A - y_B) + (\Delta y_a - \Delta y_b)]^2 + [(z_A - z_B) + (\Delta z_a - \Delta z_b)]^2\tag{5.4}$$

Following are the definition of two more vectors that will help in simplifying the notations [62]:

$$\mathbf{R} \equiv (x_A - x_B, y_A - y_B, z_A - z_B) \quad (5.5)$$

$$\mathbf{h} \equiv (\Delta x_a - \Delta x_b, \Delta y_a - \Delta y_b, \Delta z_a - \Delta z_b) \quad (5.6)$$

where their norms are obtained by scalar dot products as  $R^2 = \mathbf{R} \cdot \mathbf{R}$  and  $h^2 = \mathbf{h} \cdot \mathbf{h}$ . Then 'r' from Equation (5.3) and Equation (5.4) can be redefined as [62]:

$$r^2 = (\mathbf{R} + \mathbf{h}) \cdot (\mathbf{R} + \mathbf{h}) \quad (5.7)$$

$$r^2 = R^2 + h^2 + 2\mathbf{R} \cdot \mathbf{h} \quad (5.8)$$

The mutual potential is obtained by evaluating a pair of iterated integrals over the entire volume of the two bodies  $A$  and  $B$  [62]:

$$U \equiv \int \int \int_A \int \int \int_B \frac{1}{r} dB dA \quad (5.9)$$

The above equation can also be rewritten in terms of the tetrahedral simplices  $a$  and  $b$  from the two bodies as follows [62]:

$$U = \sum_{a \in A} \sum_{b \in B} \int \int \int_a \int \int \int_b \frac{1}{r} db da \quad (5.10)$$

The series expansion of the term  $(1/r)$  using Legendre polynomials (shown here until order 3) is given as [62]:

$$\frac{1}{r} = \left[ \frac{1}{R} \right] + \left[ \frac{-\mathbf{R} \cdot \mathbf{h}}{R^3} \right] + \left[ \frac{-h^2}{2R^3} + \frac{3(\mathbf{R} \cdot \mathbf{h})^2}{2R^5} \right] + \left[ \frac{3h^2(\mathbf{R} \cdot \mathbf{h})}{2R^5} - \frac{5(\mathbf{R} \cdot \mathbf{h})^3}{2R^7} \right] \quad (5.11)$$

A change of variables from  $(x,y,z)$  to barycentre formulation  $(u,v,w)$  is performed to carry out the integration in Equation (5.10) [62]. The vertex coordinates for a given simplex 'a' of body  $A$  (similar definitions apply for simplex  $b$  of body  $B$  as well) is given as [62]:

$$(x_1^a, y_1^a, z_1^a) = (x_A, y_A, z_A) + (\Delta x_1^a, \Delta y_1^a, \Delta z_1^a) \quad (5.12)$$

$$(x_2^a, y_2^a, z_2^a) = (x_A, y_A, z_A) + (\Delta x_2^a, \Delta y_2^a, \Delta z_2^a) \quad (5.13)$$

$$(x_3^a, y_3^a, z_3^a) = (x_A, y_A, z_A) + (\Delta x_3^a, \Delta y_3^a, \Delta z_3^a) \quad (5.14)$$

The coordinates of any vertex for a simplex  $a$  (and similarly for  $b$ ) in terms of the barycentre coordinates can be rewritten as [62]:

$$\begin{bmatrix} x_a \\ y_a \\ z_a \end{bmatrix} = \begin{bmatrix} x_A \\ y_A \\ z_A \end{bmatrix} + \begin{bmatrix} \Delta x_1^a & \Delta x_2^a & \Delta x_3^a \\ \Delta y_1^a & \Delta y_2^a & \Delta y_3^a \\ \Delta z_1^a & \Delta z_2^a & \Delta z_3^a \end{bmatrix} \begin{bmatrix} u_a \\ v_a \\ w_a \end{bmatrix} \quad (5.15)$$

where  $(u_a, v_a, w_a)$  are the barycentre coordinates for simplex  $a$  such that  $0 \leq (u_a, v_a, w_a, u_a + v_a + w_a) \leq 1$  [62]. The change of variables for integration requires introducing a certain Jacobian determinant which is described in the following equation [62]:

$$T_a = \det \begin{bmatrix} \Delta x_1^a & \Delta x_2^a & \Delta x_3^a \\ \Delta y_1^a & \Delta y_2^a & \Delta y_3^a \\ \Delta z_1^a & \Delta z_2^a & \Delta z_3^a \end{bmatrix} \quad (5.16)$$

A similar definition applies for  $T_b$ . The change to barycentre variables transforms each simplex  $a$  and  $b$  into a standard simplex form  $a'$  and  $b'$  respectively with barycentre coordinates as  $(0,0,0)$ ,

$(0,0,1)$ ,  $(0,1,0)$ , and  $(1,0,0)$  [62]. Using this new information, the mutual potential expression from Equation (5.10) changes to the following form [62]:

$$U = \sum_{a \in A} \sum_{b \in B} T_a T_b \int \int \int_{a'} \int \int \int_{b'} \frac{1}{r} db' da' \quad (5.17)$$

Now we are going to define some intermediate terms that will also be present in the final expression of the mutual potential. The reader is advised that from here onwards, unless stated otherwise, we adopt tensor notation and the Einstein summation convention and hence the reader should not attribute any significance to the distinction of superscript and/or subscript indices [62].

The coordinates to the vertices of the simplices  $a$  and  $b$ , relative to each body's centroid, are defined using three 6-element vectors (negative weight is given to the vertices of simplex  $b$ ) as follows [62]:

$$\mathbf{x}^i \equiv [\Delta x_1^a, \Delta x_2^a, \Delta x_3^a, -\Delta x_1^b, -\Delta x_2^b, -\Delta x_3^b] \quad (5.18)$$

$$\mathbf{y}^i \equiv [\Delta y_1^a, \Delta y_2^a, \Delta y_3^a, -\Delta y_1^b, -\Delta y_2^b, -\Delta y_3^b] \quad (5.19)$$

$$\mathbf{z}^i \equiv [\Delta z_1^a, \Delta z_2^a, \Delta z_3^a, -\Delta z_1^b, -\Delta z_2^b, -\Delta z_3^b] \quad (5.20)$$

Equation (5.18), Equation (5.19) and Equation (5.20) are stacked to define a new 3x6 matrix as follows [62]:

$$\mathbf{v}_j^i = \begin{bmatrix} \Delta x_1^a, \Delta x_2^a, \Delta x_3^a, -\Delta x_1^b, -\Delta x_2^b, -\Delta x_3^b \\ \Delta y_1^a, \Delta y_2^a, \Delta y_3^a, -\Delta y_1^b, -\Delta y_2^b, -\Delta y_3^b \\ \Delta z_1^a, \Delta z_2^a, \Delta z_3^a, -\Delta z_1^b, -\Delta z_2^b, -\Delta z_3^b \end{bmatrix}_j = \begin{bmatrix} \mathbf{x}_i \\ \mathbf{y}_i \\ \mathbf{z}_i \end{bmatrix}_j \quad (5.21)$$

We define another vector containing the barycenter variables [62]:

$$\mathbf{q}_i \equiv [u_a, v_a, w_a, u_b, v_b, w_b] \quad (5.22)$$

From Equation (5.11), the terms  $\mathbf{R} \cdot \mathbf{h}$  and  $h^2$  can be expressed using the above newly defined vectors. We begin with defining  $\mathbf{h}_j$  as follows [62]:

$$\mathbf{h}_j = [\mathbf{q}_i \mathbf{x}^i, \mathbf{q}_i \mathbf{y}^i, \mathbf{q}_i \mathbf{z}^i]_j \quad (5.23)$$

$$\mathbf{h}_j = \mathbf{q}_i \mathbf{v}_j^i \quad (5.24)$$

To clarify, we will expand one of the terms from the above equation:

$$\mathbf{q}_i \mathbf{x}^i = q_1 x_1 + q_2 x_2 + q_3 x_3 + q_4 x_4 + q_5 x_5 + q_6 x_6 \quad (5.25)$$

Next, we define the term  $\mathbf{R} \cdot \mathbf{h}$  [62]:

$$\mathbf{R} \cdot \mathbf{h} = \mathbf{R}^j \mathbf{h}_j \quad (5.26)$$

$$= \mathbf{R}^j \mathbf{q}_i \mathbf{v}_j^i \quad (5.27)$$

$$\equiv \mathbf{q}_i \mathbf{w}^i \quad (5.28)$$

where we have defined a 6-element vector  $\mathbf{w}^i$  for convenience [62]:

$$\mathbf{w}^i \equiv \mathbf{R}^j \mathbf{v}_j^i \quad (5.29)$$

The individual terms of the vector  $\mathbf{w}^i$  are defined as follows:

$$w^1 = R^1 v_1^1 + R^2 v_2^1 + R^3 v_3^1$$

$$w^2 = R^1 v_1^2 + R^2 v_2^2 + R^3 v_3^2$$

$$w^3 = R^1 v_1^3 + R^2 v_2^3 + R^3 v_3^3$$

⋮

$$w^6 = R^1 v_1^6 + R^2 v_2^6 + R^3 v_3^6$$

Note we used Einstein's summation convention to get the above individual elements of  $\mathbf{w}^i$ . To clarify further, consider the 3x6 matrix as defined in Equation (5.21), then, for example, the terms  $v_1^6, v_2^6, v_3^6$  are the first, second, and third-row elements in the 6<sup>th</sup> column of the matrix. Finally, we define the  $h^2$  term as follows [62]:

$$h^2 = \mathbf{h}_k \mathbf{h}_k \quad (5.30)$$

$$= \mathbf{q}_i \mathbf{v}_k^i \mathbf{q}_j \mathbf{v}_k^j \quad (5.31)$$

$$= (\mathbf{q}_i \mathbf{q}_j) (\mathbf{x}^i \mathbf{x}^j + \mathbf{y}^i \mathbf{y}^j + \mathbf{z}^i \mathbf{z}^j) \quad (5.32)$$

$$= \mathbf{q}_{ij} \mathbf{r}^{ij} \quad (5.33)$$

Where, we defined a rank 2 tensor  $\mathbf{q}_{ij} = \mathbf{q}_i \mathbf{q}_j$  such that  $\mathbf{q}_i$  will be a column vector and  $\mathbf{q}_j$  will be a row vector. We have also defined another rank 2 tensor,  $\mathbf{r}^{ij}$ , as follows [62]:

$$\mathbf{r}^{ij} \equiv \mathbf{x}^i \mathbf{x}^j + \mathbf{y}^i \mathbf{y}^j + \mathbf{z}^i \mathbf{z}^j \quad (5.34)$$

where, for example, a certain element of the tensor  $\mathbf{r}^{ij}$  will be defined as  $r^{23} = x^2 x^3 + y^2 y^3 + z^2 z^3$ . Note that the numbers are indices and not powers. The terms  $\mathbf{x}, \mathbf{y}, \mathbf{z}$  are as defined in Equation (5.18), Equation (5.19) and Equation (5.20) respectively. So basically, the term  $h^2$  is obtained as:

$$h^2 = \mathbf{q}_{11} \mathbf{r}^{11} + \mathbf{q}_{12} \mathbf{r}^{12} + \mathbf{q}_{13} \mathbf{r}^{13} + \dots + \mathbf{q}_{66} \mathbf{r}^{66} \quad (5.35)$$

We have described all the necessary intermediate terms that we shall find in the mutual potential expression and without showing any further derivation steps, we present the final expression as follows (only until order three) [62]:

$$U = \frac{G \rho_A \rho_B V_A V_B}{R} + G \sum_{a \in A} \sum_{b \in B} \rho_a \rho_b T_a T_b \left( \left[ -\frac{\mathbf{Q}_{ij} \mathbf{r}^{ij}}{2R^3} + \frac{3\mathbf{Q}_{ij} \mathbf{w}^i \mathbf{w}^j}{2R^5} \right] + \left[ \frac{3\mathbf{Q}_{ijk} \mathbf{r}^{ij} \mathbf{w}^k}{2R^5} - \frac{5\mathbf{Q}_{ijk} \mathbf{w}^i \mathbf{w}^j \mathbf{w}^k}{2R^7} \right] \right) \quad (5.36)$$

where the terms in the square brackets are the second and third-order terms, the first-order term vanishes because  $\mathbf{A}$  and  $\mathbf{B}$  are polyhedra centroids and expansion was centered at these centroids (see [62] for the proof) and the order-zero term is depicted by the first term on the right-hand side of Equation (5.36).  $V_A$  and  $V_B$  are the volumes of the two bodies respectively,  $G$  is the universal gravitational constant,  $\rho_A$  and  $\rho_B$  are the total densities of the two bodies,  $\rho_a$  and  $\rho_b$  represent the density of each individual tetrahedral simplex. The  $\mathbf{Q}$  are multi-rank tensors whose values (upto order 3) are given in [62].

A more generalized expression for the mutual potential (again, only till order 3 is shown here) can be presented as follows [12]:

$$U = G \sum_{a \in A} \sum_{b \in B} \rho_a T_a \rho_b T_b \left( \left[ \frac{\mathbf{Q}}{R} \right] + \left[ -\frac{\mathbf{Q}_i \mathbf{w}^i}{R^3} \right] + \left[ -\frac{\mathbf{Q}_{ij} \mathbf{r}^{ij}}{2R^3} + \frac{3\mathbf{Q}_{ij} \mathbf{w}^i \mathbf{w}^j}{2R^5} \right] + \left[ \frac{3\mathbf{Q}_{ijk} \mathbf{r}^{ij} \mathbf{w}^k}{2R^5} - \frac{5\mathbf{Q}_{ijk} \mathbf{w}^i \mathbf{w}^j \mathbf{w}^k}{2R^7} \right] \right) \quad (5.37)$$

### 5.3 FORCE TERMS FOR EQUATIONS OF MOTION FROM MUTUAL POTENTIAL DERIVATIVES

To compute the force acting on body  $A$  from body  $B$ , the mutual potential is differentiated with respect each component of the centroid coordinates of body  $A$ . Similarly, the force acting on body  $B$

is computed. We will again make use of tensor notation to depict the various vector terms [12]:

$$\mathbf{F}_\theta^A = \frac{\partial U}{\partial \mathbf{A}_\theta} \quad (5.38)$$

$$\mathbf{F}_\theta^B = \frac{\partial U}{\partial \mathbf{B}_\theta} \quad (5.39)$$

where  $\theta$  is just the tensor index. The above equations require us to differentiate the terms  $R$  and  $\mathbf{w}^i$  on the right-hand side of Equation (5.37). The differentiated terms are shown as follows [12]:

$$\frac{\partial R}{\partial \mathbf{A}_\theta} = -\frac{\mathbf{R}_\theta}{R} \quad (5.40)$$

$$\frac{\partial \mathbf{w}^i}{\partial \mathbf{A}_\theta} = -\mathbf{v}_\theta^i \quad (5.41)$$

where  $\mathbf{v}_\theta^i$  is as defined in Equation (5.21). Let the terms in the square bracket on the right-hand side of Equation (5.37) be denoted as  $\hat{U}_0$ ,  $\hat{U}_1$ ,  $\hat{U}_2$ , and  $\hat{U}_3$ . The partial derivatives of each of these terms is given as follows [12]:

$$\frac{\partial \hat{U}_0}{\partial \mathbf{A}_\theta} = \frac{\mathbf{Q}\mathbf{R}_\theta}{R^3} \quad (5.42)$$

The vector  $R_\theta$  is obtained as  $\mathbf{B} - \mathbf{A}$  where  $\mathbf{B}$  and  $\mathbf{A}$  are the inertial coordinates of the centroids of the respective bodies.

$$\frac{\partial \hat{U}_1}{\partial \mathbf{A}_\theta} = -\frac{3\mathbf{Q}_i \mathbf{R}_\theta \mathbf{w}^i}{R^5} + \frac{\mathbf{Q}_i \mathbf{v}_\theta^i}{R^3} \quad (5.43)$$

$$\frac{\partial \hat{U}_2}{\partial \mathbf{A}_\theta} = -\frac{3\mathbf{Q}_{ij} \mathbf{r}^{ij} \mathbf{R}_\theta}{2R^5} + \frac{15\mathbf{Q}_{ij} \mathbf{R}_\theta \mathbf{w}^i \mathbf{w}^j}{2R^7} - \frac{3\mathbf{Q}_{ij} \mathbf{w}^i \mathbf{v}_\theta^j}{R^5} \quad (5.44)$$

$$\frac{\partial \hat{U}_3}{\partial \mathbf{A}_\theta} = \frac{15\mathbf{Q}_{ijk} \mathbf{r}^{ij} \mathbf{R}_\theta \mathbf{w}^k}{2R^7} - \frac{3\mathbf{Q}_{ijk} \mathbf{r}^{ij} \mathbf{v}_\theta^k}{2R^5} - \frac{35\mathbf{Q}_{ijk} \mathbf{R}_\theta \mathbf{w}^i \mathbf{w}^j \mathbf{w}^k}{2R^9} + \frac{15\mathbf{Q}_{ijk} \mathbf{w}^i \mathbf{w}^j \mathbf{v}_\theta^k}{2R^7} \quad (5.45)$$

Thus the force acting on body  $A$  is given as follows [12]:

$$\mathbf{F}_\theta^A = G \sum_{a \in A} \sum_{b \in B} \rho_a T_a \rho_b T_b \left[ \frac{\partial \hat{U}_0}{\partial \mathbf{A}_\theta} + \frac{\partial \hat{U}_1}{\partial \mathbf{A}_\theta} + \frac{\partial \hat{U}_2}{\partial \mathbf{A}_\theta} + \frac{\partial \hat{U}_3}{\partial \mathbf{A}_\theta} \right] \quad (5.46)$$

From Newton's Law, we know that the force acting on body  $B$  is the negative of that acting on body  $A$ . The force term described by Equation (5.46) is defined in the inertial reference frame, however sometimes it is easier to work with a body-fixed frame. Consider a frame fixed to the centroid of body  $A$ , then the relative position vector as expressed in this frame is given as [12]:

$$\mathbf{R} = P^T (\mathbf{B} - \mathbf{A}) \quad (5.47)$$

where  $P^T$  is a transformation matrix that transforms a quantity in the inertial frame to the body-fixed frame. Expressed in the body-fixed frame, the relative force term can be expressed as follows [12]:

$$\mathbf{F}_{rel} = \frac{\partial U}{\partial \mathbf{R}} \quad (5.48)$$

Now we already have a function to compute  $\partial U / \partial \mathbf{B}$  which is:

$$\frac{\partial U}{\partial \mathbf{B}} = -\mathbf{F}_\theta^A \quad (5.49)$$

We do not have to write a separate piece of code to evaluate Equation (5.48) as all we have to do is to substitute  $\mathbf{R}$  from Equation (5.47) as argument instead of  $\mathbf{B}$  into the code for Equation (5.49). We can not use  $\partial U / \partial \mathbf{A}$  obviously because the body-fixed frame is attached to body  $A$ .

## 5.4 TORQUE TERMS FOR EQUATIONS OF MOTION FROM MUTUAL POTENTIAL DERIVATIVES

Let's define  $P$  as the matrix that maps from body-fixed frame of body  $A$  to the inertial frame, and  $S$  be the matrix mapping from the body-fixed frame of body  $B$  to the inertial frame. One of the ways to get the torque expressions in the coupled dynamics is to take the partial derivative of the mutual potential  $U$  with respect to either of the mapping matrices,  $P$  or  $S$ . By chain rule of differentiation, this will ultimately lead to the partial derivative of the  $\mathbf{v}$  (see Equation (5.21)) with respect to the mapping matrix [12]. We shall redefine the format of writing the tensor  $\mathbf{v}$  from Equation (5.21) by making use of the aforementioned transformation matrices as follows [12]:

$$\mathbf{v} = [P[\Delta r^{a1}, \Delta r^{a2}, \Delta r^{a3}], -S[\Delta r^{b1}, \Delta r^{b2}, \Delta r^{b3}]] \quad (5.50)$$

where each  $\Delta r^{(a,b)i}$  represents a column vector depicting the coordinates of the vertex ( $i = 1, 2$ , or  $3$ ) of given polyhedron face,  $a$  or  $b$ . The coordinates are specified in the body-fixed frame of the respective body  $A$  or  $B$ . We shall consider the case wherein we want to express the equations for torque in a frame fixed to body  $A$ . In that sense, Equation (5.50) will change as follows [12]:

$$\mathbf{v} = [[\Delta r^{a1}, \Delta r^{a2}, \Delta r^{a3}], -P^T S[\Delta r^{b1}, \Delta r^{b2}, \Delta r^{b3}]] \quad (5.51)$$

A new transformation matrix is defined called  $T$  such that it maps from the body-fixed frame of body  $B$  to the inertial frame and then ultimately to the body-fixed frame of body  $A$  and is calculated as  $T = P^T S$ . To get the expressions for torque in the body-fixed frame of  $A$ , the mutual potential expression is differentiated with respect to the transformation matrix  $T$  and as per the chain rule, this requires the differentiation of the tensor  $\mathbf{v}$  with respect to  $T$ . Therefore, differentiating Equation (5.51) with respect to  $T$  (we resume tensor notation from here onwards) gives the following result [12]:

$$\frac{\partial \mathbf{v}_j^i}{\partial T_{\phi\theta}} = [0_{j\theta}^{\phi i}, \delta_j^\phi \Delta r_\theta^{(b)i}] = \mathbf{D}_{j\theta}^{\phi i} \quad (5.52)$$

where the term  $\mathbf{D}_{j\theta}^{\phi i}$  is a rank 4 tensor; the term  $\delta_j^\phi$  is a rank 2 tensor called the Kronecker delta function; the term  $\Delta r_\theta^{(b)i}$  is a rank 2 tensor and the superscript  $(b)$  is not a tensor index but rather it denotes the facet  $b$  of body  $B$ . The result from Equation (5.52) will be utilized in obtaining the torque terms.

We proceed to show the derivatives of the potential terms  $\hat{U}_0$ ,  $\hat{U}_1$ ,  $\hat{U}_2$ , and  $\hat{U}_3$  with respect to the transformation matrix  $T$ , also called the attitude rotation matrix. The mutual potential term  $\hat{U}_0$  does not have any attitude dependence as we can see from Equation (5.37); the terms with attitude dependence are the ones which have the tensors  $\mathbf{w}$  and  $\mathbf{r}$  in Equation (5.37). For the remaining potential terms, we show the derivative results without the underlying derivation steps. For the latter, the reader should refer to [12].

$$\frac{\partial \hat{U}_1}{\partial T_{\phi\theta}} = -\frac{\mathbf{Q}_i \mathbf{R}^j \mathbf{D}_{j\theta}^{\phi i}}{R^3} \quad (5.53)$$

$$\frac{\partial \hat{U}_2}{\partial T_{\phi\theta}} = -\frac{\mathbf{Q}_{ij} \mathbf{v}_p^i \mathbf{D}_{p\theta}^{\phi j}}{R^3} + \frac{3\mathbf{Q}_{ij} \mathbf{w}^i \mathbf{R}^p \mathbf{D}_{p\theta}^{\phi j}}{R^5} \quad (5.54)$$

$$\frac{\partial \hat{U}_3}{\partial T_{\phi\theta}} = \frac{3\mathbf{Q}_{ijk}}{2R^5} \left[ 2\mathbf{v}_p^i \mathbf{D}_{p\theta}^{\phi j} \mathbf{w}^k + \mathbf{r}^{ij} \mathbf{R}^p \mathbf{D}_{p\theta}^{\phi k} \right] - \frac{15\mathbf{Q}_{ijk} \mathbf{w}^i \mathbf{w}^j \mathbf{R}^p \mathbf{D}_{p\theta}^{\phi j}}{2R^7} \quad (5.55)$$

The resulting partial derivative of the mutual potential expression with respect to the attitude matrix  $T$  can be shown as follows [12]:

$$E_{\phi\theta} = G \sum_{a \in A} \sum_{b \in B} \rho_a T_a \rho_b T_b \left[ \frac{\partial \hat{U}_1}{\partial T_{\phi\theta}} + \frac{\partial \hat{U}_2}{\partial T_{\phi\theta}} + \frac{\partial \hat{U}_3}{\partial T_{\phi\theta}} \right] \quad (5.56)$$

Note that the mapping matrix  $T$  could be in any reference frame and it would not change the definition or form of Equation (5.52) to Equation (5.56), but for our case, we will consider that the mapping or attitude matrix  $T$  is defined in the body-fixed frame of body  $A$ , and in extension this means that Equation (5.52) to Equation (5.56) are also defined in the same reference frame.  $E_{\phi\theta}$  is a rank 2 tensor the columns of which are designated as  $E = [E^\alpha, E^\beta, E^\gamma]$ . Now that we have mentioned all the relevant terms, we can express the torque terms for the equations of motion that define relative motion of the two bodies in the body-fixed frame of  $A$  as follows [12]:

$$\mu_a = \left[ P^T (\mathbf{B} - \mathbf{A}) \right] \times (-\mathbf{F}_{rel}) - \alpha_T \times E^\alpha - \beta_T \times E^\beta - \gamma_T \times E^\gamma \quad (5.57)$$

$$\mu_b = \alpha_T \times E^\alpha + \beta_T \times E^\beta + \gamma_T \times E^\gamma \quad (5.58)$$

where  $\alpha_T, \beta_T, \gamma_T$  are the columns of the mapping matrix  $T$  from left to right [12].

## 5.5 EQUATIONS OF MOTION FOR THE FULL 2-BODY PROBLEM

The coupled equations of motion shown in this section have been obtained from [12] and [33]. These equations of motion are defined in the body-fixed frame of  $A$ . Not expressing the equations in an inertial frame and using a body-fixed frame helps in reducing the size of the state vector for the equations of motion, which is always advantageous from a simulation point of view. They are presented as follows:

$$\dot{\mathbf{P}} = \mathbf{P} \times \Omega_A - \mathbf{F}_{rel} \quad (5.59)$$

where  $\mathbf{P}$  is the relative linear momentum expressed in body-fixed frame of body  $A$ . Relative momentum is computed as the product of the reduced mass of the two bodies expressed as  $m = \frac{m_A m_B}{m_A + m_B}$  and the rate of change of the relative position vector  $\mathbf{R}$  as expressed by Equation (5.47).  $\Omega_A$  is the angular velocity of body  $A$  expressed in its own body frame.

$$\dot{\mathbf{R}} = \mathbf{R} \times \Omega_A + \frac{\mathbf{P}}{m} \quad (5.60)$$

$$\dot{\Gamma}_B = \Gamma_B \times \Omega_A + \mu_B \quad (5.61)$$

where  $\Gamma_B$  is the angular momentum of body  $B$  expressed in the body-fixed frame of  $A$ .

$$\dot{\Gamma}_A = \Gamma_A \times \Omega_A + \mu_A \quad (5.62)$$

where  $\Gamma_A$  is the angular momentum of body  $A$  expressed in the body-fixed frame of  $A$ .

$$\dot{T} = T \hat{\Omega}_B - \hat{\Omega}_A T \quad (5.63)$$

where  $\Omega_B$  is the angular velocity of body  $B$  expressed in its own frame. The term  $\hat{\Omega}$ , for both  $A$  and  $B$ , consists of the three components of the angular momentum vector  $\Omega = [\Omega_x, \Omega_y, \Omega_z]^T$  arranged in a 3x3 matrix as shown below [33]:

$$\hat{\Omega} = \begin{bmatrix} 0 & -\Omega_z & \Omega_y \\ \Omega_z & 0 & -\Omega_x \\ -\Omega_y & \Omega_x & 0 \end{bmatrix} \quad (5.64)$$

Given the inertia tensors  $\mathbf{I}_A$  and  $\mathbf{I}_B$  for the bodies  $A$  and  $B$  respectively and expressed in their own body frames, the angular velocity vectors can be written as follows [12]:

$$\boldsymbol{\Omega}_A = \mathbf{I}_A^{-1} \boldsymbol{\Gamma}_A \quad (5.65)$$

$$\boldsymbol{\Omega}_B = \mathbf{I}_B^{-1} T^T \boldsymbol{\Gamma}_B \quad (5.66)$$

$$(5.67)$$

## 5.6 CONCLUSION

In this chapter, we discussed the different ways in which the two-body problem has been modeled in literature so far. More importance was given to the polyhedron approach since it was selected to model the gravitational potential in Chapter 4. The mutual potential that governs the motion of the two asteroids is mentioned following which the force and torque terms are explained that govern the coupled motion of the two-body system. All equations of motion are expressed in the body-fixed frame of body  $A$ , which is basically the primary asteroid in the binary system. Expressing equations of motion in the body-fixed frame allows one to reduce the size of the state vector compared to the case of using an inertial reference frame, thus easing the load on the dynamics simulator. It is important to solve the two-body problem with high accuracy since the position and attitude of the two asteroids directly affects the gravitational force acted upon an orbiting spacecraft or particle. Thus using a high-fidelity polyhedra model for the full 2-body problem will help in improving the accuracy of determining the trajectory of an orbiting particle/spaceship.

# 6

## THE RESTRICTED FULL 3 BODY PROBLEM

### 6.1 INTRODUCTION

In this chapter we will discuss the dynamics of the particle in motion around the binary asteroid system. We will consider that this particle in motion around the binary system is massless (basically its mass is negligibly small compared to the mass of either of the asteroids in the binary system) and so it will not affect the coupled dynamics of the binary asteroid system (see Chapter 5) itself. This particular problem in astrodynamics is referred to as the *Restricted Full Three-Body Problem*. The *Restricted* term refers to the fact that we have considered the third body, the orbiting particle in this case, to be massless. The *Full* refers to the fact that the motion of the two primaries in the three-body problem, in this case the two primaries are the two asteroids, has not been simplified. We discussed the high-fidelity full two-body problem in Chapter 5. As always, our main focus would be on discussing the three body problem for the case where the asteroids are modeled as two polyhedrons, but a brief discussion on the three body problem for other binary asteroid models (as discussed previously in Chapter 5) will also be presented in this chapter.

#### 6.1.1 CIRCULAR RESTRICTED THREE-BODY PROBLEM

The circular restricted three-body problem is a classic and fundamental astrodynamics problem. The acceleration of the third particle, in orbital motion around the two primaries (where the primaries, along with the third body, are all point masses), is derived from the gradient of the gravitational potential function  $U$ . In the barycentric rotating frame, the equations of motion are expressed as follows [5]:

$$\ddot{\rho} + 2\omega \times \dot{\rho} + \omega \times (\omega \times \rho) + \dot{\omega} \times \rho = \frac{\partial U}{\partial \rho} \quad (6.1)$$

In the above non-normalized equations of motion, the term  $U$  combines the gravitational potential of both the primary and secondary body,  $\rho$  specifies the position vector of the orbiting particle, defined in the barycentric rotating reference frame,  $\omega$  is the angular velocity of the rotating two-body system, defined in the barycentric rotating reference frame.

#### 6.1.2 SPHERE-ELLIPSOID RESTRICTED THREE-BODY PROBLEM

The orbital motion of the particle is modeled assuming that the primary and secondary are modeled as an ellipsoid and sphere respectively. The three-body geometry is depicted in Figure 6.1 [5]:

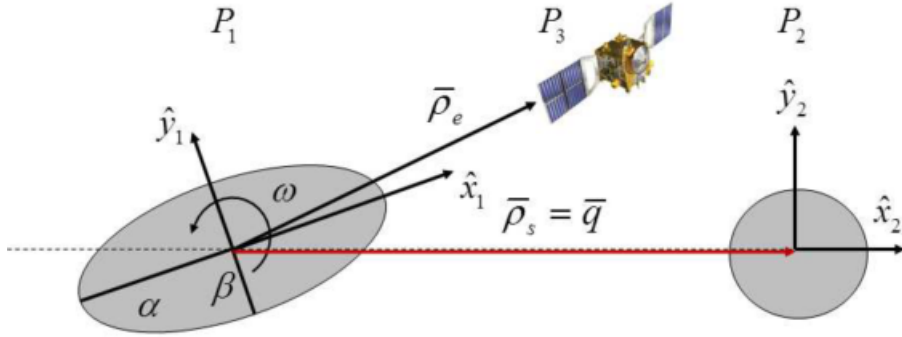


**Figure 6.1:** Geometry of the Sphere-Ellipsoid restricted three-body problem [5].

Note that the position vector of the orbiting particle or spacecraft is defined in the body-fixed frame of the ellipsoid, denoted by the symbol  $\rho_e$ . The vector  $\rho_s$  in Figure 6.1 denotes the position of the centre of mass of the sphere with respect to the ellipsoid body-fixed frame. The equation of motion for the massless third particle is given as [5]:

$$\ddot{\rho}_e + 2\omega \times \dot{\rho}_e + \omega \times (\omega \times \rho_e) + \dot{\omega} \times \rho_e = \frac{\partial U_{SE}}{\partial \rho_e} + \frac{\partial U_{e1}}{\partial \rho_s} \quad (6.2)$$

where  $\omega$  is the angular rate of the ellipsoid. The term  $U_{SE}$  is defined as  $U_{SE} = \mu U_s + (1 - \mu) U_{e1}$  where  $U_s$  and  $U_{e1}$  are the gravitational potential of the sphere and ellipsoid respectively. The term  $\mu$  is the mass parameter of the system defined as  $\mu = m_2/(m_1 + m_2)$  where  $m_1$  and  $m_2$  are the masses of the primary and secondary asteroid, respectively, in the binary system [5].

### 6.1.3 ELLIPSOID-ELLIPSOID RESTRICTED THREE-BODY PROBLEM

Here, the motion of the massless particle is computed assuming that the binary system is comprised of two ellipsoids. The geometry for this system is depicted in Figure 6.2:

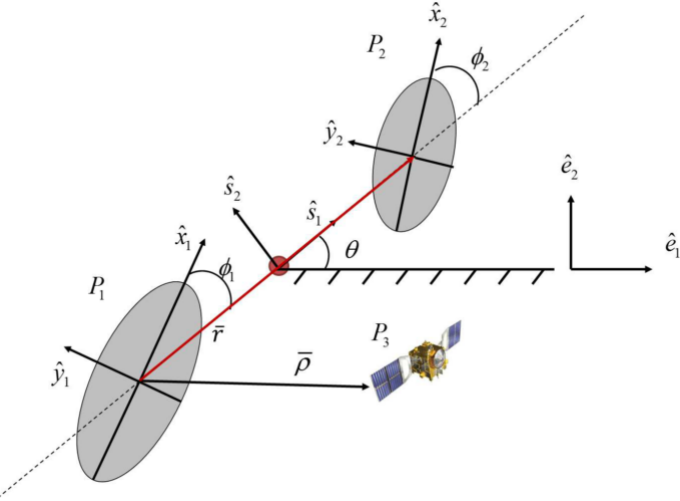


**Figure 6.2:** Geometry of the Ellipsoid-Ellipsoid restricted three-body problem [5].

The position vector of the spacecraft is defined relative to the primary asteroid in the binary system and expressed in the inertial reference frame. The equation describing the motion of the

third particle, in the inertial reference frame, is given as follows [5]:

$$\ddot{\rho} = \frac{\partial U_{EE}}{\partial \rho} \quad (6.3)$$

The gravitational potential term  $U_{EE}$  is computed as  $U_{EE} = (1 - \mu)U_{e1} + \mu U_{e2}$ , where,  $\mu$  is the mass parameter and is computed the same way as described in Section 6.1.2. The terms  $U_{e1}$  and  $U_{e2}$  denote the potential of the primary and secondary ellipsoids in the binary system [5].

## 6.2 POLYHEDRON-POLYHEDRON RESTRICTED FULL THREE-BODY PROBLEM

Herein, we will focus more on the discussion of the equation of motion for the restricted full three-body problem assuming that the binary system is modeled as two polyhedrons. We begin by first defining the non-dimensional equation of motion. The reference frame under consideration is fixed to the rotating primary asteroid in the binary system (implying that the reference frame is rotating with the same angular velocity vector as the primary asteroid) but the frame's origin is fixed to the binary system's barycenter. For future reference, let's call this frame **RF1**. The equation of motion for a massless particle in **RF1** can be stated as follows [54]:

$$\ddot{\rho} + 2\Omega \times \dot{\rho} + \dot{\Omega} \times \rho + \Omega \times (\Omega \times \rho) = \frac{\partial U_{12}}{\partial \rho} \quad (6.4)$$

where  $\Omega$  is the angular rate of the primary asteroid defined in **RF1** or equivalently, in the primary asteroid's own frame. The term  $\rho$  is the position vector of the particle, defined and originating from **RF1**. The potential term  $U_{12}$  will be defined later. Now let's define a second reference frame which is fixed to the primary asteroid and also has its origin fixed to the centre of mass of the asteroid body. We will call this frame **RF2**. The equation of motion for a massless particle in this frame is defined as follows [11]:

$$\ddot{\rho} + 2\Omega \times \dot{\rho} + \dot{\Omega} \times \rho + \Omega \times (\Omega \times \rho) + \ddot{r}_1 = \frac{\partial U_{12}}{\partial \rho} \quad (6.5)$$

where  $\ddot{r}_1$  denotes the inertial acceleration of the centroid of the primary asteroid. The vector  $\rho$  is still computed from the binary barycentre to the orbiting particle but expressed in **RF2**. We normalize the equation of motion for the third particle by considering a new unit for length, mass and time. For length  $L$  we choose the largest dimension of the primary asteroid, for mass we can choose the total mass of the binary system i.e.  $m_T = m_1 + m_2$ , and for time we can choose the mean motion for the aforementioned new units of mass and length i.e.  $n = \sqrt{G(m_1 + m_2)/L^3}$  [11]. Then the normalized position vector is given as  $\varrho = \rho/L$  and the normalized angular velocity vector is given as  $\omega = \Omega/n$  [54]. The normalized inertial position vector of the centroid of the primary asteroid will then be  $R_1 = r_1/L$ . The normalized equation of motion, as expressed in **RF2**, is stated as:

$$\ddot{\varrho} + 2\omega \times \dot{\varrho} + \dot{\omega} \times \varrho + \omega \times (\omega \times \varrho) + \ddot{R}_1 = \frac{\partial U_{12}}{\partial \varrho} \quad (6.6)$$

The potential term  $U_{12}$  is formulated with the same terminology and form as described for Equation (3.68). The expression is given as follows [11]:

$$U_{12} = -G\sigma_1 \left[ -\frac{1}{2} \sum_{e \in edges_1} \vec{r}_{e1} \cdot E_{e1} \cdot \vec{r}_{e1} \cdot L_{e1} + \frac{1}{2} \sum_{f \in faces_1} \vec{r}_{f1} \cdot F_{f1} \cdot \vec{r}_{f1} \cdot w_{f1} \right] \\ -G\sigma_2 \left[ -\frac{1}{2} \sum_{e \in edges_2} \vec{r}_{e2} \cdot E_{e2} \cdot \vec{r}_{e2} \cdot L_{e2} + \frac{1}{2} \sum_{f \in faces_2} \vec{r}_{f2} \cdot F_{f2} \cdot \vec{r}_{f2} \cdot w_{f2} \right] \quad (6.7)$$

where the subscripts 1 and 2 refer to the primary and secondary asteroid respectively; G is the normalized gravity constant and for the normalization terms currently being used, its value is unity;

$\sigma_1$  and  $\sigma_2$  are constant body densities for the two asteroids and they too are normalized [11]. The other terms in Equation (6.7) are defined properly in Section 3.6. A very important thing to note here is that, no matter which reference frame is used to express the equation of motion for the third particle, its relative position vector, used in quantities  $\vec{r}_e$ ,  $\vec{r}_f$ ,  $L_e$ , and  $w_f$ , should be expressed in the body frame of the respective asteroid [11]. For this purpose we will define two attitude rotation matrices, one for each asteroid.  $R_1$  will map from the body-fixed frame of the primary asteroid to the frame of the equation of motion (**RF1** or **RF2**) and similarly we define  $R_2$  for the secondary asteroid. Of course, if the frame **RF2** is used to express the equation of motion then  $R_1$  will be an identity matrix. The transpose of both  $R_1$  and  $R_2$  are used to express the relative position vector of the third particle in the respective body frames. These rotation matrices appear in the partial derivative of the potential term  $U_{12}$  [11].

The partial derivative of the potential  $U_{12}$  is given as follows [11]:

$$\begin{aligned} \frac{\partial U_{12}}{\partial \rho} = & -G\sigma_1 R_1 \left[ -\frac{1}{2} \sum_{e \in edges_1} E_{e1} \cdot \vec{r}_{e1} \cdot L_{e1} + \frac{1}{2} \sum_{f \in faces_1} F_{f1} \cdot \vec{r}_{f1} \cdot w_{f1} \right] \\ & -G\sigma_2 R_2 \left[ -\frac{1}{2} \sum_{e \in edges_2} E_{e2} \cdot \vec{r}_{e2} \cdot L_{e2} + \frac{1}{2} \sum_{f \in faces_2} F_{f2} \cdot \vec{r}_{f2} \cdot w_{f2} \right] \end{aligned} \quad (6.8)$$

The second partial derivative of  $U_{12}$  or the gravity gradient matrix is expressed as follows [11]:

$$\begin{aligned} \frac{\partial^2 U_{12}}{\partial \rho^2} = & -G\sigma_1 R_1 \left[ -\frac{1}{2} \sum_{e \in edges_1} E_{e1} \cdot L_{e1} + \frac{1}{2} \sum_{f \in faces_1} F_{f1} \cdot w_{f1} \right] R_1^T \\ & -G\sigma_2 R_2 \left[ -\frac{1}{2} \sum_{e \in edges_2} E_{e2} \cdot L_{e2} + \frac{1}{2} \sum_{f \in faces_2} F_{f2} \cdot w_{f2} \right] R_2^T \end{aligned} \quad (6.9)$$

### 6.2.1 LINEARIZATION

The computation of gravitational attraction, as we can see from Equation (6.8), at a given field point in the vicinity of the binary asteroid system requires summation over all faces and edges of the two asteroids. A polyhedron, even at a small resolution, has hundreds of facets or faces and here we are dealing with two such polyhedrons which means that performing a summation over all the faces and edges will be computationally intensive. A linearization method, developed in [58], helps in reducing the said computational load. For a given state, say  $X_0$ , we first compute the gravitational potential  $U_{12}^{X_0}$ , the gravitational attraction  $\partial U_{12}^{X_0}/\partial \rho$  and the gravity gradient matrix  $\partial^2 U_{12}^{X_0}/\partial \rho^2$  using Equation (6.7), Equation (6.8) and Equation (6.9) respectively. Then, in the vicinity of this reference state  $X_0$  we can compute the potential and its partial derivative for a state  $X$  as follows [58]:

$$U_{12}^X = U_{12}^{X_0} + (X - X_0) \frac{\partial U_{12}^{X_0}}{\partial \rho} + (X - X_0) \frac{\partial^2 U_{12}^{X_0}}{\partial \rho^2} (X - X_0) \quad (6.10)$$

$$\frac{\partial U_{12}^X}{\partial \rho} = \frac{\partial U_{12}^{X_0}}{\partial \rho} + (X - X_0) \frac{\partial^2 U_{12}^{X_0}}{\partial \rho^2} \quad (6.11)$$

Equation (6.10) and Equation (6.11) provide an approximation for the potential and its partial derivative only in the immediate neighborhood of the state  $X_0$ . For this reason, one should specify a certain limit  $\Delta X_{max} = (X - X_0)_{max}$  wherein this approximation will be applied [58]. Following this method would definitely help in reducing the simulation time by a considerable amount.

### 6.3 CONCLUSION

In this chapter we began the discussion with models for the three-body problem. Except for the circular restricted three body problem, every other model presented in this chapter conforms to the restricted full 3-body problem formulation. The term *Restricted* refers to the fact that the third body is modeled as a massless particle and the term *Full* refers to the fact that the remaining two bodies in the problem have not been considered as point mass objects but rather the dynamics, both rotational and translational, of the bodies have been modeled considering their specific geometric shapes. The polyhedron-polyhedron restricted full three body problem has been discussed in more detail than the other models since it is the approach which has been chosen to study the long term orbital motion of a third particle due to the higher level of accuracy offered by it. This model is used not only to study the motion of a third particle around it but also to simulate the motion of the binary asteroids around each other. Expressions for the potential, gravitational attraction and the gravity gradient matrix were presented. A linearization approach to reduce the computational loads in calculating the potential and its derivatives was also presented in this chapter.



# 7

## NUMERICAL INTEGRATION METHODS

### 7.1 INTRODUCTION

We have been acquainted with the full two-body problem and the restricted full three-body problem and in both cases we have witnessed that the equations of motion are highly complex. An analytical solution for those equations of motion can not be obtained and so to study the dynamical behavior of the binary or the tertiary system, we have to numerically integrate the equations and observe and store the state after each time step. Several methods have been developed for integrating differential equations and most of these methods have been successfully applied to the field of astrodynamics. We will be looking into the basic properties and principles of some important integration methods such as:

- Runge-Kutta methods - Easy to use and most commonly applied [36]
- Multistep methods - Offer high accuracy but require storage of previous data points [36]
- Extrapolation methods - Popular for their extremely high accuracy [36]
- Taylor Series Method - Popular for high-precision and long-time numerical integration [1]

Every method has its own set of pros and cons and it's not easy to pinpoint and select any one integration method. The aim of this chapter will be to present enough details, including the advantages and disadvantages, on each method so that at the end we can make an informed, smart, and logical decision about which integration method will be best suited for our particular application. We will present some general differential equation that will be used as reference for discussing the integration methods. The second-order differential equation expressing the acceleration for an orbiting particle is given as a function of time, position, and velocity as follows [36]:

$$\ddot{\mathbf{r}} = \mathbf{a}(t, \mathbf{r}, \dot{\mathbf{r}}) \quad (7.1)$$

where  $\ddot{\mathbf{r}}$  is the acceleration,  $\dot{\mathbf{r}}$  is the velocity, and  $\mathbf{r}$  is the position of the orbiting particle. The six dimensional position and velocity vector is given as:

$$\mathbf{y} = \begin{bmatrix} \mathbf{r} \\ \dot{\mathbf{r}} \end{bmatrix} \quad (7.2)$$

Then, the differential equation of motion is given as [36]:

$$\dot{\mathbf{y}} = \mathbf{f}(t, \mathbf{y}) = \begin{bmatrix} \dot{\mathbf{r}} \\ \mathbf{a}(t, \mathbf{r}, \dot{\mathbf{r}}) \end{bmatrix} \quad (7.3)$$

These general equations will be used when explaining the integration methods in the following sections.

## 7.2 RUNGE-KUTTA METHODS

Given the initial values  $y_0$  at some time  $t_0$ , we can approximate the value  $y$  at some time  $t_0 + h$  as follows [36]:

$$\mathbf{y}(t_0 + h) \approx \mathbf{y}_0 + h\dot{\mathbf{y}}_0 \quad (7.4)$$

$$= \mathbf{y}_0 + h f(t_0, \mathbf{y}_0) \quad (7.5)$$

where  $h$  is the *step size*, and the above process is called the *Euler Step*. Using Equation (7.5), one can obtain approximate values  $\eta_i$  of the solution of the differential equation at specific times  $t_i = t_0 + i h \forall i = 1, 2, 3, \dots$  [36]. The step size should be sufficiently small so that the approximate solution obtained over multiple time steps is still close to the actual solution and does not diverge from it. A better approximating method is given below [36]:

$$\mathbf{y}(t_0 + h) \approx \mathbf{y}_0 + h\phi = \eta(t_0 + h) \quad (7.6)$$

where  $\eta(t_0 + h)$  is the approximate solution to the differential equation, and  $\phi$  is called as the incremental function. In the classical RK4 (Runge-Kutta 4) method, the incremental function is given as follows [36]:

$$\phi_{RK4} = \frac{1}{6}(\mathbf{k}_1 + 2\mathbf{k}_2 + 2\mathbf{k}_3 + \mathbf{k}_4) \quad (7.7)$$

where the  $\mathbf{k}$  terms are defined as [36]:

$$\mathbf{k}_1 = f(t_0, \mathbf{y}_0) \quad (7.8)$$

$$\mathbf{k}_2 = f(t_0 + h/2, \mathbf{y}_0 + h\mathbf{k}_1/2) \quad (7.9)$$

$$\mathbf{k}_3 = f(t_0 + h/2, \mathbf{y}_0 + h\mathbf{k}_2/2) \quad (7.10)$$

$$\mathbf{k}_4 = f(t_0 + h, \mathbf{y}_0 + h\mathbf{k}_3) \quad (7.11)$$

The RK4 method can approximate the exact solution upto terms of order  $h^4$ , which means that if one reduces the step size for integration by, say half, then the resulting global error from the numerical integration will reduce by a factor of 16. It also means that the difference between the approximated solution and the exact solution i.e. the local truncation error, will be of the order of  $h^5$ . In general an RK (Runge-Kutta) method is said to be of order  $p$  if the local truncation error is of order  $h^{p+1}$  or if the approximated solution matches the exact solution upto an order of  $h^p$  [14]. The local truncation error in the RK4 method is given as follows [36]:

$$e_{RK4} = |y(t_0 + h) - \eta(t_0 + h)| \leq \text{const.} h^5 \quad (7.12)$$

what we discussed right now was the RK4 method, as an example, but we can also present a more generalized approach to the (explicit) Runge-Kutta methods.

### 7.2.1 GENERAL RUNGE-KUTTA METHODS

The general Runge-Kutta method consists of two tasks: the first one is to compute the *s-stage* values which are needed for forming the incremental function  $\phi$ , and the second part is to finally compute the approximated solution of the differential equation at a given time  $t_n$ . So, for an *s-stage* RK method, the following *s* function evaluations:

$$k_1 = f(t_0 + c_1 h, y_0) \quad (7.13)$$

$$k_i = f(t_0 + c_i h, y_0 + h \sum_{j=1}^{i-1} a_{ij} k_j) \quad \forall i = 2, 3, \dots s \quad (7.14)$$

are utilized in creating the increment function  $\phi$  as follows [36]:

$$\phi = \sum_{i=1}^s b_i k_i \quad (7.15)$$

from which the approximate solution is obtained as:

$$\eta(t_0 + h) = y_0 + h\phi \quad (7.16)$$

The coefficients  $c_i$ ,  $b_i$ , and  $a_{ij}$  are usually presented in a tabular form, called the *Butcher's Tableau*, as shown in Figure 7.1 [36]. These coefficients are chosen such that they maximize the order  $p$  of

$c_1$					
$c_2$	$a_{21}$				
$c_3$	$a_{31}$	$a_{32}$			
$\vdots$	$\vdots$	$\vdots$	$\ddots$		
$c_s$	$a_{s1}$	$a_{s2}$	$\dots$	$a_{s,s-1}$	
	$b_1$	$b_2$	$\dots$	$b_{s-1}$	$b_s$

**Figure 7.1:** The Butcher's Tableau depicting the coefficients used in the RK methods [36].

the local truncation error. They are determined in a manner such that they satisfy the following relations [36]:

$$\sum_{i=1}^s b_i = 1 \quad (7.17)$$

$$c_1 = 0 \quad (7.18)$$

$$c_i = \sum_{j=1}^{i-1} a_{ij} \quad (i > 1) \quad (7.19)$$

For higher-order RK methods, specifically the 6<sup>th</sup> and the 8<sup>th</sup> order, the coefficients are presented in the appendix of [24] in the form of the *Butcher's Tableau*.

### 7.2.2 EMBEDDED RUNGE-KUTTA METHODS

It is possible to develop RK methods of neighboring orders that are based on the same set of  $s$  function evaluations. This is called as *embedded* RK method. What we do in this method is that we evaluate the regular RK method but independently for two different yet nearby orders, say for example orders 10 and 8, and then we get two independent estimates of the solution of the differential equation from which we try to estimate the local truncation error. This method allows a very easy estimation of the local truncation error which is utilized in efficient stepsize control (discussed later) during the integration process.

An  $s$ -stage embedded RK method will yield two independent approximations of the exact solution and these are expressed as follows [36]:

$$\eta(t_0 + h) = y_0 + h \sum_{i=1}^s b_i k_i \quad (7.20)$$

$$\hat{\eta}(t_0 + h) = y_0 + h \sum_{i=1}^s \hat{b}_i k_i \quad (7.21)$$

with orders  $p$  and  $p + 1$  respectively, with local truncation error given as follows [36]:

$$e = |y(t_0 + h) - \eta(t_0 + h)| \leq \text{const.} h^{p+1} \quad (7.22)$$

$$\hat{e} = |y(t_0 + h) - \hat{\eta}(t_0 + h)| \leq \text{const.} h^{p+2} \quad (7.23)$$

we can see from the above equation that  $\hat{e}$  is smaller than  $e$  by an order of  $h$ , this allows us to make the following approximation [36]:

$$e = |y - \eta| \approx |\hat{\eta} - \eta| \quad (7.24)$$

which basically indicates that we can estimate the local truncation error of the RK method of order  $p$  just by taking the difference of the two outcomes of the embedded RK method. At this point, we should also discuss the embedded RK notation, which is usually given in the literature as  $RKp(q)-s$ , where  $RK$  refers to Runge-Kutta,  $p$  refers to the actual order of the RK method that we intend to use to perform our integration,  $q$  refers to the neighboring order of RK method that we use as part of the embedded RK procedure which is used only to estimate the local truncation error, and finally  $s$  represents the number of  $s$ -stage evaluations involved in both the  $p$  and  $q$  order RK methods [36]. The coefficients for the RK8(7)-13 method, which is considered as a high-order RK method, is given in the reference [36] in the *Butcher's Tableau* format.

As stated before, an easy estimation of the local truncation error will help in efficient step size control during the integration process, which is our next topic of discussion.

### 7.2.3 STEP SIZE CONTROL

In numerical integration, it is desired that every integration step contributes uniformly towards the total integration error. This can be achieved by an approach called the *Step Size Control*. A common method for performing stepsize control is with the embedded RK method wherein we can easily estimate the truncation error at each step. The stepsize control method then tries to limit this local truncation error for each step [36].

Now for a given step size  $h$ , we perform the integration step using the embedded RK method and then the estimated local truncation error is given as [36]:

$$e(h) \approx |\hat{\eta} - \eta| \quad (7.25)$$

If the above local truncation error is larger than a given tolerance value  $\epsilon$  then the same integration step is repeated but this time with a smaller step size  $h^*$ . The new local truncation error can then be computed as [36]:

$$e(h^*) = e(h) \left( \frac{h^*}{h} \right)^{p+1} \quad (7.26)$$

where  $p$  is as defined earlier, the order of the RK method. We know that  $e(h^*)$  has to be smaller than the specified tolerance  $\epsilon$  which means that the maximum allowable value of  $e(h^*)$  can be equal to the specified tolerance and no more than that. From this information we can reverse engineer the maximum allowable value for the step size  $h^*$  as follows [36]:

$$h^* = \sqrt[p+1]{\frac{\epsilon}{e(h)}} \times h \quad (7.27)$$

Using the above step size or a lower value, the integration step is repeated in the scenario when the original step size  $h$  results in a local truncation error greater than a specified tolerance. If the integration step with  $h^*$  is successful (ideally it should be since it has been reverse calculated from the tolerance), then the same can be used for the next integration step. However the reader should note that the new step-size value is allowed to differ from the old step-size value only by a factor of 2 to 5 and no more than that to avoid rapid oscillations in step-size change. This whole process

of step-size control continues for every integration step to ensure uniformity in individual local truncation errors. This process can be automated in a computer code but to initiate the process, the user obviously has to provide an initial guess for the starting step size [36].

#### 7.2.4 RUNGE-KUTTA-NYSTRÖM METHODS

RKN (Runge-Kutta-Nyström) methods have been developed especially for second-order differential equations, the kind we usually deal with in astrodynamics. The approach involves converting the second-order differential equation of the form given by Equation (7.1) into a system of first-order differential equations and then perform the standard RK method over it. Doing this, one arrives at the following solution [36]:

$$\begin{aligned}\mathbf{r}(t_0 + h) &= \mathbf{r}_0 + h\mathbf{v}_0 + h^2 \sum_i \bar{b}_i k_i^* \\ \mathbf{v}(t_0 + h) &= \mathbf{v}_0 + h \sum_i b_i k_i^*\end{aligned}\quad (7.28)$$

where  $r$  represents the position vector,  $v$  represents the velocity vector and is equal to  $\dot{r}$  from Equation (7.1),  $r_0$  and  $v_0$  are the initial position and velocity,  $h$  is the step size. The term  $k_i^*$  is defined as follows [36]:

$$k_i^* = a \left( t_0 + c_i h, \mathbf{r}_0 + c_i h\mathbf{v}_0 + h^2 \sum_j \bar{a}_{ij} k_j^*, \mathbf{v}_0 + h \sum_j a_{ij} k_j^* \right) \quad (7.29)$$

where the coefficients are defined as follows [36]:

$$\begin{aligned}\bar{a}_{ij} &= \sum_K a_{iK} a_{Kj} \\ \bar{b}_i &= \sum_j b_j a_{ji}\end{aligned}\quad (7.30)$$

Apparently, the advantages of the RKN method over the standard RK method is seen only when the second-order differential equation does not have any dependence on the velocity or the first derivative term on the right-hand side of Equation (7.1) [36]. We have seen from the equations of motion of the full two-body problem and restricted full three-body problem that the acceleration term always has explicit dependence on the velocity term. So an early conclusion regarding only the RKN method can be made that since it does not offer any advantage over the regular RK method, it shall not be used for the future thesis work.

### 7.3 MULTISTEP METHODS

So far what we discussed, the Runge-Kutta methods, can be classified as single-step methods since all individual integration steps are independent of each other. The  $s$ -stage function evaluations do not depend on the values that were computed in the previous integration steps. Thus, this method requires no storage of values from previous integration steps and in a way helps in reducing loads on the computer memory for a simulator. But in a way one can also say that all those computed values are being 'wasted' and that they can be utilized for future integration step computations. This is where the Multistep Method comes into the picture. This category of numerical integrators require storage of previous step values as they are utilized in future computations. We will begin with a brief introduction to the core principles of multistep integration methods.

We will consider the differential equation of the form  $\dot{y} = f(t, y)$ . It is assumed that we already have some initial approximate solutions to the differential equation, let's call these solutions  $\eta_j$ , at equidistant time values say  $t_j = t_0 + jh$  where  $j = 0, 1, 2, \dots, i$ . Now consider a polynomial  $p(t)$  that interpolates some values  $f_j = f(t_j, \eta_j)$  at previous times  $t_j$  for which we already have the approximate solutions  $\eta_j$ . Now we already have approximate solutions until the time value  $t_i$  as we said earlier,

but we need to perform the integration step to get the approximate solution for the next time step i.e. at  $t = t_i + h$ . This is shown in the form of an equation as follows [36]:

$$\eta_{i+1} = \eta_i + \int_{t_i}^{t_i+h} p(t) dt = \eta_{i+1} = \eta_i + h\phi \quad (7.31)$$

where  $\phi$  is the incremental function. So from this we can get the following result [36]:

$$\phi = \frac{1}{h} \int_{t_i}^{t_i+h} p(t) dt \quad (7.32)$$

This forms the basis of the multistep method. We see that we need previous function evaluations  $f_j$  from previous time steps and use it to create an interpolating polynomial which is then utilized to create the incremental function  $\phi$  that is ultimately utilized in performing the next integration step. The initial values to start a multistep method integration process can be obtained by using a high-order standard Runge-Kutta method i.e. get the function values, store them and then use them for future multistep integration steps.

### 7.3.1 ADAMS-BASHFORTH METHODS

In this subsection we will utilize the introductory ideas presented earlier and present a multistep integration method called as the AB (Adams-Bashforth) method. Now consider that we already have certain  $m$  data points, which are basically previous time steps and the corresponding function values, given as follows [36]:

$$(t_{i-m+1}, f_{i-m+1}), \dots, (t_i, f_i) \quad (7.33)$$

So the values in the bracket above are already known. Now what we do is, we create an interpolating polynomial based on these known data points, let's call this polynomial as  $p_m^i(t)$  and it is given as follows [36]:

$$p_m^i(t) = \sum_{j=0}^{m-1} (-1)^j \begin{bmatrix} -\sigma \\ j \end{bmatrix} \nabla^j f_i \quad (7.34)$$

where

$$\begin{bmatrix} -\sigma \\ j \end{bmatrix} = \frac{(-\sigma)(-\sigma-1)\dots(-\sigma-j+1)}{j!} \quad (7.35)$$

is called the binomial coefficient. The term  $\nabla^j f_i$  calculates the backward-differences of the known function values  $f$  as follows [36]:

$$\begin{aligned} \nabla^0 f_i &= f_i \\ \nabla^1 f_i &= f_i - f_{i-1} \\ \nabla^n f_i &= \nabla^{n-1} f_i - \nabla^{n-1} f_{i-1} \end{aligned} \quad (7.36)$$

Using these newly defined expressions and notations, we can finally design the increment function  $\phi$  for an  $m$  order AB method integrator as follows [36]:

$$\phi_{ABm} = \frac{1}{h} \int_{t_i}^{t_i+h} p_m^i(t) dt = \sum_{j=0}^{m-1} \gamma_j \nabla^j f_i \quad (7.37)$$

where the coefficient  $\gamma$  is computed from a recurrence relation [36]:

$$\gamma_j = 1 - \sum_{k=0}^{j-1} \frac{1}{j+1-k} \gamma_k \quad (7.38)$$

The starting value of  $\gamma$  can be taken as 1. Thus by using Equation (7.36), Equation (7.37) and Equation (7.38), we can finally compute the solution of the differential equation for the next time step as follows:

$$\eta_{i+1} = \eta_i + h\phi \quad (7.39)$$

The reader should note that  $\eta_i$  is already known,  $h$  is the step size, and  $\phi$  is obtained using Equation (7.36), Equation (7.37) and Equation (7.38). The local truncation error for the AB method is computed as [36]:

$$e_{ABm} \approx h^{m+1} |\gamma_m f_i^{(m)}| \quad (7.40)$$

where  $f_i^{(m)}$  is the  $m^{\text{th}}$  derivative of  $f$  which is computed using Equation (7.36). The approach we presented utilizes the backward-differences of the function  $f_i$  but there is another approach listed in [36], which avoids computing the backward-differences, that can also be used which is more convenient and efficient to use. As per this method the increment function can be written only in terms of the function values  $f_j$  as follows:

$$\phi_{ABm} = \sum_{j=1}^m \beta_{mj} f_{i-m+j} \quad (7.41)$$

where the coefficients  $\beta$  are calculated as follows:

$$\beta_{mj} = (-1)^{m-j} \sum_{l=m-j}^{m-1} \gamma_l \begin{bmatrix} l \\ m-j \end{bmatrix} \quad \forall j = 1, \dots, m \quad (7.42)$$

where the binomial coefficient is calculated in the same way as that in Equation (7.35). This approach does not allow easy local error-estimation and change of order between subsequent integration steps, unlike the backward-difference approach.

### 7.3.2 ADAMS-MOULTON AND PREDICTOR-CORRECTOR METHODS

In the previous multistep method, AB method, the polynomial  $p(t)$  was defined using the function values upto and including  $f_i$  at time  $t_i$  but the integration was performed for the next time step i.e. from  $t_i$  to  $t_{i+1}$ . Another multistep method called the AM method constructs the polynomial  $p(t)$  using the function value upto and including  $f_{i+1}$  at time  $t_{i+1}$  thus making the integrated solution more accurate than the AB method. The polynomial for this AM (Adams-Moulton) method is given as [36]:

$$p_m^{i+1}(t) = \sum_{j=0}^{m-1} (-1)^j \begin{bmatrix} -\sigma + 1 \\ j \end{bmatrix} \nabla^j f_{i+1} \quad (7.43)$$

where all terms are computed in the same manner as explained for Equation (7.34). The incremental function is given as [36]:

$$\phi_{AMm} = \sum_{j=0}^{m-1} \gamma_j^* \nabla^j f_{i+1} \quad (7.44)$$

where the coefficient  $\gamma_j^*$  can be evaluated using the recurrence relation [36]:

$$\gamma_j^* = - \sum_{k=0}^{j-1} \frac{1}{j+1-k} \gamma_k^* \quad (7.45)$$

Like before, the starting  $\gamma$  value can be taken as 1. The local truncation error for the AM method is given as [36]:

$$e_{AMm} \approx h^{m+1} |\gamma_m^* f_i^{(m+1)}| \quad (7.46)$$

For the same order of integrator,  $m$ , the AM method has a smaller error per step than the AB method since the error constant  $\gamma_m^*$  is smaller than  $\gamma_m$  [36]. Just like the AB method, the AM method can also be designed without having to use the backward-differences of  $f_j$  function values and so the new increment function is defined as follows [36]:

$$\phi_{AMm} = \sum_{j=1}^m \beta_{mj}^* f_{i+1-m+j} \quad (7.47)$$

where the coefficient is defined as [36]:

$$\beta_{mj}^* = (-1)^{m-j} \sum_{l=m-j}^{m-1} \gamma_l^* \begin{bmatrix} l \\ m-j \end{bmatrix} \quad \forall j = 1, \dots, m \quad (7.48)$$

Computing the next integration step is not that direct in case of the AM method as compared to the AB method because the increment function evaluation depends on a future function evaluation  $f_{i+1}$  at time  $t_{i+1}$  and so we can not simply use the relation like the one given in Equation (7.39) to perform the integration. The way this works is, that one has to combine an order  $m$  AB method with an order  $m$  or  $m+1$  AM method in a so-called PECE (Predictor-Corrector) algorithm to get the solution  $\eta_{i+1}$  for the differential equation. The algorithm is listed as follows [36]:

- Calculate the initial estimate of the solution to the differential equation at time  $t_{i+1}$  using the AB method.
- Using the estimated solution previously computed, the function value  $f_{i+1}$  at time  $t_{i+1}$  is calculated.
- Using the function value previously computed, the new incremental function for the AM method is calculated and through it the new estimate of the solution to the differential equation is calculated.
- Using the new estimate of the solution, the function value  $f_{i+1}$  is recomputed which will be utilized in the next integration step.

In principle, the last two steps mentioned in the algorithm above have to be repeated until convergence is achieved for the AM method but doing so will result in repeated evaluation of the function value  $f_{i+1}$  and then recomputation of the incremental function  $\phi$ . This will demand considerable computational effort, but [36] mentions that the PECE algorithm can be implemented if one can accept slightly higher local truncation error. A relative value for this error is not easy to provide since it depends on how many iterations one performs to get the best estimate of the solution. If computational resources can be increased, then performing multiple iterations of the final two steps in the algorithm should be feasible.

The reader should note that when it comes to multistep integration methods, stability becomes an issue when we are using high-order integrators. One has to be careful with the selected step size because even if the local truncation error is small, the global integration error can increase exponentially if the appropriate stepsize for higher-order multistep methods is not chosen. This is not an issue with lower-order integrators even if a relatively large step size is used for them. Using the PECE algorithm improves the stability of the multistep integration method considerably [36]. Figure 7.2 depicts what we just discussed, as one can see, the AB method of order 8 becomes highly unstable relative to its lower-order counterpart. The combined AB and AM method as discussed in the PECE algorithm, denoted in the graphs as 'ABM8', offers lowest global errors and remains highly stable over the course of integration even with twice the step size as that for the other two methods depicted in the graph [36]. Clearly, we have a winner in this scenario.

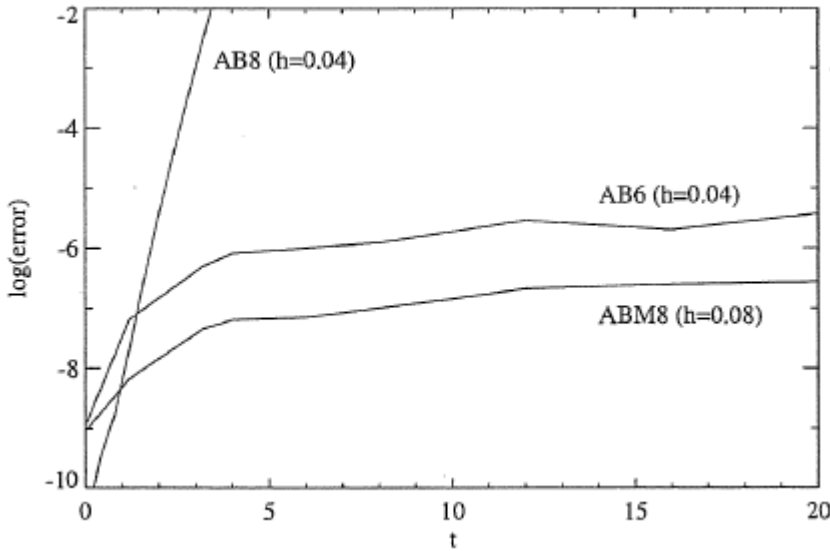


**Figure 7.2:** Global integration error versus time for different multistep methods and their order. ABM refers to the Adams-Basforth-Moulton method which is basically the PECE algorithm. [36].

Since we will be working with perturbing accelerations as well in our simulations, [36] suggests that only the central gravitational field acceleration term should be updated with the new coordinates obtained from the third step (corrector step) of the PECE algorithm and the perturbing acceleration should be updated with the output of coordinates from the first step (predictor step) of the PECE algorithm only. This increases the stability of the integrator when one is dealing with orbital perturbations in their simulators. [36] also recommends that for the purpose of orbit simulations, one should use multiistep methods of orders in the range of 8 to 12.

### 7.3.3 VARIABLE-ORDER AND VARIABLE STEP SIZE METHODS

The Adam methods that we have discussed so far, perform integration with a constant step size, but in some cases, one may have to change the step size in between the integration to reduce the local errors so that the integrator remains stable and the global errors do not increase exponentially. For arbitrary step sizes the  $m^{th}$ -order predictor formula (AB method) for the computation of the estimated solution at the next time step i.e.  $t_{i+1}$  can be written as [36]:

$$\eta_{i+1} = \eta_i + (t_{i+1} - t_i) \sum_{j=0}^{m-1} g_j(i) \phi_j(i) \quad (7.49)$$

where the coefficients are defined as follows [36]:

$$g_j(i) = \frac{1}{t_{i+1} - t_i} \int_{t_i}^{t_{i+1}} \prod_{l=0}^{j-1} \frac{t - t_{i-l}}{t_{i+1} - t_{i-l}} dt \quad (7.50)$$

$$\phi_j(i) = \prod_{l=0}^{j-1} (t_{i+1} - t_{i-l}) f[t_i, \dots, t_{i-j}] \quad (7.51)$$

where the term  $f[t_i, \dots, t_{i-j}]$  is called divided differences and is defined as follows [36]:

$$\begin{aligned} f[t_i] &= f_i \\ f[t_i, t_{i-1}] &= \frac{f_i - f_{i-1}}{t_i - t_{i-1}} \\ f[t_i, t_{i-1}, t_{i-2}] &= \frac{f[t_i, t_{i-1}] - f[t_{i-1}, t_{i-2}]}{t_i - t_{i-2}} \end{aligned} \quad (7.52)$$

To use the variable-order and stepsize method, the error for the current order and nearby order is calculated for the predictor formula first. A new step size based on the estimated error for the current order and step size is also estimated. The error-estimation formula is given in Equation (7.40). A stepsize change is performed only if the new step size requires a change from the current one by a factor of 2 or more. The change in order is done by changing the value of  $m$  in the predictor formula to  $m - 1$  or  $m + 1$ .

## 7.4 EXTRAPOLATION METHODS

Extrapolation methods are powerful, in the sense that they offer extremely high accuracy in the integration process. These methods are, like their Runge-Kutta counterparts, single step methods.

### 7.4.1 MID-POINT RULE

Consider the differential equation of the form  $\dot{y} = f(t, y)$  with given initial conditions  $y(t_0) = y_0$ . We want to calculate the solution to the differential equation at some time  $t_0 + H$ . To do this, the time interval  $[t_0, t_0 + H]$  is first converted into  $n$  number of steps, each of equal size  $h = H/n$ . For the first time step we obtain an approximation  $u_1$  using the simple *Euler Step* through Equation (7.5) and obtain further approximations  $u_i$  using the so-called *mid-point rule*. These are shown as follows [36]:

$$\begin{aligned} u_1 &= y_0 + hf(t_0, y_0) \\ u_{i+1} &= u_{i-1} + 2hf(t_0 + ih, u_i) \end{aligned} \quad (7.53)$$

This gives an approximate solution to the differential equation at time  $t_0 + H$  as follows [36]:

$$y(t_0 + H) \approx \eta(h) = \frac{1}{4}u_{n-2} + \frac{1}{2}u_{n-1} + \frac{1}{4}u_n \quad (7.54)$$

The error between the exact solution and the approximated solution is an asymptotic expansion in the square of the stepsize  $h^2$  and so the error can be reduced drastically by employing small step size.

### 7.4.2 EXTRAPOLATION

The method presented earlier, is of low order and one of the ways to increase the order of integration is by performing the integration step again with a different step size  $h^*$  all the while keeping the result from the old step size as well. Then we can use the following formula [36]:

$$y(t_0 + H) \approx \eta^* = \frac{h^{*2}\eta(h) - h^2\eta(h^*)}{h^{*2} - h^2} \quad (7.55)$$

By doing the above process, the error in the integration step is reduced by two orders i.e. reduced by an order of  $h^2$ . We can use even higher-order extrapolation formulas to further improve the order of integration. This is done by basically performing the same integrations step with several step sizes  $h_i = H/n_i$  where  $n_i = 2, 4, 6, 8, 12, \dots$ . The higher-order extrapolation then takes place as follows [36]:

$$y(t_0 + H) \approx \eta_{i,j+1} = \frac{h_{i-j}^2\eta_{i,j} - h_i^2\eta_{i-1,j}}{h_{i-j}^2 - h_i^2} \quad (7.56)$$

The above equation depends on the sequence shown in Figure 7.3. Each entry in the figure is a combination of the entries to the left and upper left of it and this is exactly what is done in Equation (7.56). Thus to get a high-order estimate to the solution of the differential equation, a given integration step has to be done again and again with different step sizes using the mid point rule so that towards the end and using the sequence given in Figure 7.3 we can obtain a highly accurate estimate of the true solution.

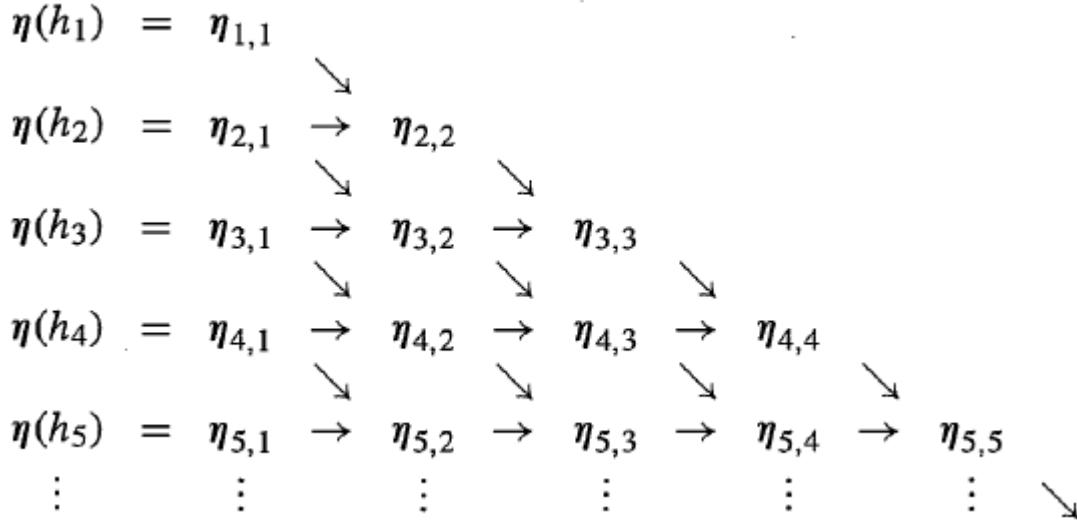


**Figure 7.3:** Extrapolating sequence, called the Burlisch Sequence [36].

To get an idea on the error estimate, [36] mentions that each value  $\eta_{ij}$  in column  $j$  of the sequence shown in Figure 7.3 provides an approximation of the true solution comparable to that provided by the RK method of order  $2j$ . So when high accuracy is required, extrapolation methods definitely beat the Runge-Kutta methods.

## 7.5 LIE GROUP VARIATIONAL INTEGRATOR

When it comes to simulating rigid-body dynamics such as the full two-body problem we discussed in Chapter 5, one should not use general numerical integration methods because they fail to preserve the geometric characteristics of the dynamics. For example, if we use Runge-Kutta method for numerical integration of the full two-body equation of motion, then with time the rotation matrices, say  $R$ , will drift from the orthonormal rotation group; the quantity  $R^T R$  will drift from being an identity matrix. This means that the attitude of the rigid bodies cannot be accurately determined and since the gravitational force and moment due to the gravitational mutual potential both depend on the attitude of the rigid bodies, their computations will no longer be accurate, which will ultimately lead to a wrong two-body simulation. A solution to curb this problem is the LGVI (Lie Group Variational Integrator) [13].

The equations of motion presented in Chapter 5 are continuous in time but LGVI works with a discretized version of those equations. For a full derivation, the reader should refer to [32]. The discrete time equations for the relative motion of the binary system (motion relative to one of the asteroids in the binary system) in the full two-body problem in Lagrangian form are presented as follows [32]:

$$F_{2_n} X_{n+1} - 2X_n + F_{2_{n-1}}^T X_{n-1} = -\frac{h^2}{m} \frac{\partial U_n}{\partial X_n} \quad (7.57)$$

where  $X$  is the relative position of body 1 (henceforth **B1**) with respect to body 2 (henceforth **B2**);  $h$  is the stepsize of integration;  $U$  is the mutual gravitational potential;  $m$  is the mass ratio of the two bodies defined as  $\frac{m_1 m_2}{m_1 + m_2}$ ;  $F_2$  is a matrix that represents the relative attitude for **B2** between two integration steps and it ensures that the attitude matrix of **B2** i.e.  $R_2$  will not drift from the orthonormal rotation group [32]. The  $F_2$  matrix is related to the rotation matrix as  $F_{2_n} = R_{2_n}^T R_{2_{n+1}}$ . A similar definition applies for the  $F_1$  matrix as well. In the lines of relative motion a matrix  $F$  is also defined such that  $F = RF_1R^T$ , where  $R$  is the relative attitude of **B1** with respect to **B2**. The subscript

$n$  denotes the integration step number.

$$F_{n+1} J_{dR_{n+1}} - J_{dR_{n+1}} F_{n+1}^T = F_{2_n}^T (F_n J_{dR_n} - J_{dR_n} F_n^T) F_{2_n} + h^2 S(M_{n+1}) \quad (7.58)$$

where  $J_{dR}$  is the non-standard moment of inertia matrix for **B1** with respect to **B2** and is defined as  $J_{dR} = R J_d R^T$  [32]. The body-specific non-standard moment of inertia matrix  $J_{d_i}$  where  $i = 1, 2$  for bodies 1 and 2, is related to the standard moment of inertia matrix  $J_i$  as  $J_{d_i} = \text{trace}[J_{d_i}] I_{3x3} - J_{d_i}$  [32].  $I_{3x3}$  is the identity matrix. The term  $S(M)$ , where  $M$  is the moment due to the gravity potential, in Equation (7.58) is determined by the following relationship [13]:

$$S(M) = \frac{\partial U}{\partial R} R^T - R \frac{\partial U}{\partial R} \quad (7.59)$$

The partial derivative of the mutual gravitational potential with respect to the relative attitude matrix has already been presented in Equation (5.56). The notation is different but the meaning of the terms is still the same. Let's move on to the other discrete time equations used for the LGVI:

$$F_{2_{n+1}} J_{d_2} - J_{d_2} F_{2_{n+1}}^T = F_{2_n}^T (F_{2_n} J_{d_2} - J_{d_2} F_{2_n}^T) F_{2_n} + h^2 X_{n+1} \times \frac{\partial U_{n+1}}{\partial X_{n+1}} + h^2 S(M_{n+1}) \quad (7.60)$$

$$R_{n+1} = F_{2_n}^T F_n R_n \quad (7.61)$$

$$R_{2_{n+1}} = R_{2_n} F_{2_n} \quad (7.62)$$

So Equation (7.57), Equation (7.58), Equation (7.60), Equation (7.61) and Equation (7.62) are effectively what are used to propagate the two-body problem. They comprise the LGVI. Given the initial conditions  $(X_0, R_0, R_{2_0}, X_1, R_1, R_{2_1})$ , Equation (7.61) and Equation (7.62) can be used to obtain  $F_0$  and  $F_{2_0}$ . Then Equation (7.58) and Equation (7.60) can be used to obtain the terms  $F_1$  and  $F_{2_1}$ . Then the terms  $X_2, R_2, R_{2_2}$  can be obtained by solving Equation (7.57), Equation (7.61) and Equation (7.62). This process is then continued again and again to propagate the two-body model [32]. This is the Lie group variational integration process which, here, has been given specifically for the two-body problem.

## 7.6 TAYLOR SERIES METHOD

TSM (Taylor Series Method) has been used in the past for numerical integration of ODE (Ordinary Differential Equation) in the study of dynamical systems. TSM has been used in the past in studies concerning Celestial Mechanics and where high-precision was required for long-term numerical simulations (see [1] and references therein). TSM has been the topic of extensive research in the field of applied mathematics. Although the theory behind this particular method for numerical integration is straight forward, its practical implementation is extremely cumbersome. In the literature, one can find several software implementations of TSM. The list of the most important implementations is given in [1]. In this section, we will particularly discuss one of the implementations (a software package written in the C programming language) [30], called TAYLOR, that can be used for our application. We will begin with a brief discussion on the theory of numerical integration with TSM, following which we will briefly look into what the TAYLOR software does and how it can potentially be used for our application.

Consider the initial value problem in the following general form (where  $t$  is the independent variable) [30]:

$$\begin{aligned} \dot{x}(t) &= f(t, x(t)) \\ x(t_0) &= x_0 \end{aligned} \quad (7.63)$$

where  $f$  is an analytic function in its domain of definition,  $x_0$  is the initial value or the starting value of the variable  $x$  corresponding to the initial time  $t_0$ . Given the initial condition  $x(t_0) = x_0$ , the value

$x(t_0 + h)$  (where  $h$  is the step size of integration) is approximated by the Taylor Series Expansion of the solution  $x(t)$  at  $t = t_0$  [30]:

$$\begin{aligned} x_0 &= x(t=0) \\ x_{m+1} &= x_m + \dot{x}(t_m)h + \frac{\ddot{x}(t_m)h^2}{2!} + \dots + \frac{\frac{\delta^p x(t_m)}{\delta t^p}h^p}{p!} \end{aligned} \quad (7.64)$$

where  $p$  is the degree of the Taylor Series expansion,  $m = 0, \dots, M - 1$  and  $M$  is the total number of steps involved in the integration process. Note that the TSM does not require a reduction in step size of the integrator to increase its accuracy; increasing the order of the Taylor expansion increases the integrator's accuracy [30]. In theory, Equation (7.64) describes how the integration is done for an ODE. For simplicity, we will henceforth represent the  $j^{th}$  derivative of the dependent variable  $x$  with respect to time as  $x^{(j)}(t)$ . In practice, to implement TSM, one has to compute the values of the derivatives  $x^{(j)}(t_m)$  and substitute them in Equation (7.64) to get the value of  $x_{m+1}$  i.e. the integrated value of  $x$ . The theoretical way to achieve this is by differentiating the first expression in Equation (7.63) with respect to time, at  $t = t_m$  [30]. This is illustrated as follows:

$$\begin{aligned} x^1(t_m) &= f(t_m, x(t_m)) \\ x^2(t_m) &= f_t(t_m, x(t_m)) + f_x(t_m, x(t_m))x^1(t_m) \end{aligned} \quad (7.65)$$

where  $f_t$  and  $f_x$  are the derivatives of the function  $f$  (defined in Equation (7.63)) with respect to time and  $x$  respectively. Thus, for the order  $p$  of the Taylor expansion in Equation (7.64), the derivatives of the function  $f$  (upto order  $p$ ) have to be computed first. Then for each integration step, these derivatives have to be evaluated at  $t = t_m$  to obtain the coefficients for the expansion given in Equation (7.64) [30].

For the full two-body and the restricted full three-body problem that we had discussed earlier in Chapter 5 and Chapter 6, respectively, obtaining the coefficients for the Taylor expansion will be cumbersome, especially for relatively high-orders of expansion, because the differential equations of motion have a complex structure. However, there is a recursive numerical technique called AD (Automatic Differentiation) that allows fast computation of derivatives upto any order [30]. The topic of AD is quite comprehensive and as such can not be covered in this literature study. However, an explanation on AD can be found in [30] (also see references therein) along with a worked out example using the Van Der Pol equation. The first step in AD technique is to decompose the function  $f$  in an ODE (see the first expression in Equation (7.63)) into a sequence of smaller functions, which when utilizes simple algebraic operations such as addition, multiplication, subtraction, division, real powers, exponentials, logarithms and trigonometry, obtains the original function  $f$  in the ODE. The example using Van Der Pol equation in [30] illustrates the decomposition process properly. The reason why we decompose is because AD provides simple formulas for calculating the  $n^{th}$  derivative of a function that can be decomposed into a sequence of basic operations. These formulas can also be found in [30], referred to as *propositions* in the paper. Once the expressions for calculating the  $n^{th}$  derivative of the basic functions are obtained, they can be used recursively to calculate the  $n^{th}$  derivative of the function  $f$  in order to get the coefficients of the Taylor expansion in Equation (7.64). This process is also illustrated properly in the same example as mentioned before, in [30]. There is no general code for computing derivatives of a function using the AD technique; instead AD has to be coded separately for different systems [30]. Fortunately, if we use the TAYLOR software provided by [30], then we do not have to code the AD separately as the software does that internally.

The TAYLOR software, reads a set of differential equations provided by the user, decomposes them to apply AD and then generates a C code as its output that can compute all the coefficients in the Taylor expansion (see Equation (7.64)) for a given point  $(t_m, x_m)$  [30]. So basically, the input to the software is the set of differential equations that have to be integrated (in our case, these would be

the equations of motion for the two or the three-body problem) and the output of the software is a complete numerical integrator (with an option to have automatic step-size and order control) based on the TSM [30]. The output consists of a *C* code and corresponding header file for the integrator. This allows the user to make a function call to the integrator from their *main* code. An example on using the TAYLOR software for the R3BP (Restricted Three-Body Problem) is given in [30]. The example explains how to provide the set of differential equations to the software and the commands needed to get a compiled *C* code for the integrator out of it.

We will now summarize the results, pertaining to the performance and applicability of TAYLOR for short and long-time simulation of the R3BP, presented in [30]. The accuracy of the software in a short-time simulation was tested for; the authors of [30] called it the *local error* test. For one unit of time, numerical integration of the R3BP was performed, once using double precision and then again with extended precision (with twice the order of Taylor expansion than that used for the double precision simulation and with the same step-size). The relative error in the final position and velocity components, obtained from the two different simulations was computed and was found to be in the order of the machine precision epsilon<sup>1</sup>. The value for the latter was  $2.22 \times 10^{-16}$  [30]. The actual values for the errors can be found in [30]. Note that the test results we just discussed were obtained from a short time simulation.

Similar to previous one, another simulation for longer integration time was performed. The integration was performed with both double and extended precision. During each integration run, the sequences of intersections of the orbit with the  $z = 0$  plane was recorded. The relative error between the results recorded from the double and extended precision simulations was calculated and plotted. As the simulation time increased, the relative error increased to an order which was five times larger than the machine precision epsilon. Another simulation, to check the preservation of the Hamiltonian of the R3BP, with long integration time was performed. Theoretically, the Hamiltonian for the R3BP should remain constant for a given orbit, so any drift in the initial and final value of the Hamiltonian after a long integration time can indicate the severity of error propagation in the integrator. The integration was performed with double precision with time of  $10^6$  units. A drift in the initial and final value of the Hamiltonian was observed, however, [30] considered the drift to be meaningless from a statistical point of view because the drift was relatively small compared to the length of the integration. The paper reported that for shorter integration times, the TAYLOR software could provide an integrator that is symplectic but in long term integration, biases could be observed in the Hamiltonian. The biases in the Hamiltonian over long term integration were also observed when extended precision arithmetic was used. The drift in the value of the Hamiltonian is because of truncation error (due to a finite order for the Taylor Series expansion) and round-off errors in the numerical integration process [30].

A comparison of the performance of TSM, as obtained from the use of the TAYLOR software, with other commonly used integrators will be presented in Section 7.8.

## 7.7 PERFORMANCE VERIFICATION OF A NUMERICAL INTEGRATOR

Until this point we have discussed the various strategies available in the literature to numerically integrate a set of ODEs. However, verification and validation of a numerical integrator, i.e. ensuring that the algorithms that have been implemented are correct, is more important than selecting the appropriate numerical integration scheme itself. If the algorithms have not been implemented correctly, then no matter how accurate an integration method is, the results obtained will be wrong which will eventually lead to wrong conclusions. Hence, a method must be adopted to ensure the integrity of the chosen numerical integrator.

For problems in the field of astrodynamics, a suitable method would be to integrate the unperturbed two-body problem, for both short and long integration times. Once the integration has

---

<sup>1</sup>Machine precision epsilon is defined as the distance between 1 and the next larger floating point number

completed, we can transform the Cartesian coordinates at each epoch into the classical orbital elements and verify that they remain conserved over extended periods of integration and for stressful cases such as highly eccentric orbits [52]. [52] also mentions that to verify the performance of an integrator, one can also check that the Jacobi integral (if defined for a system) remains preserved. These methods are not a proof of an integrator's accuracy but they provide effective means to verify the performance of an integrator and ensure that the algorithms have been implemented properly.

## 7.8 CONCLUSION

The research work can be easily subdivided into two main focus areas: one is the simulation of the full two-body problem and the other is the simulation of the restricted three-body problem. For the full two-body problem, we already mentioned that the only way we can avoid a wrong simulation is by not using the general integration methods like Runge-Kutta, multistep or extrapolation. The only way one can perform an integration without violating the geometric characteristics of the two-body problem, such as drift in the attitude matrices from the orthonormal rotation group, is by using the Lie group variational integrator, for which we presented the discretized equations of motion in Lagrangian format. The approach is to simulate the entire two-body problem first using LGVI and create a set of relevant data points consisting of position, velocity, potential, torque, moment etc. values and utilize these when we simulate the three-body problem. When we simulate the three-body problem, we do not require the LGVI since in our case the third body is modeled as a point massless object which will not affect the dynamics of the two-body problem. Thus, there will not be any geometric characteristics to consider when it comes to simulating the orbit of the third particle around the binary system. In this regard, one can say that we can use any one of the standard integration techniques.

To compare the standard numerical integration methods for orbital computation, we will consider that an accuracy of upto 8 digits is required, which means that the position estimation will be correct upto 10 nm, which is adequate when it comes to simulating the orbit of a particle. We will compare the number of function calls that is needed to achieve this accuracy for each integration method type by evaluating the graphical results presented in [37]. The graphs for Runge-Kutta, multistep, and extrapolation methods are presented as follows [37]:

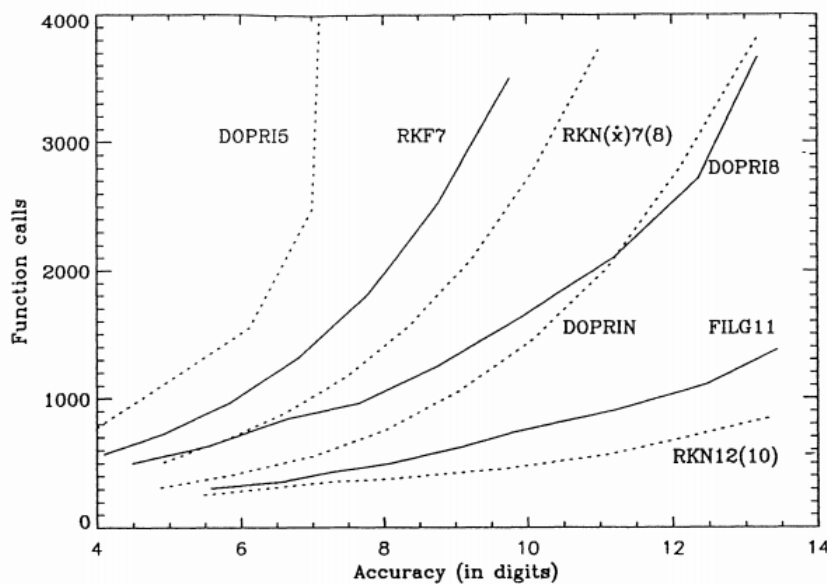


**Figure 7.4:** Function calls versus accuracy for various Runge-Kutta integrator implementations [37].

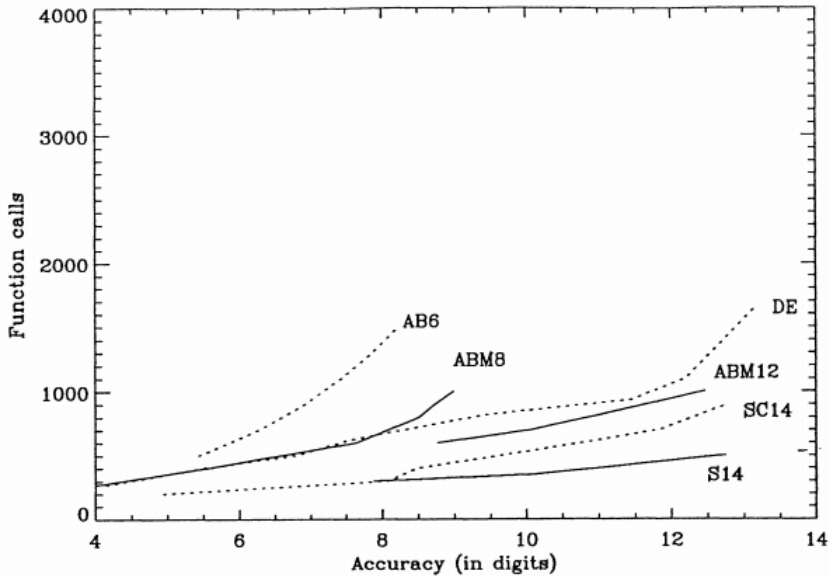


**Figure 7.5:** Function calls versus accuracy for various multistep integrator implementations [37].

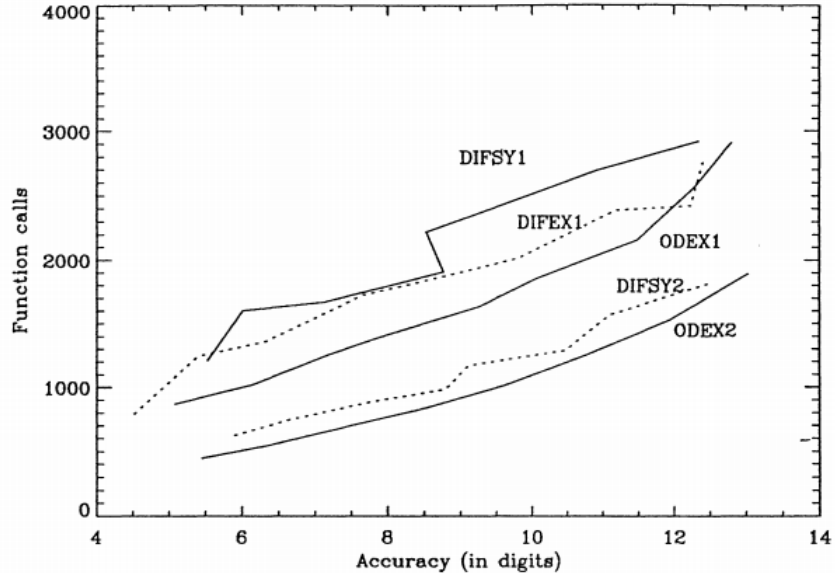


**Figure 7.6:** Function calls versus accuracy for various extrapolation integrator implementations [37].

Starting with the Runge-Kutta methods in Figure 7.4, the methods RKN12(10), FILG11, DOPRIN are all based on Runge-Kutta Nyström methods which as we discussed earlier is a method developed for the case where the acceleration term in the differential equation has no dependency on the velocity, which is not the case for the three-body problem we developed so these methods will not be utilized. The next best solution is the embedded Runge-Kutta method called DOPRI8 which is basically an 8<sup>th</sup>-order method with a 7<sup>th</sup>-order embedded method for accuracy control. For an accuracy of 8 digits, it requires a little over 1000 function calls. The coefficients for this method are readily available and the implementation of this method is the easiest of all.

Next we will consider the multistep methods in Figure 7.5. S14 and SC14 are based on Stoermer-Cowell methods which again work on differential equation forms where the acceleration does not depend on the velocity term, hence these two methods will not be considered. To get the required accuracy of 8 digits, two methods namely DE (which is a variable-stepsize and variable-order mul-

timestep Adams method) and ABM8 (which is an 8<sup>th</sup>-order Adams-Bashforth-Moulton method that utilizes the PECE algorithm) require the same number of function calls i.e. a little less than 1000. From a computational point of view, coding the ABM8 method is much more simple than the DE method since the mathematics behind the former is much easier in comparison to that of a variable-order and stepsize method. Moreover, the coefficients for the ABM8 method are also provided in [36] which would drastically help in coding the algorithm in practice.

Next we will discuss the extrapolation integration methods from Figure 7.6. The methods presented here are very specific but they basically follow the same principles of extrapolation methods that we had discussed earlier. The DIFSY2 method is specially designed for differential equations that do not depend on first-order derivatives and hence this method will not be considered. The same goes for ODEX2. The remaining methods depicted in the graph provide the required accuracy for function calls way over 1000.

Finally we will discuss the TSM for numerical integration. [30] compares the performance of the TSM with, and specifically their implementation, with an explicit Runge-Kutta code of order 8 and an extrapolation method of varying order based on the Gragg-Bulirsh-Stoer algorithm. [30] notes that the TSM and the extrapolation methods are, in general, similar to each other since both can use arbitrarily high orders. [30] did the performance comparison by numerically solving the R3BP, Lorenz problem and the periodically forced pendulum problem. In all the tests, the integrator produced by the TAYLOR software was superior to the other two integrators. The extrapolation method based integrator was comparable to the TSM integrator in its performance, however, the RK integrator performed poorly compared to the former two. Note that the integration time was small in all test cases and [30] did not do the comparison for longer integration times.

From the application point of view, it is more important to produce reliable results rather than being concerned about the time it takes to produce highly accurate results. Of all the methods that we have discussed here, when it comes to accuracy, the extrapolation method and TSM prove to be superior. In particular, the TSM implementation from [30] provides high accuracy and is also faster than its RK and extrapolation counterparts. The TSM from [30] is the easiest to implement since all one has to do is to provide the differential equation in their mathematical form to the software which then automatically produces the code for the integrator. But since this integrator has not been tested for longer integration times, its reliability is questionable. We could use multistep integration methods, however they tend to be highly unstable, especially at higher-orders, unless of course a PECE algorithm is used. The latter is particularly useful for astrodynamics problems which often involve long-periods of perturbations intertwined with short-periods of intense interactions with the main body [52]. Of all, however, the most accurate method, albeit computationally expensive, is the extrapolation method. Since we are more concerned with the accuracy than the speed of integration, extrapolation methods such as the Burlisch-Stoer algorithm offer the most superior performance and hence shall be used for the thesis.



# 8

## MONTE CARLO SIMULATION

### 8.1 INTRODUCTION

Monte Carlo is a simulation technique wherein uncertain inputs to a simulation model are represented in the form of a probability distribution. When we talk about observing the trajectories of multiple particles around a binary system, we want to observe all possible scenarios in which these particles could be lofted from the surface of the asteroid and then analyze the corresponding long or short-term behavior of the particles in orbit. In this regard, Monte Carlo simulations will turn out to be a useful tool. It will be utilized in generating multiple debris particles at the surface of the asteroid by basically generating random initial state vectors (position and velocity) from a reasonable probability distribution for the third body in the three-body problem. These particles will then be propagated in the three-body simulator to record its orbit.

It is assumed that the surface debris is lofted off the surface of the asteroid due to an impact by a spacecraft or its constituent as part of an exploration program. This will result in a crater on the asteroids surface from where the debris shall be lofted. Since we are modeling the asteroids as polyhedrons, we can consider certain multiple adjacent facets on the polyhedron from where we will assume that the debris is lofted from. Thus these facets will enable us to put a boundary on the probability distribution from which we can sample random values for the position components of the initial state vector, thereby ensuring that the initial vector is from within a designated surface area on the asteroid and not elsewhere. For the velocity components, we will follow a similar process but for the first set of simulation the probability distribution shall be bounded between a velocity of 0 and the escape velocity. The second set of simulation could involve increasing the upper bound from the escape velocity by a certain constant factor to observe if the perturbations could play a more significant role in the dynamical environment around the asteroid than the latter's gravitational force itself (this phenomenon will also be analyzed for in the first set of simulations as well), such as bringing back the particle back to the asteroid's surface despite having a higher than escape velocity. Thus in this manner we will be able to simulate the various, if not all, conditions in which a particle can be lofted from the surface. The Monte Carlo simulation will help us in determining the range of all possible outputs along with the likelihood of each occurring.

Now that we have presented a rationale for using Monte Carlo methods, this chapter will further discuss the way in which we can produce a random value generating function from a given probability density function of our choice following which we will discuss how we can sample random values using the generating function.

## 8.2 RANDOM VALUE GENERATING FUNCTION

We need a random value generating function for each component of the initial state vector to run the Monte Carlo simulation. To do that we first need a probability density function  $f(x)$ , then from this we will obtain the distribution function  $F(x)$ . The random value generating function  $G(F(x))$  will then generate the random value as  $x = G(f(x))$  [25].

We will take a general example and explain the whole process of obtaining  $G(F(x))$ . Consider a sinusoidal probability density function, shown in Figure 8.1, as follows [25]:

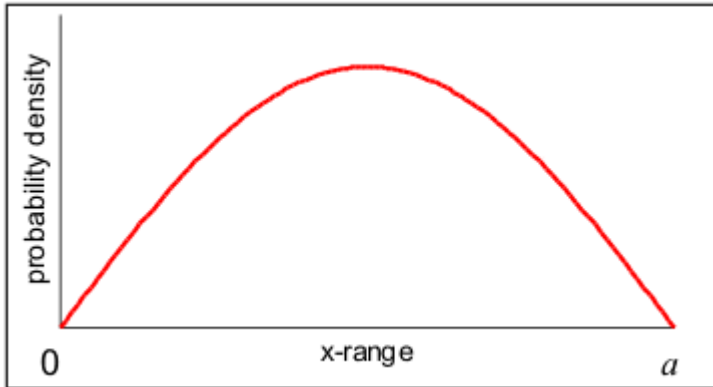


**Figure 8.1:** Sinusoidal probability density function [25].

$$f(x) = b \sin\left(\frac{\pi x}{a}\right) \quad (8.1)$$

where  $a$  and  $b$  are two constants and  $x$  is the random value. From this the cumulative distribution function is obtained as follows [25]:

$$F(x) = \int_0^x b \sin\left(\frac{\pi x}{a}\right) dx = \frac{ab}{\pi} (1 - \cos(\pi x/a)) \quad (8.2)$$

The area under the probability density function must be equal to unity. The user can set the value of the constant  $a$  and then the value of  $b$  can be obtained such that  $F(a) = 1$  [25]:

$$F(a) = 1 = (ab/\pi)(1 - \cos(\pi)) = 2ab/\pi \quad (8.3)$$

Thus from the above expression, the value of  $b$  comes out to be  $b = \pi/2a$ . Then  $F(x)$  becomes [25]:

$$F(x) = 0.5(1 - \cos(\pi x/a)) \quad (8.4)$$

Now we can get the random value generating function from  $G(F(x)) = x$  by rearranging the terms such that [25]:

$$x = (a/\pi) \cos^{-1}(1 - 2F(x)) = G(F(x)) \quad (8.5)$$

Thus by choosing an appropriate probability density function for each component of the initial state vector of the third particle in the three-body problem, we can generate appropriate random values to initiate the simulation.

## 8.3 RANDOM VALUE SAMPLING

Once we have the distribution function and the corresponding generating function, we need a way in which we can efficiently sample the random value. For this purpose, we shall use a sampling technique called the Latin Hypercube sampling. In this method the distribution function is divided into equal  $n$  intervals where  $n$  is the number of iterations we want to perform in the Monte Carlo simulations. A graphical representation of this is given in Figure 8.2 [25]:

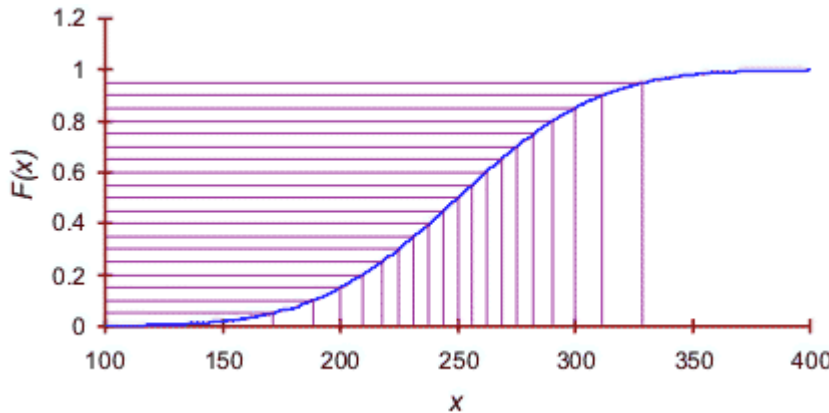


**Figure 8.2:** Equal intervals in Latin Hypercube sampling [25].

The iterations begin by randomly selecting one of the intervals out of the  $n$  intervals. A second random number is then used to determine where within the selected interval would the value of  $F(x)$  would lie. Using this value of  $F(x)$  the random value  $x = G(F(x))$  is obtained. The integration process continues and whatever interval was used earlier is marked so that it is not used again. This avoids repetition of iterations [25].

## 8.4 CONCLUSION

This chapter provided the mathematical basis for the use of Monte Carlo simulation in a generalized manner. In the introduction we also presented the motive for using this simulation technique and how this technique would be applied to generate multiple debris particles at the surface of the asteroid. Another simulation technique which was not discussed in this chapter, called the grid-search or enumerative technique, involves a systematic search through a predefined model space (in our case the model space would contain the initial values for position and velocity of the orbiting particle) and then the evaluation of the dynamical model for each of the grid-searched values [55]. For the astrodynamics problem of a particle orbiting around an asteroid, a grid-search based method will not be practical because the model space or the search space will be very large. On the other hand, the Monte Carlo method is a random search method wherein the search space can be narrowed by defining a probability distribution function from which the model parameters (i.e. the initial conditions) are sampled from [55].

Monte Carlo simulation will be necessary in analyzing all "what-if" situations such as "what if the particle has an initial velocity less than the escape velocity" or "what if the particle is deployed from the pole or the equator of the asteroid" and so on. Once a dynamics simulator is set up, it is very important that we exploit the simulator to assess every possible outcome and to be able to do this, we need the Monte Carlo simulation technique.



# 9

## DYNAMICAL SYSTEMS THEORY

### 9.1 INTRODUCTION

In the three-body problem, an important aspect is the invariant manifolds of the periodic orbits. An invariant manifold is a manifold embedded within a given phase space such that the manifold is invariant under the phase flow i.e. an orbit or solution that starts within an invariant manifold stays within this manifold [59]. From an astrodynamics perspective, invariant manifolds are tube-like structures along which a spacecraft can travel without utilizing any energy [38]. The invariant manifold structures of libration points  $L_1$  and  $L_2$  are important for understanding the motion of a particle in a three-body problem that undergoes resonance hopping. Also of importance are the stable and unstable invariant manifolds associated with the periodic orbits around  $L_1$  and  $L_2$  since they are the phase space channels transporting material between the various realms within the three-body problem. It is the invariant manifold tubes that put limitations on the capture and escape properties of a third particle in motion in the three-body problem. Inside the invariant manifolds tubes, the motion of a particle consists of a set of paths called transit orbits and outside the manifolds, these transit orbits are not possible. The cylindrical tube like shaped unstable and stable manifolds associated with  $L_1$  and  $L_2$  are needed to understand the connections within the phase space [19]. This chapter will provide a brief description on the underlying theory regarding dynamical systems and the invariant manifolds theory in the context of the three-body problem. The general discussion will be based on the (planar) circularly restricted three-body problem, but the concepts can easily be extended to higher fidelity models of the restricted three-body problem.

### 9.2 (PLANAR) CIRCULAR RESTRICTED THREE-BODY PROBLEM

We will consider the motion of a massless particle  $\mathbf{P}$  which is being influenced by the gravitational attraction of two primary bodies with masses  $m_1$  and  $m_2$ . These bodies are moving in a circular orbit around their barycentre or centre of mass. The particle  $\mathbf{P}$  does not affect the motion of the two primary bodies. We define a certain mass parameter for this system as follows [19]:

$$\mu = \frac{m_2}{m_1 + m_2} \quad (9.1)$$

It is assumed that mass  $m_1$  is larger than  $m_2$ . The two primary masses  $m_1$  and  $m_2$  are then rewritten in terms of this mass parameter as follows [19]:

$$\begin{aligned} \mu_1 &= 1 - \mu \\ \mu_2 &= \mu \end{aligned} \quad (9.2)$$

The geometry of the PCRTBP (Planar Circular Restricted Three Body Problem) is defined in a rotating frame where the origin of the frame is centered at the barycentre of the two primaries and

the frame is rotating synchronously with the primary bodies' revolution rate around the barycentre. The geometry is depicted in Figure 9.1 [19].

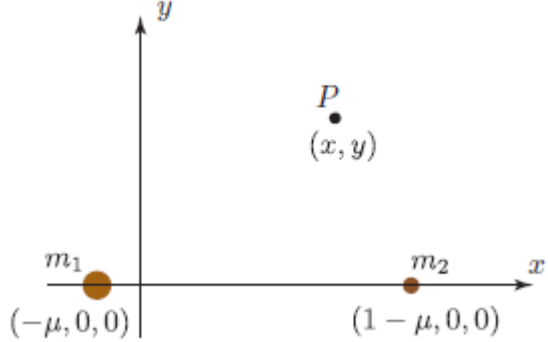


**Figure 9.1:** Geometry of the PCRTBP in rotating frame [19].

The Hamiltonian equations of motion for the general circular restricted three-body problem (which can easily be converted to the PCRTBP by making  $z = \dot{z} = 0$ ) in the rotating frame are given as follows [19]:

$$\begin{aligned}\dot{x} &= p_x + y \\ \dot{y} &= p_y - x \\ \dot{z} &= p_z \\ \dot{p}_x &= p_y - x - U_x \\ \dot{p}_y &= -p_x - y - U_y \\ \dot{p}_z &= -U_z\end{aligned}\tag{9.3}$$

where  $U$  is the gravitational potential and the subscripts denote against which term the partial derivative has been taken. The  $p$  term are the momenta conjugate and are given as follows:

$$\begin{aligned}p_x &= \dot{x} - y \\ p_y &= \dot{y} + x \\ p_z &= \dot{z}\end{aligned}\tag{9.4}$$

The corresponding energy integral of motion is also given as [19]:

$$E(x, y, z, \dot{x}, \dot{y}, \dot{z}) = \frac{1}{2}(\dot{x}^2 + \dot{y}^2 + \dot{z}^2) + U(x, y, z)\tag{9.5}$$

This was a brief introduction to the (planar) circular restricted three-body problem. The equations of motion and energy integral of motion will be used in the following sections to understand the concepts of dynamical systems theory in astrodynamics.

### 9.3 ENERGY MANIFOLD, HILL'S REGION, AND ZERO VELOCITY CURVES

Considering the PCRTBP, we have a four-dimensional phase space namely two position coordinates  $x, y$  and two velocity coordinates  $\dot{x}$  and  $\dot{y}$ . For a real value  $e$ , the equation  $E_{kep} = e$  where  $E_{kep}$  is called the Keplerian energy, denotes a three-dimensional set in the four-dimensional phase space. This three-dimensional set is termed the energy surface corresponding to the energy  $e$  or simply an energy manifold [19].

Let  $\mathcal{M}$  denote the energy manifold obtained by equating energy integral given by Equation (9.5) (take  $z = \dot{z} = 0$ ) to a constant real value  $e$  [19]:

$$\mathcal{M}(\mu, e) = \{(x, y, \dot{x}, \dot{y}) | E(x, y, \dot{x}, \dot{y}) = e\}\tag{9.6}$$

For a given value of  $\mu$  and  $e$ , the energy manifold term  $\mathcal{M}$  can be considered as a three-dimensional surface within the four-dimensional phase space. The projection of the energy manifold onto the  $xy$  plane i.e. the position space of the rotating frame of reference, gives the region in which a particle with energy  $e$  can undergo motion under the influence of the gravitational pull of the two primary masses  $m_1$  and  $m_2$ . The regions of allowable motion are called *Hill's Region*. This projection is given as follows [19]:

$$M(\mu, e) = \{(x, y) | U(x, y) \leq e\} \quad (9.7)$$

The boundary of the Hill region,  $M(\mu, e)$ , places bounds on the motion of the third particle and is called the zero velocity curve. The latter are a locus of points in the  $xy$ -plane where the kinetic energy of the particle vanishes i.e. the velocity is zero. The particle can have a non-zero velocity only on the side of this curve for which the particle has a positive kinetic energy. The other side of the curve is where the particle has negative energy and this is the region where motion is obviously not possible and is called the forbidden realm [19].

For a given mass parameter value, there are five basic configurations for the Hill's region each corresponding to the five intervals of the energy value  $e$  in Equation (9.6). Four of the cases are depicted in Figure 9.2. The fifth case is not depicted here because it is graphically not relevant since in the fifth case, the particle is not subjected to any forbidden realm and can freely move about anywhere around the two primary bodies.

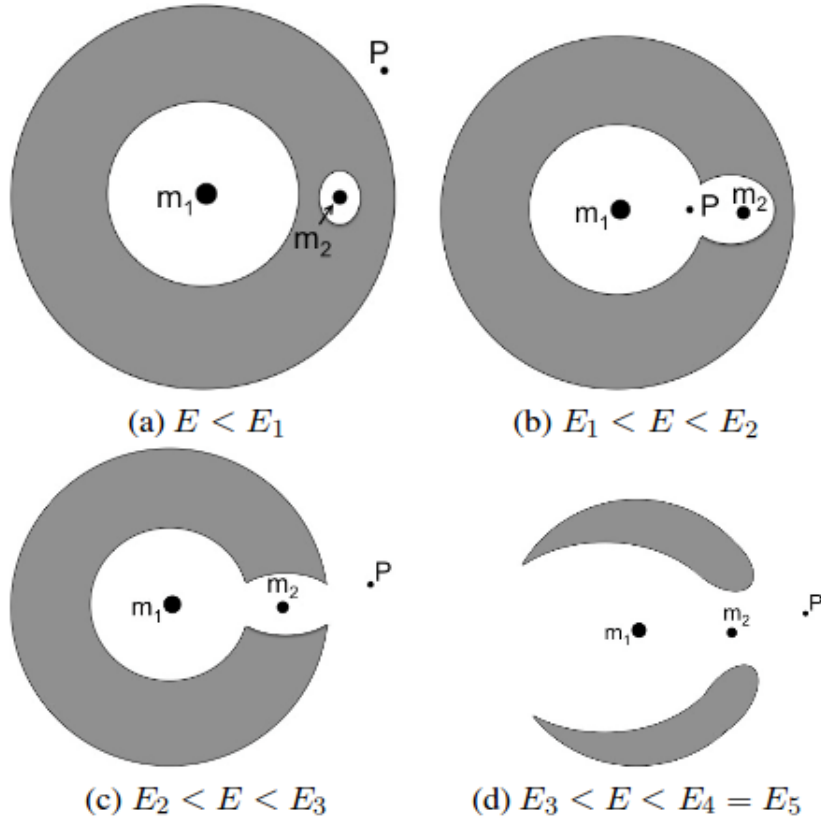


**Figure 9.2:** Zero Velocity Curves for four cases of different energy values. The white regions in each case corresponds to the region accessible by the third particle for motion around the two primary masses. The shaded region are inaccessible by the particle and is called the forbidden realm. The outermost region beyond the shaded area, called exterior realm is accessible by particle. The fifth configuration, not shown here, is where the particle is not subjected to any forbidden realms and can freely move in the entire plane [38].

We will discuss the five cases of energy values now and how they affect the motion of the particle

in the PCRTBP [19]:

- $E < E_1$ : If the energy of the particle is less than the critical value  $E_1$  then the particle cannot move from the accessible realm around  $m_1$  to the accessible realm around  $m_2$  and vice-versa.
- $E_1 < E < E_2$ : For the particle energy just above the critical energy  $E_1$ , a small opening or a "neck" forms between the accessible realms of  $m_1$  and  $m_2$  from the previous case. The  $L_1$  point is in this neck opening. The particle can thus move through this neck and this transport is controlled by the invariant manifold associated with the  $L_1$  point.
- $E_2 < E < E_3$ : If the energy of the particle is just above the critical value  $E_2$  then another neck opens up connecting the realm around  $m_2$  to the exterior realm. This neck also corresponds to the  $L_2$  point. The particle can now move between the internal realms around the primary masses and also to the exterior realm through the two necks as seen in case 3 in Figure 9.2.
- $E_3 < E < E_4 = E_5$ : The particle in this energy range results in opening up the neck region between the  $m_1$  realm and the exterior realm and this neck region corresponds to the  $L_3$  libration point.
- $E_4 = E_5 < E$ : For particle in this energy interval, the forbidden realm vanishes and the particle can move everywhere in the position space.

Each critical value of energy as discussed above,  $E_i$ ,  $i = 1\dots 4$  corresponds to the corresponding libration points  $L_i$ ,  $i = 1\dots 4$  [19]. In the next section we will look at how the libration points are obtained for a given system.

## 9.4 LIBRATION POINTS

We will still consider the PCRTBP. The equations of motion for this problem are given as:

$$\begin{aligned}\dot{x} &= v_x \\ \dot{y} &= v_y \\ \dot{v}_x &= 2v_y - U_x \\ \dot{v}_y &= -2v_x - U_y\end{aligned}\tag{9.8}$$

To find the libration points, the right-hand sides of each expression in Equation (9.8) is set to zero. In doing so we get two equations which have to solved to obtain the equilibrium points namely  $U_x = 0$  and  $U_y = 0$ . The libration points are also called equilibrium points and the equilibria in the four-dimensional phase space is of the form  $(x_e, y_e, 0, 0)$  where the critical points of the potential function are given as  $(x_e, y_e)$ . In the PCRTBP there are 5 equilibrium or libration points out of which the first three,  $L_1$ ,  $L_2$ , and  $L_3$  lie on the  $x$ -axis and are collinear.  $L_4$  and  $L_5$  are not collinear and are located in the  $xy$ -plane such that  $y \neq 0$ . A few definitions might come handy. Assume  $r_1$  is the distance from the primary  $m_1$  to the third particle and similarly  $r_2$  is the distance from the primary  $m_2$  to the particle. These terms are obtained as follows [19]:

$$\begin{aligned}r_1^2 &= (x + \mu_2)^2 + y^2 + z^2 \\ r_2^2 &= (x - \mu_1)^2 + y^2 + z^2\end{aligned}\tag{9.9}$$

Of course for the planar problem the  $z$ -term in Equation (9.9) would become 0. The potential term is given as [19]:

$$\begin{aligned}U(x, y) &= -\frac{1}{2}(x^2 + y^2) - \frac{\mu_1}{r_1} - \frac{\mu_2}{r_2} - \frac{1}{2}\mu_1\mu_2 \\ &= -\frac{1}{2}(\mu_1 r_1^2 + \mu_2 r_2^2) - \frac{\mu_1}{r_1} - \frac{\mu_2}{r_2}\end{aligned}\tag{9.10}$$

We will start with the process to obtain the non-collinear libration points. After rearranging terms in Equation (9.9) the following expression is obtained [19]:

$$x^2 + y^2 = (1 - \mu)r_1^2 + \mu r_2^2 - \mu(1 - \mu) \quad (9.11)$$

Substituting this into Equation (9.10) we get:

$$-U(r_1, r_2) = \frac{1}{2}(1 - \mu)r_1^2 + \frac{1}{2}\mu r_2^2 + \frac{1 - \mu}{r_1} + \frac{\mu}{r_2} \quad (9.12)$$

The partial derivatives of  $U$  equated to 0 will give the libration points 4 and 5:

$$\begin{aligned} U_x &= U_{r_1} \frac{\partial r_1}{\partial x} + U_{r_2} \frac{\partial r_2}{\partial x} = 0 \\ U_y &= U_{r_1} \frac{\partial r_1}{\partial y} + U_{r_2} \frac{\partial r_2}{\partial y} = 0 \end{aligned} \quad (9.13)$$

solving which leads to:

$$\begin{aligned} 0 &= -U_{r_1} = \mu r_2 - \frac{\mu}{r_2^2} \\ 0 &= -U_{r_2} = (1 - \mu)r_1 - \frac{1 - \mu}{r_2^2} \end{aligned} \quad (9.14)$$

Solving which we get the unique solution  $r_1 = r_2 = 1$  meaning that the  $L_4$  and  $L_5$  libration points lie at equal distances from the two primary masses.  $L_4$  lies in the positive  $y$  segment and  $L_5$  lies in the negative. Now we will calculate the collinear equilibrium points. In this case  $y = 0$  and so the potential function would be rewritten as [19]:

$$U(x, 0) = -\frac{1}{2}x^2 - \frac{1 - \mu}{|x + \mu|} - \frac{\mu}{|x - 1 + \mu|} \quad (9.15)$$

We have three intervals along the  $x$ -axis as can be seen in Figure 9.1 namely  $(-\infty, -\mu)$ ,  $(-\mu, 1 - \mu)$ , and  $(1 - \mu, \infty)$ . Note that these intervals are only for the  $x$ -coordinate and the second term in each bracket does not correspond to the  $y$ -coordinate. For all these intervals, the potential function tends to  $-\infty$ . Also, the second partial derivative of the potential function from Equation (9.15) is always negative meaning that the potential function is concave in all three intervals. Thus each interval has precisely one critical point. These points are the three remaining libration points. Calculating the  $x$  coordinate of the collinear libration points requires us to finding the maximum (due to concavity) of the potential function. The distance from  $L_1$  and  $L_2$  to the mass  $m_2$  is given by the following equation [19]:

$$\gamma^5 \mp (3 - \mu)\gamma^4 + (3 - 2\mu)\gamma^3 - \mu\gamma^2 \pm 2\mu\gamma - \mu = 0 \quad (9.16)$$

A similar equation can be found for the distance of  $L_3$  to the mass  $m_1$ . The solution to the distance equation is obtained by using a series expansion method and are given as [19]:

$$\begin{aligned} \gamma_1 &= r_h \left(1 - \frac{1}{3}r_h - \frac{1}{9}r_h^2 + \dots\right) \\ \gamma_2 &= r_h \left(1 + \frac{1}{3}r_h - \frac{1}{9}r_h^2 + \dots\right) \end{aligned} \quad (9.17)$$

where  $r_h$  is called the Hill radius and is defined by the equation  $r_h = \frac{\mu^{1/3}}{3}$ . Using the Newton-Raphson method and taking the Hill radius as initial value, the solutions  $\gamma_1$  and  $\gamma_2$  to Equation (9.16) can be found. This is how the libration points can be found in the case of the PCRTBP and a similar approach can be applied for higher-fidelity models.

## 9.5 INVARIANT MANIFOLDS OF A PERIODIC ORBIT

To compute the invariant manifolds of a periodic orbit, one needs two mathematical tools namely the monodromy matrix and the Poincaré maps. These tools will also be helpful in assessing the stability of periodic orbits.

### 9.5.1 MONODROMY MATRIX

We will consider an autonomous equation of the form  $\dot{x} = f(x)$  with  $x(0) = x_0$ . The periodic solution for this is given as  $x(t)$  with a period of  $T$ . Now a trajectory, or solution, that starts at a perturbed initial state vector i.e.  $x_0 + \delta x_0$  will after one full period experience a displacement by [19]:

$$\delta x(T) = \phi(T; x_0 + \delta x_0) - \phi(T; x_0) \quad (9.18)$$

which in first order is written as:

$$\delta x(T) = \phi(T)\delta x_0 \quad (9.19)$$

where  $\phi(T)$  is the state transition matrix for one time period  $T$ . This is the monodromy matrix which determines whether a perturbation in the initial state vector tends to grow or decay, and is defined as [19]:

$$M \equiv \phi(T) = \frac{\partial \phi(T; x_0)}{\partial x_0} \quad (9.20)$$

Some important mathematical properties relating to the monodromy matrix which will be helpful are stated as follows [19]:

- Floquet Theorem:  $\phi(t) = P(t)e^{Rt}$  where  $P(t)$  is periodic with a period of  $T$  and  $R$  is a constant matrix
- $\phi(kT) = M^k$
- $M$  has an eigenvalue equal to 1 with an eigenvector that is tangent to the periodic orbit at  $x_0$  and this eigenvector is given as  $\dot{x}(0) = f(x_0)$

The eigenvalues  $\lambda$  of the monodromy matrix are called Floquet or characteristic multipliers and each number  $\sigma$  related to eigenvalue as  $\lambda = e^{\sigma T}$  is called the Floquet or characteristic exponent. These terms are used for studying the local stability of a periodic solution.

### 9.5.2 POINCARÉ MAPS

These maps are useful to study the flow near a periodic orbit. Let's define a co-dimension 1 surface of section as  $\Sigma$  such that all trajectories that cross it in a neighborhood of  $q \in \Sigma$  satisfy two requirements namely: the trajectories intersect the surface of section transversely and that they cross the surface in the same direction [19]. If  $T_\Sigma(q)$ , where  $q \in \Sigma$ , is the time taken for a trajectory  $\phi(t; q)$  to return to  $\Sigma$  for the first time, then the Poincaré map is given as [19]:

$$P(q) \equiv \phi(T_\Sigma(q); q) \quad (9.21)$$

So in plain words, a Poincaré map is created by allowing trajectories to intersect with the Poincaré section. This is shown pictorially in Figure 9.3.

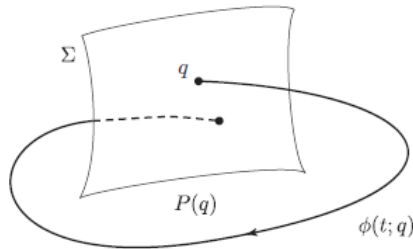


**Figure 9.3:** Poincaré map generated by trajectories intersecting the Poincaré section [19].

A periodic trajectory would then be the one which intersects the section at the same fixed point  $q$  where  $q = \phi(T; q)$ . The stability of a periodic orbit is obtained by checking whether the point  $q$  is an attractor or repellor in the map. To do this we linearize the Poincaré map around the fixed point  $q$  as follows [19]:

$$\frac{\partial P(q)}{\partial q} = \frac{\partial \phi(T; q)}{\partial q} \quad (9.22)$$

The eigenvalues of this linearization are then calculated and if the moduli of all eigenvalues is smaller than 1 then the point  $q$  is stable and if the modulus of any one eigenvalue is larger than 1 then  $q$  is unstable. Similarly in case of the monodromy matrix  $M$ , apart from the one eigenvalue which is equal to one, if the modulus of all remaining eigenvalues of  $M$  is less than one then the periodic orbit is stable otherwise even if the modulus of one of the eigenvalue is greater than one then the orbit is unstable.

### 9.5.3 COMPUTATION OF INVARIANT MANIFOLDS

Given the monodromy matrix  $M = \phi(T)$ , its eigenvalues are first calculated. The eigenvectors associated with the modulus of eigenvalues greater than 1 are in the unstable direction whereas the eigenvectors associated with modulus of eigenvalues less than 1 are in the stable direction. Let  $Y^s(X_0)$  denote the normalized stable eigenvector and  $Y^u(X_0)$  denote the normalized unstable eigenvector. These are used to get the approximate manifolds as [19]:

$$\begin{aligned} X^s(X_0) &= X_0 + \epsilon Y^s(X_0) \\ X^u(X_0) &= X_0 + \epsilon Y^u(X_0) \end{aligned} \quad (9.23)$$

where  $X^s$  and  $X^u$  are the initial guesses for the stable and unstable manifolds respectively at  $X_0$  along the periodic orbit. The term  $\epsilon$  denotes a small displacement from  $X_0$ . By numerically integrating the unstable eigenvector forward in time using both  $\pm\epsilon$  we can generate trajectories shadowing the two branches of the unstable manifold and in a similar way, by integrating the stable eigenvector backwards in time we can generate trajectories shadowing the two branches of the stable manifold. So this is how the invariant manifold for the periodic orbit are obtained [19].

## 9.6 CONCLUSION

This was a brief chapter describing various elements that are utilized when it comes to applying the dynamical systems theory to astrodynamics problems. Many books have been written in this regard and for some readers this chapter might seem obscure but the purpose of including it in this literature study report was to understand the basics of dynamical systems theory and its application to celestial mechanics.



# 10

## CONCLUSIONS

This literature study report focused on a thorough study of the dynamics of a binary asteroid system and of a spacecraft/particle orbiter around the binary asteroids. The study of a binary asteroid system was inspired by the joint mission between ESA and NASA, called AIDA, which involves sending two spacecrafsts to the binary asteroid system Didymos. This report provides an extensive coverage of the various models and methods available to simulate the gravitational potential of an asteroid in general. After a careful evaluation of all the methods covered in this report, the polyhedron model was chosen to simulate the gravity field of an asteroid as it offered higher accuracy and a more realistic representation of an irregularly shaped asteroid. A study of some basic perturbation models, such as third-body effects and Solar Radiation Pressure, was also conducted. In general, these perturbations are accounted for in the motion of an orbiter around an asteroid. We calculated the first-order values for the perturbing accelerations from the gravitational acceleration of the Sun and Jupiter, the Solar Radiation Pressure and compared it to the acceleration due to gravity of a reference asteroid 433 Eros. These perturbing accelerations were calculated for a single regolith particle. The first order perturbing accelerations were calculated to assess their relative significance. We found that the perturbing acceleration due to the third-body effect of the Sun and the Solar Radiation Pressure was of the same order of magnitude as the acceleration due to gravity of Eros. Hence, it was concluded that the perturbations due to the third-body effect of the Sun and Solar Radiation Pressure can not be ignored in the dynamics simulator of an orbiting particle or spacecraft around an asteroid. The equations of motion for the full two-body problem, i.e. the relative motion of two non-point mass asteroids around each other, was studied and presented in the report. The equations of motion were presented for different configurations of the binary system, such as sphere-ellipsoid, ellipsoid-ellipsoid and polyhedron-polyhedron. The equations of motion for a massless third-body orbiting around a binary asteroid system were also studied for the same three binary configurations mentioned earlier. To simulate the motion of a spacecraft or a particle around an asteroid, the differential equations of motion have to be integrated. The structure of these equations is such that it is difficult to integrate them analytically and so a numerical integrator is used instead. This report provides an extensive coverage on the various numerical integration schemes available in literature and compares their performance with one another. Every scheme has its own advantages and disadvantages and as of now, none are universal. For our application, which involves long simulation times, the extrapolation method is the most suitable scheme for numerical integration. This literature study report also presented a brief chapter on the Monte Carlo simulation technique; a method which is needed to observe the motion of several regolith particles, each with a different set of initial conditions, around an asteroid at once. The report concludes by providing a rudimentary introduction to the Dynamical Systems Theory and its role in characterizing orbital motion in general.

It is emphasized again that the literature study report began with a focus on the motion of a spacecraft around a binary asteroid system, but later on the focus was shifted to the study of regolith around an asteroid. The tentative research questions for the latter are presented in Chapter 1. The final research questions, along with the research timeline and corresponding work-packages will be presented in the thesis report that follows.

# BIBLIOGRAPHY

- [1] Barrio, Roberto et al. "Breaking the limits: the Taylor series method". In: *Applied mathematics and computation* 217.20 (2011), pp. 7940–7954.
- [2] Beshore, E. et al. "The OSIRIS-REx Asteroid Sample Return Mission". In: *39th COSPAR Scientific Assembly*. Vol. 39. 2012, p. 154. URL: <http://ntrs.nasa.gov/archive/nasa/casi.ntrs.nasa.gov/20150000808.pdf>.
- [3] Bottke, W.F. *Asteroids III*. University of Arizona Press, 2002.
- [4] Campins, H. et al. "The Origin of Asteroid 162173 (1999 JU3)". In: *The Astronomical Journal* 146.2 (2013), p. 26. URL: <http://stacks.iop.org/1538-3881/146/i=2/a=26>.
- [5] Chappaz, L. and Howell, K. "Bounded Orbits near Binary Systems Comprised of Small Irregular Bodies". In: *AIAA/AAS Astrodynamics Specialist Conference*. 2014. URL: <http://arc.aiaa.org/doi/pdf/10.2514/6.2014-4153>.
- [6] Cheng, A.F. et al. "Asteroid Impact and Deflection Assessment mission". In: *Acta Astronautica* 115 (2015), pp. 262 –269. ISSN: 0094-5765. DOI: <http://dx.doi.org/10.1016/j.actaastro.2015.05.021>. URL: <http://www.sciencedirect.com/science/article/pii/S0094576515002040>.
- [7] Dechambre, D.J.P. "Computation of ellipsoidal gravity field harmonics for small solar system bodies". MA thesis. 2000. URL: [http://ccar.colorado.edu/scheeres/scheeres/assets/Theeses%20and%20Abstracts/dechambre\\_thesis.pdf](http://ccar.colorado.edu/scheeres/scheeres/assets/Theeses%20and%20Abstracts/dechambre_thesis.pdf).
- [8] Dietze, C et al. "Landing and mobility concept for the small asteroid lander MASCOT on asteroid 1999 JU3". In: *61st International Astronautical Congress*. 2010, pp. 1–13.
- [9] Dunham, D.W. et al. "Recovery of NEAR's Mission to Eros". In: *Acta Astronautica* 47.2 (2000), pp. 503–512. URL: <http://www.sciencedirect.com/science/article/pii/S0094576500000898>.
- [10] ESA Science, ESA. *Marcopolo-R*. 2015. URL: <http://sci.esa.int/marcopolo-r/>. [Online Access: 11-09-2015].
- [11] Fahnstock, E.G. "The full two-body-problem: Simulation, analysis, and application to the dynamics, characteristics, and evolution of binary asteroid systems". PhD thesis. 2009. URL: [http://deepblue.lib.umich.edu/bitstream/handle/2027.42/62378/efahnest\\_1.pdf?sequence=1&isAllowed=y](http://deepblue.lib.umich.edu/bitstream/handle/2027.42/62378/efahnest_1.pdf?sequence=1&isAllowed=y).
- [12] Fahnstock, E.G. and Scheeres, D.J. "Simulation of the full two rigid body problem using polyhedral mutual potential and potential derivatives approach". In: *Celestial Mechanics and Dynamical Astronomy* 96.3-4 (2006), pp. 317–339.
- [13] Fahnstock, Eugene G et al. "Polyhedral potential and variational integrator computation of the full two body problem". In: *Proc. AIAA/AAS Astrodynamics Specialist Conf., AIAA-2006-6289*. 2006.
- [14] Feagin, T. "A tenth-order Runge-Kutta method with error estimate". In: *Proceedings of the IAENG Conf. on Scientific Computing*. 2007.
- [15] Ferri, Paolo. "Mission operations for the new Rosetta". In: *Acta Astronautica* 58.2 (2006), pp. 105 –111. ISSN: 0094-5765. DOI: <http://dx.doi.org/10.1016/j.actaastro.2005.06.003>. URL: <http://www.sciencedirect.com/science/article/pii/S0094576505002316>.

- [16] Geissler, Paul et al. "Erosion and ejecta reaccretion on 243 Ida and its moon". In: *Icarus* 120.1 (1996), pp. 140–157.
- [17] Geissler, Pl et al. "Erosion and ejecta reaccretion on 243 Ida and its moon". In: *Icarus* 120.1 (1996), pp. 140–157.
- [18] Glassmeier, K-H. et al. "The Rosetta mission: flying towards the origin of the solar system". In: *Space Science Reviews* 128.1-4 (2007), pp. 1–21. DOI: 10.1007/s11214-006-9140-8. URL: <http://link.springer.com/article/10.1007/s11214-006-9140-8>.
- [19] Gómez, G et al. *Invariant manifolds, the spatial three-body problem and space mission design*. 109. American Astronautical Society, 2001.
- [20] Han, D. "Orbit Transfers for Dawn's Vesta Operations: Navigation and Mission Design Experience". In: *Proceedings 23 rd International Symposium on Space Flight Dynamics, Pasadena, CA, USA*. 2012. URL: [http://issfd.org/ISSFD\\_2012/ISSFD23\\_IN2\\_4.pdf](http://issfd.org/ISSFD_2012/ISSFD23_IN2_4.pdf).
- [21] Hechler, M. "{ROSETTA} mission design". In: *Advances in Space Research* 19.1 (1997). Proceedings of the E1.1, B1.5, and C2.4 Symposia of {COSPAR} Scientific Commissions E, B and C, pp. 127–136. ISSN: 0273-1177. DOI: [http://dx.doi.org/10.1016/S0273-1177\(96\)00125-1](http://dx.doi.org/10.1016/S0273-1177(96)00125-1). URL: <http://www.sciencedirect.com/science/article/pii/S0273117796001251>.
- [22] Helfrich, CE et al. "Near Earth Asteroid Rendezvous (NEAR) Revised Eros Orbit Phase Trajectory Design". In: *AAS/AIAA Astrodynamics Specialist Conference, AAS Paper*. 1999, pp. 99–464. URL: <http://ntrs.nasa.gov/archive/nasa/casi.ntrs.nasa.gov/20000057504.pdf>.
- [23] Hu, Xuanyu. "Comparison of Ellipsoidal and Spherical Harmonics for Gravitational Field Modeling of Non-spherical Bodies". PhD thesis. The Ohio State University, 2012.
- [24] Hull, T. E. et al. "Comparing Numerical Methods for Ordinary Differential Equations". In: *SIAM Journal on Numerical Analysis* 9.4 (1972), pp. 603–637. ISSN: 00361429. URL: <http://www.jstor.org/stable/2156215>.
- [25] *Introduction To Monte Carlo Simulation*. Accessed 1 December 2015. URL: [http://www.epixalytics.com/modelassist/AtRisk/Model\\_Assist.htm](http://www.epixanalytics.com/modelassist/AtRisk/Model_Assist.htm).
- [26] *Jet Propulsion Laboratory, Solar System dynamics, Asteroids*. Accessed 1 July 2016. URL: <http://ssd.jpl.nasa.gov/?asteroids>.
- [27] *Jet Propulsion Laboratory, Solar System Dynamics, Astrodynamical Constants*. Accessed 14 July 2016. URL: <http://ssd.jpl.nasa.gov/?constants>.
- [28] *Jet Propulsion Laboratory, Solar System Dynamics, Small-Body Database Browser*. Accessed 14 July 2016. URL: <http://ssd.jpl.nasa.gov/sbdb.cgi?sstr=433>.
- [29] *Jet Propulsion Laboratory, Why Study Asteroids?* Accessed 1 July 2016. URL: [http://ssd.jpl.nasa.gov/?why\\_asteroids](http://ssd.jpl.nasa.gov/?why_asteroids).
- [30] Jorba, Àngel and Zou, Maorong. "A software package for the numerical integration of ODEs by means of high-order Taylor methods". In: *Experimental Mathematics* 14.1 (2005), pp. 99–117.
- [31] Kaula, W.M. *Theory of satellite geodesy: applications of satellites to geodesy*. Courier Corporation, 2000.
- [32] Lee, Taeyoung, Leok, Melvin, and McClamroch, N Harris. "Lie group variational integrators for the full body problem". In: *Computer Methods in Applied Mechanics and Engineering* 196.29 (2007), pp. 2907–2924.
- [33] Maciejewski, A.J. "Reduction, relative equilibria and potential in the two rigid bodies problem". In: *Celestial Mechanics and Dynamical Astronomy* 63.1 (1995), pp. 1–28. ISSN: 0923-2958. DOI: 10.1007/BF00691912. URL: <http://dx.doi.org/10.1007/BF00691912>.

- [34] Marchis, F et al. "Multiple asteroid systems: Dimensions and thermal properties from Spitzer Space Telescope and ground-based observations". In: *Icarus* 221.2 (2012), pp. 1130–1161.
- [35] Margot, Jean-Luc et al. "Asteroid systems: binaries, triples, and pairs". In: *Asteroids IV. University Arizona Press, Tucson* (2015), pp. 355–374.
- [36] Montenbruck, O. and Gill, E. *Satellite orbits: models, methods and applications*. Springer Science & Business Media, 2005.
- [37] Montenbruck, Oliver. "Numerical integration methods for orbital motion". In: *Celestial Mechanics and Dynamical Astronomy* 53.1 (1992), pp. 59–69.
- [38] Moore, Ashley. "Two Approaches Utilizing Invariant Manifolds To Design Trajectories For DMO Optimization". In: *Geometric Mechanics Project Archives, California Institute of Technology, Pasadena, CA* (2009).
- [39] Muñoz, P. et al. "Preparations and Strategy for Navigation during Rosetta Comet Phase". In: *Proceedings 23rd International Symposium on Space Flight Dynamics-23rd ISSFD, Pasadena, USA*. 2012. URL: [http://issfd.org/ISSFD\\_2012/ISSFD23\\_IN2\\_2.pdf](http://issfd.org/ISSFD_2012/ISSFD23_IN2_2.pdf).
- [40] NASA, *Planetary Fact Sheet*. Accessed 14 July 2016. URL: <http://nssdc.gsfc.nasa.gov/planetary/factsheet/jupiterfact.html>.
- [41] National Space Science Data Centre, NASA. *Dawn*. 2014. URL: <http://nssdc.gsfc.nasa.gov/nmc/spacecraftDisplay.do?id=2007-043A>. [Online Access: 11-09-2015].
- [42] National Space Science Data Centre, NASA. *Hayabusa 2*. 2014. URL: <http://nssdc.gsfc.nasa.gov/nmc/spacecraftDisplay.do?id=2014-076A>. [Online Access: 10-09-2015].
- [43] Panou, G. "The gravity field due to a homogeneous triaxial ellipsoid in generalized coordinates". In: *Studia Geophysica et Geodaetica* 58.4 (2014), pp. 609–625.
- [44] Pacher, D.W. "Low-thrust orbit transfer design for DAWN operations at VESTA". In: *Spaceflight Mechanics* 140 (2011). URL: <http://hdl.handle.net/2014/41932>.
- [45] Polanskey, C. A. et al. "Architecting the Dawn Ceres science plan". In: *Space Operations, Pasadena, CA* (2014). URL: <http://arc.aiaa.org/doi/pdf/10.2514/6.2014-1720>.
- [46] Rayman, M. *Dawn Journal*. 2014. URL: <http://dawnblog.jpl.nasa.gov/2014/02/28/dawn-journal-february-28-2014/>. [Online Access: 13-09-2015].
- [47] Rayman, M. *Dawn Journal*. 2014. URL: <http://dawnblog.jpl.nasa.gov/2014/04/30/dawn-journal-april-30-2/>. [Online Access: 15-09-2015].
- [48] Rayman, M.D. et al. "Dawn: A mission in development for exploration of main belt asteroids Vesta and Ceres". In: *Acta Astronautica* 58.11 (2006), pp. 605–616. ISSN: 0094-5765. DOI: <http://dx.doi.org/10.1016/j.actaastro.2006.01.014>. URL: <http://www.sciencedirect.com/science/article/pii/S0094576506000671>.
- [49] Romain, G. and Jean-Pierre, B. "Ellipsoidal Harmonic expansions of the gravitational potential: Theory and application". English. In: *Celestial Mechanics and Dynamical Astronomy* 79.4 (2001), pp. 235–275. ISSN: 0923-2958. DOI: [10.1023/A:1017555515763](https://doi.org/10.1023/A:1017555515763). URL: <http://dx.doi.org/10.1023/A%3A1017555515763>.
- [50] Scheeres, D. "Orbital Mechanics About Small Asteroids". In: *Advances in Astronautical Sciences* 134 (2009), pp. 1795–1812. URL: [http://issfd.org/ISSFD\\_2007/21-2.pdf](http://issfd.org/ISSFD_2007/21-2.pdf).
- [51] Scheeres, Daniel Jay. "Orbit mechanics about asteroids and comets". In: *Journal of Guidance, Control, and Dynamics* (2012).
- [52] Scheeres, D.J. *Orbital Motion in Strongly Perturbed Environments: Applications to Asteroid, Comet and Planetary Satellite Orbiters*. *Astronautical Engineering*. Springer, 2012.

- [53] Scheeres, DJ. "Solar radiation pressure and transient flows on asteroid surfaces". In: *36th Annual Lunar and Planetary Science Conference*. Vol. 36. 2005.
- [54] Scheeres, D.J. and Augenstein, S. "Spacecraft motion about binary asteroids". In: *Advances in the Astronautical Sciences* 116 (2004), pp. 1–20.
- [55] "Chapter 3 Monte carlo methods". In: *Global Optimization Methods in Geophysical Inversion*. Ed. by Sen, Mrinal and Stoffa, Paul L. Vol. 4. Advances in Exploration Geophysics. Elsevier, 1995, pp. 67 –77. DOI: [http://dx.doi.org/10.1016/S0921-9366\(06\)80004-6](http://dx.doi.org/10.1016/S0921-9366(06)80004-6).
- [56] Sucarrat, E.H. "The full problem of two and three bodies: application to asteroids and binaries". PhD thesis. University of Surrey, 2012. URL: <http://epubs.surrey.ac.uk/797900/>.
- [57] Tsuda, Y. et al. "System design of the Hayabusa 2—Asteroid sample return mission to 1999 {JU3}". In: *Acta Astronautica* 91 (2013), pp. 356 –362. ISSN: 0094-5765. DOI: <http://dx.doi.org/10.1016/j.actaastro.2013.06.028>. URL: <http://www.sciencedirect.com/science/article/pii/S009457651300218X>.
- [58] Van Wal, S. "The ballistic deployment of asteroid landers". MA thesis. 2015. URL: <http://repository.tudelft.nl/view/ir/uuid:20f07d7e-3d2d-498a-898a-e165affa6c12/>.
- [59] Verhulst, Ferdinand. *Nonlinear differential equations and dynamical systems*. Springer Science & Business Media, 2006.
- [60] Wakker, K.F. *Fundamentals of Astrodynamics*. TU Delft Library, 2015. ISBN: 9789461864192. URL: <http://repository.tudelft.nl/view/ir/uuid%3A3fc91471-8e47-4215-af43-718740e6694e/>.
- [61] Werner, R.A. and Scheeres, D.J. "Exterior gravitation of a polyhedron derived and compared with harmonic and mascon gravitation representations of asteroid 4769 Castalia". In: *Celestial Mechanics and Dynamical Astronomy* 65.3 (1996), pp. 313–344.
- [62] Werner, R.A. and Scheeres, D.J. "Mutual potential of homogeneous polyhedra". In: *Celestial Mechanics and Dynamical Astronomy* 91.3-4 (2005), pp. 337–349.